A coupled, two-phase fluid-sediment material model and mixture theory implemented using the material point method

by

Aaron S. Baumgarten

Submitted to the Department of Aeronautics and Astronautics
in partial fulfillment of the requirements for the degree of

Master of Science in Aerospace Engineering

at the

MASSACHUSETTS INSTITUTE OF TECHNOLOGY

June 2018

Signature redacted

Author .....
Department of Aeronautics and Astronautics
May 24, 2018

Signature redacted

Certified by ....
Ken Kamrin
Associate Professor of Mechanical Engineering
Thesis Supervisor

Signature redacted

Certified by ...
Raul Radovitzky
Professor of Aeronautics and Astronautics
Thesis Supervisor

Signature redacted

Accepted by .....
Hamsa Balakrishnan
Associate Professor of Aeronautics and Astronautics
Chair, Graduate Program Committee

A coupled, two-phase fluid-sediment material model and mixture theory implemented using the material point method

by

Aaron S. Baumgarten

Submitted to the Department of Aeronautics and Astronautics
on May 24, 2018, in partial fulfillment of the
requirements for the degree of
Master of Science in Aerospace Engineering

Abstract

A thermodynamically consistent constitutive model for fluid-saturated sediments, spanning dense to dilute regimes is developed from the integral form of the basic balance laws for two-phase mixtures. This model is formulated to capture the (i) viscous inertial rheology of wet grains under steady shear, (ii) the critical state behavior of granular materials under shear, (iii) the viscous thickening of fluid due to the presence of suspended grains, and (iv) the Darcy-like drag interaction for both dense and dilute mixtures. The full constitutive model is combined with the basic equations of motion for each mixture phase and implemented in the material point method (MPM) to accurately model the coupled dynamics of the combined system. Qualitative results show the breadth of problems, which this model can address. Quantitative results demonstrate the accuracy of this model as compared with analytical models and experimental observations.

Thesis Supervisor: Ken Kamrin
Title: Associate Professor of Mechanical Engineering

Thesis Supervisor: Raul Radovitzky
Title: Professor of Aeronautics and Astronautics

Acknowledgments

The completion of this work would not have been possible without the guidance and support of my research advisor Ken Kamrin and my academic advisor Raul Radovitzky. Raul has continually expected and encouraged me to be a better student and researcher, and Ken has been an invaluable tutor and resource for finding, addressing, and solving challenging problems. To both of these mentors, I am grateful.

I thank my parents and younger brother for their support, encouragement, and the open invitation for a meal at home if I needed it.

I am thankful for all of my peers in AeroAstro and MechE, especially the AeroAstro Blackbirds IM hockey team, the members of the Kamrin Group, and my friends in the ACDL, for making this entire experience a positive one. I am also indebted to an innumerable number of friends who have been there for me throughout my time at MIT, the MIT Heavyweight Rowing team, and the 'lab group of destiny'.

In particular, though, I want to thank Alex Feldstein and Connor McMahon, whose patience and friendship I could not do without.

Contents

List of Figures

List of Tables

Chapter 1

Introduction

Mixtures of fluids and sediments play an important role in many industrial and geotechnical engineering problems, from transporting large volumes of industrial wastes to building earthen levees and damns. To solve these problems, engineers have traditionally relied on the myriad of empirical models developed in the last century.

These empirical models are derived by coupling relevant experimental observations to an understanding of the underlying physics governing the behavior of these mixtures. The model reported in Einstein [1906] describes the viscous thickening of fluids due to dilute suspensions of grains. The Darcy-like drag law given in Carman [1937] describes the pressure drop in a fluid as it flows through a bed of densely packed grains. The work by Turian and Yuan [1977] characterizes the flow of slurries in pipelines. Other models (such as in Pailha and Pouliquen [2009]) describe more complex problems (such as the initiation of submerged granular avalanches); however, each of these models can only provide a description of a specific regime of mixture and flows.

To address an engineering problem which involves complex interactions of fluids and sediments spanning many flow regimes requires a more general modeling approach. A natural first step is to model the underlying physics directly by solving the coupled fluid grain interactions at the micro-scale (as in the coupled lattice Boltzman and discrete element method, LBM-DEM, proposed in Cook et al. [2004]). Many problems of interest, however, involve far too much material for a direct approach to be computationally viable. We therefore turn to a continuum modeling approach, where the small scale structures and physics are homogenized into bulk properties and behaviors. Recent work simulating fluid-sediment mixtures as continua (see Soga et al. [2015]) has shown promise, but the reported results are highly sensitive to the choice of sediment constitutive model (see Ceccato and Simonini [2016] and Fern and Soga [2016]); no existing dry granular plasticity models will correctly predict the behavior of saturated soils.

In this work, we begin with the integral form of the basic balance laws for two-phase mixture and carefully formulate a new set of constitutive rules governing the fluid and sediment phases of the continuum mixture. Using these rules, we construct a model which recovers the correct limiting empirical behaviors (i.e. dry and viscous granular inertial rheologies, viscous thickening due to suspended grains, Stokes and Carman-Kozeny drags, and

Reynolds dilation) and smoothly transitions between flow regimes covering the range from dense slurry-like flow to dilute suspensions. We discretize the weak form of the governing equations of motion using MPM and validate this implementation against several dynamic experiments involving submerged glass beads. We also consider the application of our model to the problems of slope collapses and intrusion.

Chapter 2

Theory and Formulation

Here we lay out the theoretical framework for the two-phase mixture model. In the formulation of this theory, we use the standard notation of continuum mechanics from Gurtin et al. [2010]. In particular, the trace of the tensor $\mathbf{A}$ is given by $\operatorname{tr}\mathbf{A}$ and the transpose by $\mathbf{A}^\top$. Every tensor admits the unique decomposition into a deviatoric part $\mathbf{A_0}$ and spherical part by $\mathbf{A} = \mathbf{A_0} + \frac{1}{3}\operatorname{tr}(\mathbf{A})\mathbf{1}$ with $\mathbf{1}$ the identity tensor.

2.1 Mixture Theory

To develop the model we start by considering a mixture of grains and fluid. We assume that the grains are rough (i.e. *true* contact can occur between grains), incompressible with density ρ_s, and essentially spherical with diameter d. We also assume that the grains are fully immersed in a barotropic viscofluid with local density ρ_f and viscosity η_0. A representative volume of material, Ω, can therefore be decomposed into a solid volume, Ω_s, and a fluid volume, Ω_f, such that $\Omega = \Omega_s \cup \Omega_f$.

Figure 2-1 shows how this volume is decomposed and the important step of homogenizing the solid volume and fluid volume into two, overlapping continua. In the analysis that follows, ψ_s will refer to some field ψ defined on the solid phase, and ψ_f will refer to some field ψ defined on the fluid phase. If no subscript is given, then that field is defined on the mixture as a whole.

After defining the *effective* or *homogenized* fields, we derive the equations of motion through conservation of mass and momentum. This analysis is essentially identical to that of Bandara and Soga [2015], but explicating it fully here allows us to better present our novel constitutive model and numerical framework.

2.1.1 Homogenization of Phases

The effective densities $\overline{\rho}_s$ and $\overline{\rho}_f$, and phase velocities $\mathbf{v_s}$ and $\mathbf{v_f}$ of the mixture are defined such that conservation of mass and momentum in the continuum correspond to conservation of mass and momentum in the real mixture. For this, we consider a representative volume of

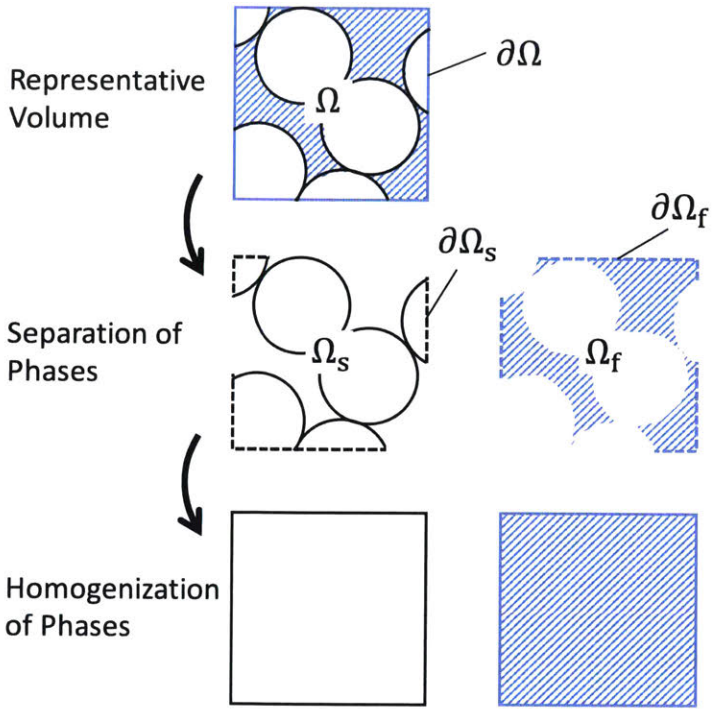

Figure 2-1: Pictorial description of the representative volume Ω and boundary $\partial\Omega$, the decomposition of the domain into fluid and solid volumes, and the homogenization of the two phases.

material, Ω, that contains a *large* number of individual grains. For the continuum approximation to be valid, *large* is defined such that grain-scale phenomena are smoothed out and bulk behavior is captured.

$$\begin{aligned}
\int_{\Omega} \overline{\rho}_s dv &= \int_{\Omega_s} \rho_s dv \\
\int_{\Omega} \overline{\rho}_f dv &= \int_{\Omega_f} \rho_f dv \\
\int_{\Omega} \overline{\rho}_s \mathbf{v_s} dv &= \int_{\Omega_s} \rho_s \mathbf{v} dv \\
\int_{\Omega} \overline{\rho}_f \mathbf{v_f} dv &= \int_{\Omega_f} \rho_f \mathbf{v} dv
\end{aligned} \tag{2.1}$$

We now introduce the concept of the local packing fraction and the local porosity. The packing fraction, ϕ, is defined as the ratio of volume of solid grains to volume of mixture. The porosity, n, is defined as the ratio of the volume of the fluid to the volume of mixture.

$$\phi = \frac{\int_{\Omega_s} dv}{\int_{\Omega} dv}, \qquad n = \frac{\int_{\Omega_s} dv}{\int_{\Omega} dv}$$

As a consequence of this definition, evaluation of Equation (2.1) over a *small* representative volume (where *small* is defined such that changes in the local fields are negligible) leads to three important results. First, the packing fraction and porosity can be calculated from one another (their sum must be one). Second, the effective solid density is equal to the density of the grains scaled by the packing fraction. And third, the effective fluid density is equal to the local fluid density scaled by the porosity.

$$\begin{aligned} \phi &= 1 - n \\ \overline{\rho}_s &= \phi \rho_s \\ \overline{\rho}_f &= n \rho_f \end{aligned} \tag{2.2}$$

We must also define the effective body force acting on each phase in the continuum, $\mathbf{b_{0s}}$ and $\mathbf{b_{0f}}$. As with effective density, we require that the integral of the effective body force over the whole volume be equal to the integral of the actual body force over the phase volume. In the presence of a constant gravity, $\mathbf{g}$, and in the absence of other body forces, we state:

$$\int_\Omega \mathbf{b_{0s}} dv = \int_{\Omega_s} \mathbf{b_0} dv = \int_{\Omega_s} \rho_s \mathbf{g} dv$$

$$\int_\Omega \mathbf{b_{0f}} dv = \int_{\Omega_f} \mathbf{b_0} dv = \int_{\Omega_f} \rho_f \mathbf{g} dv$$

Using the definitions in Equation (2.1), it can be shown that the effective body forces must have the following form,

$$\begin{aligned} \mathbf{b_{0s}} &= \overline{\rho}_s \mathbf{g} \\ \mathbf{b_{0f}} &= \overline{\rho}_f \mathbf{g} \end{aligned} \tag{2.3}$$

Lastly, we define the effective Cauchy stress, $\boldsymbol{\sigma}$, of the mixture according to the integral form of Cauchy's Theorem. This relation is given in Equation (2.4). Since we define the domain boundary $\partial\Omega$ such that $\partial\Omega = \partial\Omega_s \cup \partial\Omega_f$, we can also define the effective Cauchy stress on each phase, $\boldsymbol{\sigma}_{\langle\cdot\rangle}$. In these expressions, $\mathbf{t}$ is the surface traction vector which is a function of the surface normal vector $\mathbf{n}$.

$$\begin{aligned} \int_{\partial\Omega} \boldsymbol{\sigma} \mathbf{n} da &= \int_{\partial\Omega} \mathbf{t}(\mathbf{n}) da \\ \int_{\partial\Omega} \boldsymbol{\sigma_s} \mathbf{n} da &= \int_{\partial\Omega_s} \mathbf{t}(\mathbf{n}) da \\ \int_{\partial\Omega} \boldsymbol{\sigma_f} \mathbf{n} da &= \int_{\partial\Omega_f} \mathbf{t}(\mathbf{n}) da \end{aligned} \tag{2.4}$$

It follows from $\partial\Omega = \partial\Omega_s \cup \partial\Omega_f$, that,

$$\int_{\partial\Omega} \mathbf{t}(\mathbf{n}) da = \int_{\partial\Omega_s} \mathbf{t}(\mathbf{n}) da + \int_{\partial\Omega_f} \mathbf{t}(\mathbf{n}) da$$

and therefore,

$$\int_{\partial\Omega} \boldsymbol{\sigma}\mathbf{n}da = \int_{\partial\Omega} \boldsymbol{\sigma_s}\mathbf{n}da + \int_{\partial\Omega} \boldsymbol{\sigma_f}\mathbf{n}da$$

Since this must hold for any choice of volume Ω and boundary $\partial\Omega$, we require,

$$\boldsymbol{\sigma} = \boldsymbol{\sigma_s} + \boldsymbol{\sigma_f} \tag{2.5}$$

By defining the effective Cauchy stresses as in Equation (2.4), we show that the total effective Cauchy stress of the mixture can be decomposed into a stress contribution belonging to the solid phase and another belonging to the fluid phase. This will become important later when we define the constitutive models for the two phases.

2.1.2 Overlapping Continuum Bodies

In the previous section, we defined a continuum representation for a mixture of grains and fluid. We now turn our consideration to the continuum mixture model. As shown in Figure 2-2(a), we first define two overlapping continuum bodies. $\mathcal{B}^s$ defines the solid phase reference body and $\mathcal{B}^f$ defines the fluid phase reference body. At some time t, $\mathcal{B}_t^s$ defines the solid phase deformed body and $\mathcal{B}_t^f$ defines the fluid phase deformed body. These definitions allow us to use the usual continuum definitions of motion, as in Gurtin et al. [2010].

To determine the behavior of a volume of mixture Ω, as shown in figure 2-2(b), we let that volume define a part in each continuum body. The full mixture is defined by the sum of these parts. If the volume of mixture is composed of fluid only, the porosity n is unity. We also enforce that, in the absence of a solid phase, the local solid phase stress is zero, $\boldsymbol{\sigma_s} = \mathbf{0}$. In this limit, we expect the behavior of the mixture to be identical to that of a barotropic viscous fluid. If the volume of mixture is solid only, the porosity n is *not* zero (it would only be zero in the limit of vanishing pore space). In this limit, the behavior of the mixture should be identical to that of a dry granular material. To ensure this, we enforce that the local fluid phase stress is zero, $\boldsymbol{\sigma_f} = \mathbf{0}$, *and* that the *true* fluid density is zero, $\rho_f = 0$.

2.1.3 Mass Conservation

We now define the equations governing the evolution of the *true* fluid density (i.e. the density of the fluid that is between the grains), ρ_f, and the effective densities of both phases, $\overline{\rho}_s$ and $\overline{\rho}_f$. Recalling that the solid grains are assumed incompressible, ρ_s is constant. Since we will often have fields which *belong* to one phase or another (e.g. ρ_s *belongs* to the solid phase), it is convenient to define the material derivatives on each phase as follows,

$$\begin{aligned} \frac{D^s\psi}{Dt} &= \frac{\partial\psi}{\partial t} + \mathbf{v_s}\cdot\operatorname{grad}\psi \\ \frac{D^f\psi}{Dt} &= \frac{\partial\psi}{\partial t} + \mathbf{v_f}\cdot\operatorname{grad}\psi \end{aligned} \tag{2.6}$$

We consider a volume of continuum mixture Ω. Mass conservation in the solid phase is

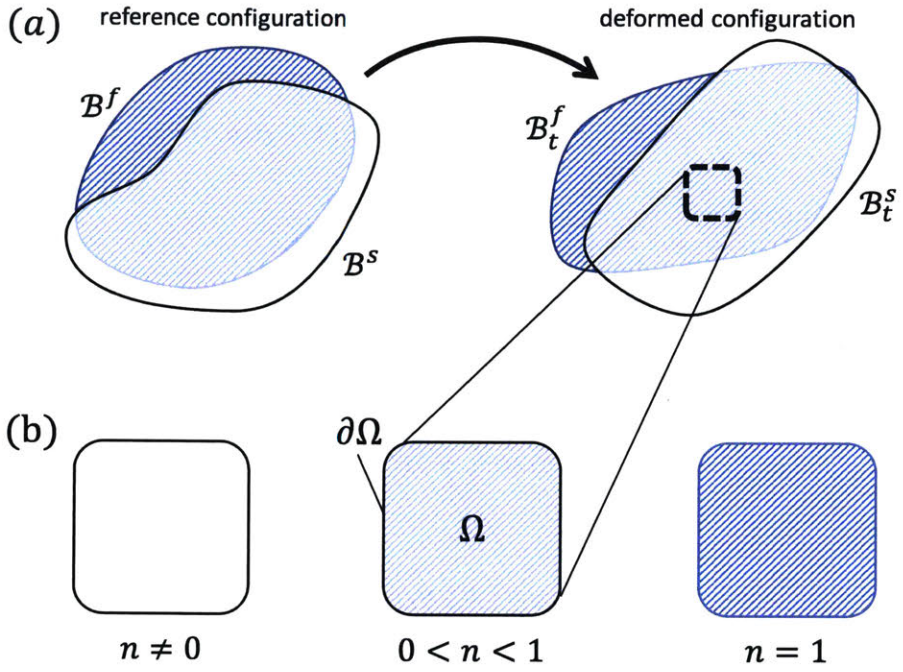

Figure 2-2: (a) Pictorial definition of the reference bodies, $\mathcal{B}^s$ and $\mathcal{B}^f$, and deformed bodies, $\mathcal{B}_t^s$ and $\mathcal{B}_t^f$. (b) Parts in the deformed body are *always* fully saturated with porosity $n > 0$. In the limit of a fluid-only volume, the porosity $n = 1$. In the limit of a solid-only volume, we *do not* let the porosity n go to zero, instead we let the fluid viscosity and bulk modulus go to zero.

enforced by setting the material derivative of solid mass in this volume to zero.

$$\frac{D^s}{Dt}\int_\Omega \overline{\rho}_s dv = 0$$

Using Reynolds' transport relation we can move the material derivative inside of the integral.

$$\int_\Omega \frac{D^s\overline{\rho}_s}{Dt} + \overline{\rho}_s \operatorname{div}(\mathbf{v_s}) dv = 0$$

This must be true of any choice of volume Ω, therefore the strong form statement must also be true. We therefore arrive at Equation (2.7) which governs the evolution of the effective solid density.

$$\frac{D^s\overline{\rho}_s}{Dt} + \overline{\rho}_s \operatorname{div}\mathbf{v_s} = 0 \tag{2.7}$$

We then expand the first term of this evolution law according to Equation (2.6).

$$\frac{\partial\overline{\rho}_s}{\partial t} + \mathbf{v_s}\cdot\operatorname{grad}\overline{\rho}_s + \overline{\rho}_s \operatorname{div}\mathbf{v_s} = 0$$

Expanding with the identity, $\overline{\rho}_s = \phi\rho_s = (1-n)\rho_s$,

$$\frac{\partial(1-n)\rho_s}{\partial t} + \mathbf{v_s} \cdot \operatorname{grad}((1-n)\rho_s) + (1-n)\rho_s \operatorname{div} \mathbf{v_s} = 0$$

and applying the chain rule,

$$(1-n)\frac{\partial \rho_s}{\partial t} - \rho_s \frac{\partial n}{\partial t} + (1-n)\mathbf{v_s} \operatorname{grad} \rho_s - \rho_s \mathbf{v_s} \cdot \operatorname{grad} n + (1-n)\rho_s \operatorname{div} \mathbf{v_s} = 0$$

Enforcing uniform incompressible grains (ρ_s constant) and dividing out ρ_s, we find,

$$-\frac{\partial n}{\partial t} - \mathbf{v_s} \cdot \operatorname{grad} n + (1-n) \operatorname{div} \mathbf{v_s} = 0$$

and therefore,

$$\frac{\partial n}{\partial t} = (1-n) \operatorname{div} \mathbf{v_s} - \mathbf{v_s} \cdot \operatorname{grad} n \tag{2.8}$$

The significance of Equation (2.8) is that we can express the rate of change of the local porosity with knowledge of the current porosity and the solid phase velocity alone. Intuitively this makes sense, the porosity is a measure of the space between grains. We only need a description of the motion of the grains to describe how the porosity is changing.

Turning now to the fluid part defined by the volume Ω, we enforce mass conservation in the fluid phase by setting the material derivative of fluid mass to zero.

$$\frac{D^f}{Dt} \int_\Omega \overline{\rho}_f dv = 0$$

As before, we use Reynolds' transport relation to move the material derivative inside the integral.

$$\int_\Omega \frac{D^f \overline{\rho}_f}{Dt} + \overline{\rho}_f \operatorname{div} \mathbf{v_f} dv = 0$$

This must hold for any choice of volume Ω, therefore we find Equation (2.9), which governs the evolution of the effective fluid phase density.

$$\frac{D^f \overline{\rho}_f}{Dt} + \overline{\rho}_f \operatorname{div} \mathbf{v_f} = 0 \tag{2.9}$$

We expand the first term according to Equation (2.6),

$$\frac{\partial \overline{\rho}_f}{\partial t} + \mathbf{v_f} \cdot \operatorname{grad} \overline{\rho}_f + \overline{\rho}_f \operatorname{div} \mathbf{v_f} = 0$$

and replace $\overline{\rho}_f$ above with it's definition in Equation (2.2),

$$\frac{\partial n\rho_f}{\partial t} + \mathbf{v_f} \cdot \text{grad}(n\rho_f) + n\rho_f \,\text{div}\, \mathbf{v_f} = 0$$

Using the chain rule, we find,

$$n\frac{\partial \rho_f}{\partial t} + \rho_f \frac{\partial n}{\partial t} + n\mathbf{v_f} \cdot \text{grad}(\rho_f) + \rho_f \mathbf{v_f} \cdot grad(n) + n\rho_f \,\text{div}\, \mathbf{v_f} = 0$$

We then group terms multiplied by n and ρ_f

$$n\left(\frac{\partial \rho_f}{\partial t} + \mathbf{v_f} \cdot \text{grad}\, \rho_f\right) + \rho_f \left(\frac{\partial n}{\partial t} + \mathbf{v_f} \cdot grad(n) + n \,\text{div}\, \mathbf{v_f}\right) = 0$$

Recognizing the material derivative in the first term and replacing $\frac{\partial n}{\partial t}$ with its definition in Equation (2.8), the above expression can be rewritten,

$$n\frac{D^f \rho_f}{Dt} + \rho_f \big((1-n)\,\text{div}\, \mathbf{v_s} - \mathbf{v_s} \cdot \text{grad}(n) + \mathbf{v_f} \cdot \text{grad}(n) + n\,\text{div}\, \mathbf{v_f}\big) = 0$$

With some further simplification, we find Equation (2.10), which governs the evolution of the *true* fluid density.

$$\frac{n}{\rho_f}\frac{D^f \rho_f}{Dt} = -\,\text{div}\,\big((1-n)\mathbf{v_s} + n\mathbf{v_f}\big) \tag{2.10}$$

2.1.4 Momentum Balance

Conservation of linear momentum can be expressed for a volume Ω in the deformed configuration on the mixture as a whole or on each phase independently. For the entire mixture, this conservation law, in integral form is given as,

$$\int_\Omega \overline{\rho}_s \frac{D^s \mathbf{v}_s}{Dt} + \overline{\rho}_f \frac{D^f \mathbf{v}_f}{Dt} dv = \int_\Omega \mathbf{b_{0s}} + \mathbf{b_{0f}} dv + \int_{\partial\Omega} \mathbf{t}(\mathbf{n}) da \tag{2.11}$$

Using Equation (2.3) and (2.4), the above expression can be rewritten as,

$$\int_\Omega \overline{\rho}_s \frac{D^s \mathbf{v}_s}{Dt} + \overline{\rho}_f \frac{D^f \mathbf{v}_f}{Dt} dv = \int_\Omega (\overline{\rho}_s + \overline{\rho}_f)\mathbf{g} dv + \int_{\partial\Omega} \boldsymbol{\sigma}\mathbf{n} da$$

and applying the divergence theorem,

$$\int_\Omega \overline{\rho}_s \frac{D^s \mathbf{v}_s}{Dt} + \overline{\rho}_f \frac{D^f \mathbf{v}_f}{Dt} dv = \int_\Omega (\overline{\rho}_s + \overline{\rho}_f)\mathbf{g} + \text{div}\, \boldsymbol{\sigma} dv \tag{2.12}$$

Equation (2.12) must hold for any choice of volume Ω, therefore Equation (2.13) must

be true everywhere,

$$\overline{\rho}_s \frac{D^s \mathbf{v}_s}{Dt} + \overline{\rho}_f \frac{D^f \mathbf{v}_f}{Dt} = (\overline{\rho}_s + \overline{\rho}_f)\mathbf{g} + \operatorname{div} \boldsymbol{\sigma} \tag{2.13}$$

This is the general strong form of momentum balance in the mixture. Intuitively, it matches our expectation that the rate of change of momentum in the mixture will depend on the total body force and total stress divergence. It will also serve as a check for the phase-wise momentum balance equations we derive next.

Recalling the expressions in Equation (2.4), the integral form of mass conservation in each phase can be written as,

$$\begin{aligned} \int_\Omega \overline{\rho}_s \frac{D^s \mathbf{v}_s}{Dt} dv &= \int_\Omega \mathbf{b_{0s}} - \mathbf{f_b} - \mathbf{f_d} dv + \int_{\partial\Omega} \boldsymbol{\sigma_s} \mathbf{n} da \\ \int_\Omega \overline{\rho}_f \frac{D^f \mathbf{v}_f}{Dt} dv &= \int_\Omega \mathbf{b_{0f}} + \mathbf{f_b} + \mathbf{f_d} dv + \int_{\partial\Omega} \boldsymbol{\sigma_f} \mathbf{n} da \end{aligned} \tag{2.14}$$

We've introduced two new body forces, $\mathbf{f_b}$ and $\mathbf{f_d}$. $\mathbf{f_b}$ has the form of the *buoyant* force described in Drumheller [2000]. As we will see in Equation (2.20) this term is necessary to recover the correct physical behavior of immiscible mixtures. $\mathbf{f_d}$ is the *drag* or Darcy's law force. We simplify this expression using the divergence theorem,

$$\begin{aligned} \int_\Omega \overline{\rho}_s \frac{D^s \mathbf{v}_s}{Dt} dv &= \int_\Omega \mathbf{b_{0s}} - \mathbf{f_b} - \mathbf{f_d} + \operatorname{div} \boldsymbol{\sigma_s} dv \\ \int_\Omega \overline{\rho}_f \frac{D^f \mathbf{v}_f}{Dt} dv &= \int_\Omega \mathbf{b_{0f}} + \mathbf{f_b} + \mathbf{f_d} + \operatorname{div} \boldsymbol{\sigma_f} dv \end{aligned} \tag{2.15}$$

As before, Equation (2.15) must be true for any choice of volume Ω, therefore the strong form of momentum balance holds everywhere.

$$\begin{aligned} \overline{\rho}_s \frac{D^s \mathbf{v}_s}{Dt} &= \mathbf{b_{0s}} - \mathbf{f_b} - \mathbf{f_d} + \operatorname{div} \boldsymbol{\sigma_s} \\ \overline{\rho}_f \frac{D^f \mathbf{v}_f}{Dt} &= \mathbf{b_{0f}} + \mathbf{f_b} + \mathbf{f_d} + \operatorname{div} \boldsymbol{\sigma_f} \end{aligned} \tag{2.16}$$

Because the buoyant and drag forces act *between* phases, we see that taking the sum of the expressions in Equation (2.16) yields Equation (2.13), showing consistency of our method. We leave the specific form of the buoyant and drag force and the phase stresses for later sections.

2.1.5 Specific Form of Phase Stresses

Equation (2.16) fully describes the motion of mixture; however, it is not very useful until we develop expressions for the inter-phase forces and stresses. Since our definitions in Section 2.1.1 rely on selecting a *large* domain, we expect that the stresses defined in Equation (2.4) will contain contributions from both phases of the real mixture.

As we will see in Section 2.1.7, in order to recover the form of momentum balance given in Jackson [2000], we let the solid phase stress $\boldsymbol{\sigma_s}$ take the classic form,

$$\boldsymbol{\sigma_s} = \tilde{\boldsymbol{\sigma}} - (1-n)p_f\mathbf{1} \tag{2.17}$$

$\tilde{\boldsymbol{\sigma}}$ is the portion of the solid phase stress resulting from *true* granular contacts and from microscopic viscous interactions between grains due to immersion in a fluid medium (e.g. lubrication forces). We will see later that this is also the Terzaghi effective stress that governs plastic flow in the solid phase. $\tilde{\boldsymbol{\sigma}}$ is not necessarily deviatoric. p_f is the *true* fluid phase pore pressure. Since the fluid is barotropic, this is determined by the *true* fluid density ρ_f.

The expression for the fluid phase stress $\boldsymbol{\sigma_f}$ is taken to be,

$$\boldsymbol{\sigma_f} = \boldsymbol{\tau_f} - np_f\mathbf{1} \tag{2.18}$$

The fluid phase stress is decomposed into a deviatoric part, $\boldsymbol{\tau_f}$, and a spherical part, $np_f\mathbf{1}$. We expect the viscous shear stress in the fluid phase, $\boldsymbol{\tau_f}$, to be proportional to the shear rate of the fluid and a function of the porosity of the mixture.

2.1.6 Specific Form of the Buoyant Body Force

To gain an intuition for the form of the buoyant term, we substitute the expression for the solid phase stress in Equation (2.17) into the expression for the solid phase momentum balance in Equation (2.16),

$$\overline{\rho}_s\frac{D^s\mathbf{v_s}}{Dt} = \overline{\rho}_s\mathbf{g} - \mathbf{f_b} - \mathbf{f_d} + \operatorname{div}(\tilde{\boldsymbol{\sigma}} - (1-n)p_f\mathbf{1})$$

We then separate the divergence of the total solid phase stress into the divergence of the Terzaghi effective stress and gradient of scaled pressure,

$$\overline{\rho}_s\frac{D^s\mathbf{v_s}}{Dt} = \overline{\rho}_s\mathbf{g} - \mathbf{f_b} - \mathbf{f_d} + \operatorname{div}(\tilde{\boldsymbol{\sigma}}) - \operatorname{grad}\left((1-n)p_f\right)$$

Then, applying the chain rule to the gradient term, we find

$$\overline{\rho}_s\frac{D^s\mathbf{v_s}}{Dt} = \overline{\rho}_s\mathbf{g} - \mathbf{f_b} - \mathbf{f_d} + \operatorname{div}(\tilde{\boldsymbol{\sigma}}) + p_f\operatorname{grad}(n) - (1-n)\operatorname{grad}(p_f) \tag{2.19}$$

Equation (2.19) has the unusual property that, as given, the acceleration of the solid phase appears to depend directly on the *magnitude* of the fluid pressure p_f. To emphasize the oddity of this result, consider a bed of grains settled at the bottom of a fluid chamber. If the acceleration does have this property, then it would be possible to unsettle the grains simply by adding a uniform pressure to the entire chamber. Since we do not observe this in practice, we let the buoyant force take the form given in Drumheller [2000],

$$\mathbf{f_b} = p_f\operatorname{grad}(n) \tag{2.20}$$

2.1.7 Equations of Motion

With the expressions for the stresses and the buoyant body force given in Equations (2.17), (2.18), and (2.20), we recover the equations of motion from Jackson [2000]. Substituting Equation (2.20) into Equation (2.19), we find the final expression of the solid phase momentum balance,

$$\overline{\rho}_s \frac{D^s \mathbf{v_s}}{Dt} = \overline{\rho}_s \mathbf{g} - \mathbf{f_d} + \operatorname{div}(\tilde{\boldsymbol{\sigma}}) - (1-n)\operatorname{grad}(p_f) \tag{2.21}$$

For the fluid phase, we substitute Equation (2.18) into Equation (2.16),

$$\overline{\rho}_f \frac{D^f \mathbf{v_f}}{Dt} = \overline{\rho}_f \mathbf{g} + \mathbf{f_b} + \mathbf{f_d} + \operatorname{div}(\boldsymbol{\tau_f} - np_f \mathbf{1})$$

and,

$$\overline{\rho}_f \frac{D^f \mathbf{v_f}}{Dt} = \overline{\rho}_f \mathbf{g} + \mathbf{f_b} + \mathbf{f_d} + \operatorname{div} \boldsymbol{\tau_f} - \operatorname{grad}(np_f)$$

Using the chain rule,

$$\overline{\rho}_f \frac{D^f \mathbf{v_f}}{Dt} = \overline{\rho}_f \mathbf{g} + \mathbf{f_b} + \mathbf{f_d} + \operatorname{div}(\boldsymbol{\tau_f}) - n\operatorname{grad}(p_f) - p_f \operatorname{grad}(n)$$

and substituting in the expression for the buoyant body force,

$$\overline{\rho}_f \frac{D^f \mathbf{v_f}}{Dt} = \overline{\rho}_f \mathbf{g} + \mathbf{f_d} + \operatorname{div}(\boldsymbol{\tau_f}) - n\operatorname{grad}(p_f) \tag{2.22}$$

Together, Equations (2.21) and (2.22) are the complete equations of motion of the mixture. If we let,

$$\langle \mathbf{f} \rangle = \mathbf{f_d} - (1-n)\operatorname{grad}(p_f)$$

then we recover Equations (2.27') and (2.28') from Jackson [2000],

$$\begin{aligned} \phi\rho_s \frac{D^s \mathbf{v_s}}{Dt} &= \operatorname{div}(\tilde{\boldsymbol{\sigma}}) - \langle \mathbf{f} \rangle + \phi\rho_s \mathbf{g} \\ n\rho_f \frac{D^f \mathbf{v_f}}{Dt} &= \operatorname{div}(\boldsymbol{\tau_f} - p_f \mathbf{1}) + \langle \mathbf{f} \rangle + n\rho_f \mathbf{g} \end{aligned} \tag{2.23}$$

In addition to the equations of motion, we also need to define the equations of state to fully characterize the mixture. In the following sections, we will formulate the laws governing the inter-phase drag force $\mathbf{f_d}$, the Terzaghi effective granular stress $\tilde{\boldsymbol{\sigma}}$, the fluid phase effective shear stress $\boldsymbol{\tau_f}$, and the fluid pressure p_f.

2.2 Methods for Formulating Drag Law

The flow of viscous fluid around and between grains of sediment will result in an inter-phase drag that we represent with the drag force $\mathbf{f_d}$. This drag force can be understood as a body force acting on one phase by the other and has units $[N/m^3]$. In this work we assume that this force depends only on the relative velocities of the two phases $(\mathbf{v_s} - \mathbf{v_f})$, the porosity of the mixture n, the grain diameter d, and the fluid viscosity η_0. We neglect dependence on material orientation or rotation (e.g. a fabric tensor).

$$\mathbf{f_d} = \hat{\mathbf{f}}_\mathbf{d}(\mathbf{v_s} - \mathbf{v_f}, n, d, \eta_0) \tag{2.24}$$

There are three general methods which may be used to determine the form of Equation (2.24): analytical, empirical, and simulation.

2.2.1 Analytical Method: Stokes's Law

In a dilute mixture ($\phi \to 0$), the individual solid grains are dispersed in the fluid and seldom interact. In this limit, it is reasonable to assume that the fluid flow around a single grain will not be affected by the flow around neighboring grains. Therefore, (as shown in Figure 2-3) we calculate the force on a single grain in an *large* fluid domain and homogenize this force through Equation (2.3). *Large* here is taken to mean that the inflow and outflow of the domain are approximately uniform.

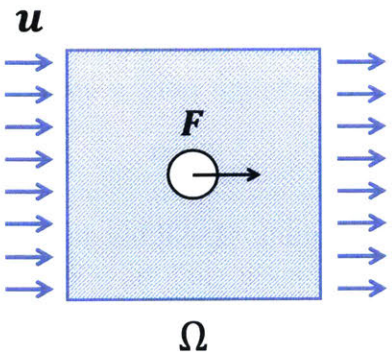

Figure 2-3: In a dilute mixture ($\phi \to 0$), the viscous drag of the fluid phase on the solid phase can be calculated from the flow field around individual grains through Stokes' law. We consider a spherical grain with diameter d in a *large* fluid domain Ω. The free stream fluid velocity is given as $\mathbf{u}$, and the resulting drag force is $\mathbf{F}$.

We begin by considering the Stokes-Einstein drag equation for a single sphere with diameter d in a Stokes' flow with free-stream velocity $\mathbf{u}$ and viscosity η_0,

$$\mathbf{F} = 3\pi\eta_0 d\mathbf{u} \tag{2.25}$$

Equation (2.25) is valid if the flow velocity is *small*. *Small* is taken to mean in the limit of

$\mathrm{Re} \to 0$, where

$$\mathrm{Re} = \frac{\rho_f \mathbf{u} d}{\eta_0} \tag{2.26}$$

To derive an expression for the inter-phase drag body force, we return to the intuition driving Equation (2.3). That is, we want to find $\mathbf{f_d}$ such that,

$$\int_\Omega -\mathbf{f_d} dv = \mathbf{F}$$

For a *small* domain, we let $\mathbf{f_d}$ be uniform and,

$$-\mathbf{f_d} \cdot \int_\Omega dv = \mathbf{F}$$

Replacing $\mathbf{F}$ with the Stokes-Einstein equation, we find,

$$-\mathbf{f_d} \cdot \int_\Omega dv = 3\pi\eta_0 d\mathbf{u} \tag{2.27}$$

There are two identities which we will use to transform this integral equation. First, we let that the volume of the solid phase be the volume of a sphere with diameter d,

$$\int_{\Omega_s} dv = \frac{\pi d^3}{6} \tag{2.28}$$

Second we have the definition of an average pore velocity, $\mathbf{u_e}$, which is related to the free stream velocity by,

$$\mathbf{u_e} = \frac{\mathbf{u}}{n} \tag{2.29}$$

Equation (2.29) was first shown by Dupuit [1863] for dense packings of grains, but it equally applicable in the dilute limit. Recognizing that $\mathbf{u_e}$ is expressible as the difference between the fluid phase velocity and the solid phase velocity, we let

$$\mathbf{u} = n\mathbf{u_e} = n(\mathbf{v_f} - \mathbf{v_s}) \tag{2.30}$$

Replacing Equations (2.28) and (2.30) in Equation (2.27),

$$\mathbf{f_d} \cdot \int_\Omega dv = 3n\pi\eta_0 d \cdot (\mathbf{v_s} - \mathbf{v_f}) \cdot \frac{\int_{\Omega_s} dv}{\frac{\pi d^3}{6}}$$

which is equivalent to,

$$\mathbf{f_d} = \frac{18n\eta_0}{d^2} \cdot \frac{\int_{\Omega_s} dv}{\int_\Omega dv} \cdot (\mathbf{v_s} - \mathbf{v_f})$$

and using the definitions in Equation (2.2), we arrive at an expression for the inter-phase

drag function derived from Stokes's Law.

$$\mathbf{f_d} = \frac{18n(1-n)\eta_0}{d^2} \cdot (\mathbf{v_s} - \mathbf{v_f}) \tag{2.31}$$

Although this method of formulating the drag term is analytically sound, its limitations are immediately apparent. Stokes's Law for drag on a sphere is valid only in the limit of $\mathrm{Re} \to 0$. Although other analytical expressions have been found for non-zero Reynolds number, a thorough analysis in Clift et al. [2005] suggests that analytical expressions for drag on a single sphere "have little value" for $\mathrm{Re} > 1$. Further, as the packing fraction increases ($\phi > 0$), we can no longer assume that the flow around one grain is independent of the proximity of other grains, and an analytical solution for such a flow is clearly intractable.

2.2.2 Empirical Method: Darcy's Law

We now consider the other end of the packing spectrum. For dense packings of grains ($\phi \to 0.65$), there is no analytical solution for the drag on the entire granular structure. In this limit, the grains of sediment pack tightly together forming what is essentially a porous solid. Therefore, (as shown in Figure 2-4) we can determine an expression for $\mathbf{f_d}$ empirically with Darcy's law. The steady flow of fluid through the pores of the solid phase will result in a measurable pressure drop across the solid phase. This pressure drop can be related to the inter-phase drag through Equation (2.22).

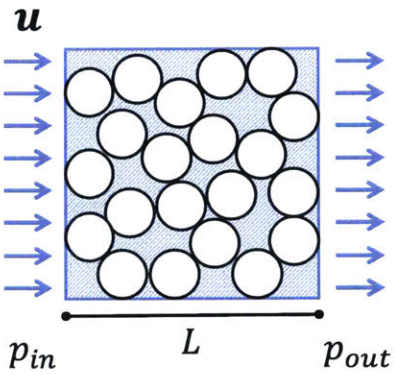

Figure 2-4: In a dense mixture ($\phi \to 0.65$), the viscous drag of the fluid phase on the solid phase can be determined empirically by relating the pressure drop, $(p_{out} - p_{in})$, measure over some distance, L, to the measured steady inlet flow velocity, $\mathbf{u}$.

The general method of determining an equation empirically, begins with the plotting of experimental results against dimensionless groups (in this analysis attributed to Blake [1922]). We therefore begin with the empirical relation given in Equation (10) of Carman [1937],

$$u = \frac{d^2}{k\eta_0} \cdot \frac{n^3}{36(1-n)^2} \cdot \frac{(p_{in} - p_{out})}{L} \tag{2.32}$$

where u is the measured steady fluid velocity at the inlet (and outlet), k is the permeability of the granular packing, p_{in} and p_{out} are the measured fluid pressures at the inlet and outlet of the packing, and L is the length of the granular packing (see Figure 2-4). The average pore fluid velocity u_e is related to the inlet flow velocity u through Equation (2.29),

$$u_e = \frac{u}{n}$$

Recognizing that u_e is expressible as the difference between the fluid phase velocity and the solid phase velocity, we let,

$$u_e \sim \mathbf{v_f} - \mathbf{v_s}$$

and assuming that the pressure drop per unit length is approximately uniform, we let,

$$\frac{(p_{out} - p_{in})}{L} \sim \text{grad}(p_f)$$

then Equation (2.32) can be rewritten as,

$$\mathbf{v_f} - \mathbf{v_s} = -\frac{d^2}{k\eta_0} \cdot \frac{n^2}{36(1-n)^2} \cdot \text{grad}(p_f)$$

or,

$$\text{grad}(p_f) = \frac{36k(1-n)^2\eta_0}{n^2 d^2}(\mathbf{v_s} - \mathbf{v_f}) \tag{2.33}$$

By plugging Equation (2.33) into Equation (2.22), we find

$$\overline{\rho}_f \frac{D^f \mathbf{v_f}}{Dt} = \overline{\rho}_f \mathbf{g} + \mathbf{f_d} + \text{div}(\boldsymbol{\tau_f}) - \frac{36k(1-n)^2\eta_0}{nd^2}(\mathbf{v_s} - \mathbf{v_f})$$

In the steady-state flow considered, and assuming gravitational effects and wall drags are negligible, this becomes

$$\mathbf{0} = \mathbf{f_d} - \frac{36k(1-n)^2\eta_0}{nd^2}(\mathbf{v_s} - \mathbf{v_f})$$

or,

$$\mathbf{f_d} = \frac{36k(1-n)^2\eta_0}{nd^2}(\mathbf{v_s} - \mathbf{v_f}) \tag{2.34}$$

Carman gives an average measure for the permeability k of dense packings of spheres ($0.60 \leq \phi \leq 0.647$) equal to about 5. Plugging this value into Equation (2.34), we recover the common expression for fluid drag in soils and sediments, the Carman-Kozeny drag equation (as used in Bandara and Soga [2015]),

$$\mathbf{f_d} = \frac{180(1-n)^2\eta_0}{nd^2}(\mathbf{v_s} - \mathbf{v_f}) \tag{2.35}$$

Equation (2.35) has the useful property that it accurately describes the drag rheology

of dense mixtures ($\phi > 0.6$). By observing how measured quantities depend on the non-dimensional groups describing the flow, a simple formula has been found. However, in the large range of regimes of interest ($0 < \phi < 0.65$), this expression is still insufficient. Direct comparison of Equations (2.31) and (2.35) shows that the Carman-Kozeny equation *does not* recover the analytical model from the Stokes-Einstein equation. In fact, at low packing fractions ($\phi \to 0$), the Carman-Kozeny equation *under*-predicts the drag associated with a single grain. Although the methodology of presented here is sound, a larger range of packing fractions and flow velocities must be considered in order to form a complete expression for the inter-phase drag.

2.2.3 Simulation Method: van der Hoef's Equation

Determining an expression for the inter-phase drag for the full range of potential packing fractions ($0 \leq \phi \leq 0.65$) has historically been an intractable challenge. Analytical methods *cannot* be used for high Reynolds number flows ($\mathrm{Re} > 1$) and flows with non-negligible packing fractions ($\phi > 0$). Experimentally, any *loose* packing ($\phi < 0.58$) without sustained granular contacts will quickly compact, making the collection of accurate measurements near impossible. In the last 30 years, advances in computational fluid dynamics have made it possible to directly simulate the flows around large clusters of particles immersed in fluid. In particular, we are interested in simulation results that have used the lattice-Boltzman method, a discrete formulation of Navier-Stokes equations which is capable of modeling fluid flows involving complex boundary geometries. van der Hoef et al. [2005] and Beetstra et al. [2007] use the lattice-Boltzman method to simulate the flow around mono- and bi-disperse packings of spheres in the range of $0.10 < \phi < 0.6$ and up to $\mathrm{Re} \approx 1000$. As shown in Figure 2-5, the flow simulation allows the calculation of an *average* force vector, $\mathbf{F}$. Once normalized, an empirical-like relation can be developed.

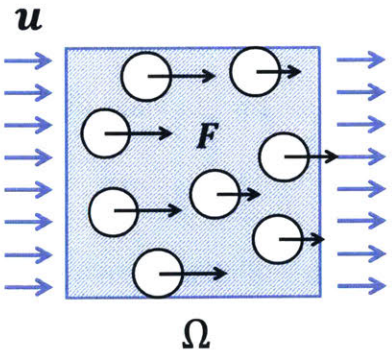

Figure 2-5: For an arbitrarily dense mixture ($0 < \phi < 0.65$), the fluid flow around the solid grains can be simulated using the lattice-Boltzmann method. The resulting average force vector, $\mathbf{F}$, can be normalized and empirically related to the free-stream flow velocity, $\mathbf{u}$.

The *average* force $\mathbf{F}$ is defined in terms of the total force (i.e. sum of skin and pressure

drags) of each grain, $\mathbf{F}_i$, in the simulated domain, Ω,

$$\mathbf{F} = \sum_{i \in \Omega} \mathbf{F}_i / N$$

where N is the total number of grains in the domain. To recover the viscous drag component, van der Hoef et al. [2005] gives the following definition,

$$\mathbf{F_d} = (1 - \phi)\mathbf{F}$$

$\mathbf{F_d}$ is then normalized by the Stokes-Einstein drag from Equation (2.25),

$$F = \frac{\mathbf{F_d}}{3\pi\eta_0 d\mathbf{u}} = \frac{(1-\phi)\mathbf{F}}{3\pi\eta_0 d\mathbf{u}} \tag{2.36}$$

where F is the normalized drag force measure and $\mathbf{u}$ is the inlet flow velocity of the simulation. Once F is determined for a wide range of simulations, an empirical relation can be developed by plotting the results against non-dimensional groups and finding a good fit line.

$$F = \hat{F}(\phi, \mathrm{Re})$$

van der Hoef et al. [2005] give the following form of F at low Reynolds numbers ($\mathrm{Re} \to 0$),

$$\hat{F}(\phi, 0) = \frac{10\phi}{(1-\phi)^2} + (1-\phi)^2(1 + 1.5\sqrt{\phi}) \tag{2.37}$$

Beetstra et al. [2007] expand on the previous work by considering mono-disperse flows up to $\mathrm{Re} = 1000$ and bi-disperse flows up to $\mathrm{Re} = 120$. The corrected form of F, is then,

$$\hat{F}(\phi, \mathrm{Re}) = \hat{F}(\phi, 0) + \frac{0.413\,\mathrm{Re}}{24(1-\phi)^2}\left(\frac{(1-\phi)^{-1} + 3\phi(1-\phi) + 8.4\,\mathrm{Re}^{-0.343}}{1 + 10^{3\phi}\,\mathrm{Re}^{-(1+4\phi)/2}}\right) \tag{2.38}$$

Now, as in Section 2.2.1, we want to find $\mathbf{f_d}$ such that,

$$\int_\Omega -\mathbf{f_d} dv = \mathbf{F_d}$$

For a sufficiently *large* domain Ω with sufficiently uniform $\mathbf{f_d}$,

$$-\mathbf{f_d} \int_\Omega dv = \mathbf{F_d}$$

Substituting in Equation (2.36), we find an expression that looks remarkably similar to the expression in Equation (2.27),

$$-\mathbf{f_d} \cdot \int_\Omega dv = 3\pi\eta_0 d\mathbf{u} \cdot \hat{F}(\phi, \mathrm{Re})$$

Recalling the definitions in Equations (2.28), (2.29), and (2.30), we arrive at the final expression for the inter-phase drag $\mathbf{f_d}$

$$\mathbf{f_d} = \frac{18\phi(1-\phi)\eta_0}{d^2} \cdot \hat{F}(\phi, \mathrm{Re}) \cdot (\mathbf{v_s} - \mathbf{v_f}) \tag{2.39}$$

where $\hat{F}(\phi, \mathrm{Re})$ is given as in Equation (2.37) or (2.38). Since this expression derives from direct simulation of flows through a wide range of granular packings, we expect it to more accurately represent the inter-phase drag of the mixture than either Equation (2.31) or (2.35).

2.2.4 Comparison of Methods

As shown in Figure 2-6, Equations (2.37) and (2.38) have properties which will be useful in the simulation of our continuum. First, both expressions return finite values for packing fractions in the range $0 < \phi < 1$ and Reynolds numbers in the range $\mathrm{Re} \geq 0$. Although physically we do not expect packing fractions above $\phi \approx 0.65$, it is possible that the continuum representation could exceed this limit. In the dilute ($\phi \to 0$), low Reynolds ($\mathrm{Re} \to 0$) limit, Equation (2.38) reduces to Equation (2.38) with the final result,

$$\hat{F}(0, 0) = 1$$

Plugging this into Equation (2.39), we recover the Stokes-Einstein inter-phase drag from Section 2.2.1,

$$\mathbf{f_d} = \frac{18\phi(1-\phi)\eta_0}{d^2} \cdot (\mathbf{v_s} - \mathbf{v_f}) = \frac{18n(1-n)\eta_0}{d^2} \cdot (\mathbf{v_s} - \mathbf{v_f})$$

In the dense ($\phi \to 1$), low Reynolds ($\mathrm{Re} \to 0$) limit, Equation (2.38) reduces to Equation (2.38) with the final result,

$$\hat{F}(1, 0) \approx \frac{10\phi}{(1-\phi)^2}$$

Plugging this into Equation (2.39), we recover the Carman-Kozeny inter-phase drag from Section 2.2.2,

$$\mathbf{f_d} = \frac{180\phi^2\eta_0}{(1-\phi)d^2} \cdot (\mathbf{v_s} - \mathbf{v_f}) = \frac{180(1-n)^2\eta_0}{nd^2} \cdot (\mathbf{v_s} - \mathbf{v_f})$$

2.3 Material Constitutive Models

In this section, we lay out the thermodynamic rules governing the behavior of the mixture. When considering a single phase of material, it is often useful to assume that *internal energy* (ε), *entropy* (η), and *absolute temperature* (ϑ) are basic properties of a material. That is, they do not need to be defined in terms of other more basic properties. For this analysis, we assume that analogous continuum fields exist describing the energy, entropy, and temperature

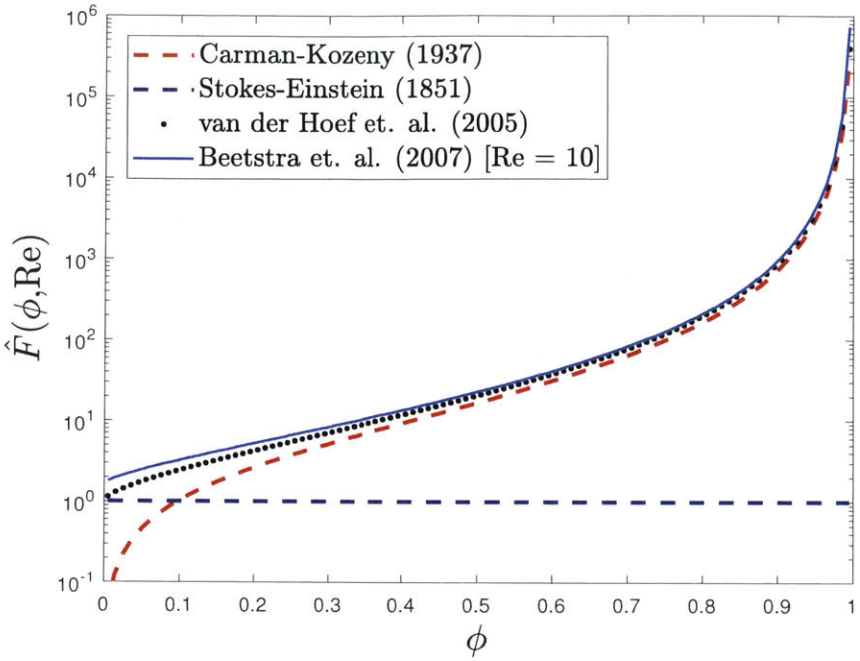

Figure 2-6: Comparison of the normalized drag force expressions, $\hat{F}(\phi, \mathrm{Re})$. In the dilute limit ($\phi \to 0$), the Carman-Kozeny equation clearly under-predicts the analytical drag force given by the Stokes-Einstein drag equation. In the dense limit ($\phi \to 0.65$), the Stokes-Einstein drag equation under-predicts the experimentally derived Carman-Kozeny equation. The expressions from van der Hoef et al. [2005] and Beetstra et al. [2007] capture both limits correctly.

of the two continuum phases; however, as stated by Wilmanski [2008] and Klika [2014], the physical basis of these fields is poorly defined. We therefore rely on the intuition developed in Gurtin et al. [2010] to develop the governing thermodynamic laws of the continuum mixture. Then, through careful consideration of microscopic flow behavior, experimental observations, and the results of particle simulations, we develop the constitutive laws governing the phase stresses in Equations (2.17) and (2.18). In Section 3, we verify that these relations recover the empirical limiting behaviors of fluid-sediment mixtures. For this formulation, we return to the continuum representation of the mixture shown in Figure 2-2. In particular, we are interested in the behavior of a part of the mixture defined by a volume Ω.

2.3.1 First Law of Thermodynamics

The first law of thermodynamics states that the rate of change of the *total energy* stored within a volume must be equal to the rate of *heat flow* into the volume plus the *external power* exerted on the volume. The total energy stored within a volume is the sum of *internal energy* and *kinetic energy*. We consider the part of the solid body defined by the volume Ω,

and we express the conservation of energy of this part as follows,

$$\frac{D^s}{Dt}\Big(\mathcal{E}_s(\Omega) + \mathcal{K}_s(\Omega)\Big) = \mathcal{Q}_s(\Omega) + \mathcal{W}_s(\Omega) - \mathcal{Q}_i(\Omega) - \mathcal{W}_i(\Omega) \tag{2.40}$$

where,

- $\mathcal{E}_s(\Omega)$ is the *internal energy* of the solid part.
- $\mathcal{K}_s(\Omega)$ is the *kinetic energy* of the solid part.
- $\mathcal{Q}_s(\Omega)$ is the *external heat flow* into the solid part.
- $\mathcal{W}_s(\Omega)$ is the *external power* exerted on the solid part.
- $\mathcal{Q}_i(\Omega)$ is the *inter-phase heat flow* from the solid part to fluid part (defined by the volume Ω).
- $\mathcal{W}_i(\Omega)$ is the *inter-phase work power* exerted on the fluid part by the solid part.

We also consider the part of the fluid body defined by the volume Ω and express energy conservation of this part similarly,

$$\frac{D^f}{Dt}\Big(\mathcal{E}_f(\Omega) + \mathcal{K}_f(\Omega)\Big) = \mathcal{Q}_f(\Omega) + \mathcal{W}_f(\Omega) + \mathcal{Q}_i(\Omega) + \mathcal{W}_i(\Omega) \tag{2.41}$$

where,

- $\mathcal{E}_f(\Omega)$ is the *internal energy* of the fluid part.
- $\mathcal{K}_f(\Omega)$ is the *kinetic energy* of the fluid part.
- $\mathcal{Q}_f(\Omega)$ is the *external heat flow* into the fluid part.
- $\mathcal{W}_f(\Omega)$ is the *external power* exerted on the fluid part.

Summing the expressions for phase-wise energy conservation in Equations (2.40) and (2.41), we arrive at the expression for the combined conservation of energy in the mixed volume, Ω,

$$\frac{D^s}{Dt}\Big(\mathcal{E}_s(\Omega) + \mathcal{K}_s(\Omega)\Big) + \frac{D^f}{Dt}\Big(\mathcal{E}_f(\Omega) + \mathcal{K}_f(\Omega)\Big) = \mathcal{Q}_s(\Omega) + \mathcal{Q}_f(\Omega) + \mathcal{W}_s(\Omega) + \mathcal{W}_f(\Omega) \tag{2.42}$$

We let the *internal energies*, $\mathcal{E}_s(\Omega)$ and $\mathcal{E}_f(\Omega)$, be defined by integrating the *specific internal energies*, ε_s and ε_f over the volume Ω,

$$\begin{aligned} \mathcal{E}_s(\Omega) &= \int_\Omega \bar{\rho}_s \varepsilon_s dv \\ \mathcal{E}_f(\Omega) &= \int_\Omega \bar{\rho}_f \varepsilon_f dv \end{aligned} \tag{2.43}$$

We let the *kinetic energies*, $\mathcal{K}_s(\Omega)$ and $\mathcal{K}_f(\Omega)$, be similarly defined by integrating the *specific kinetic energies* over the volume Ω,

$$\begin{aligned} \mathcal{K}_s(\Omega) &= \int_\Omega \frac{1}{2}\bar{\rho}_s(\mathbf{v_s}\cdot\mathbf{v_s})dv \\ \mathcal{K}_f(\Omega) &= \int_\Omega \frac{1}{2}\bar{\rho}_f(\mathbf{v_f}\cdot\mathbf{v_f})dv \end{aligned} \tag{2.44}$$

The *external heat flows*, $\mathcal{Q}_s(\Omega)$ and $\mathcal{Q}_f(\Omega)$, are characterized by the phase-wise *external heat fluxes*, $\mathbf{q_s}$ and $\mathbf{q_f}$, at the boundary $\partial\Omega$ and phase-wise *internal heat generation*, q_s and q_f, within the volume Ω as follows,

$$\begin{aligned} \mathcal{Q}_s(\Omega) &= -\int_{\partial\Omega}(\mathbf{q_s}\cdot\mathbf{n})da + \int_\Omega q_s dv \\ \mathcal{Q}_f(\Omega) &= -\int_{\partial\Omega}(\mathbf{q_f}\cdot\mathbf{n})da + \int_\Omega q_f dv \end{aligned} \tag{2.45}$$

We also define an *inter-phase heat flow*, $\mathcal{Q}_i(\Omega)$, in terms of the *inter-phase heat transfer*, q_i (volume averaged heat transfer from the solid phase to the fluid phase),

$$\mathcal{Q}_i(\Omega) = \int_\Omega q_i dv \tag{2.46}$$

For the *external powers*, $\mathcal{W}_s(\Omega)$ and $\mathcal{W}_f(\Omega)$, we return to the definition of the phase stresses in Equation (2.4) and the expression for external body forces in Equation (2.3) to define,

$$\begin{aligned} \mathcal{W}_s(\Omega) &= \int_{\partial\Omega}(\boldsymbol{\sigma_s}\mathbf{n}\cdot\mathbf{v_s})da + \int_\Omega(\bar{\rho}_s\mathbf{g}\cdot\mathbf{v_s})dv \\ \mathcal{W}_f(\Omega) &= \int_{\partial\Omega}(\boldsymbol{\sigma_f}\mathbf{n}\cdot\mathbf{v_f})da + \int_\Omega(\bar{\rho}_f\mathbf{g}\cdot\mathbf{v_s})dv \end{aligned} \tag{2.47}$$

To simplify the analysis of the combined conservation of energy in Equation (2.42), we will apply the definitions given above to each term individually, then recombine all the terms at the end. This will allow us to cleanly derive an integral expression for the combined conservation of energy within a mixed volume Ω. We begin this analysis with the first term, the time rate of change of the total energy stored in the solid part defined by the volume Ω. Using the relations for internal and kinetic energies from Equations (2.43) and (2.44), we can rewrite this term as,

$$\frac{D^f}{Dt}\Big(\mathcal{E}_f(\Omega)+\mathcal{K}_f(\Omega)\Big) = \frac{D^s}{Dt}\Big(\int_\Omega \bar{\rho}_s\big(\varepsilon_s+\frac{1}{2}(\mathbf{v_s}\cdot\mathbf{v_s})\big)dv\Big)$$

Applying Reynolds' transport relation, we find,

$$\int_\Omega \left[\frac{D^s}{Dt}\left(\bar{\rho}_s\left(\varepsilon_s + \frac{1}{2}(\mathbf{v_s}\cdot\mathbf{v_s})\right)\right) + \bar{\rho}_s\left(\varepsilon_s + \frac{1}{2}(\mathbf{v_s}\cdot\mathbf{v_s})\right)\operatorname{div}(\mathbf{v_s})\right] dv$$

which is equivalent to,

$$\int_\Omega \left[\left(\frac{D^s\bar{\rho}_s}{Dt} + \bar{\rho}_s\operatorname{div}(\mathbf{v_s})\right)\left(\varepsilon_s + \frac{1}{2}(\mathbf{v_s}\cdot\mathbf{v_s})\right) + \bar{\rho}_s\frac{D^s}{Dt}\left(\varepsilon_s + \frac{1}{2}(\mathbf{v_s}\cdot\mathbf{v_s})\right)\right] dv$$

Using the expression for solid phase mass conservation from Equation (2.7), we get the final integral form for the rate of change of total energy in the solid part,

$$\frac{D^s}{Dt}\left(\mathcal{E}_s(\Omega) + \mathcal{K}_s(\Omega)\right) = \int_\Omega \left(\bar{\rho}_s\frac{D^s\varepsilon_s}{Dt} + \bar{\rho}_s\frac{D^s\mathbf{v_s}}{Dt}\cdot\mathbf{v_s}\right) dv \tag{2.48}$$

A similar analysis can be performed for the expression of material rate of change for the total energy in the fluid part defined by the volume Ω (the second term in Equation (2.42)); the result is given here,

$$\frac{D^f}{Dt}\left(\mathcal{E}_f(\Omega) + \mathcal{K}_f(\Omega)\right) = \int_\Omega \left(\bar{\rho}_f\frac{D^f\varepsilon_f}{Dt} + \bar{\rho}_f\frac{D^f\mathbf{v_f}}{Dt}\cdot\mathbf{v_f}\right) dv \tag{2.49}$$

Keeping these relations in mind, we continue through the terms in the combined expression for conservation of energy. The first and second terms on the right hand side of Equation (2.42) we recognize as the external power acting on the mixed volume Ω. Applying the definitions from Equation (2.47) to these terms, we find that,

$$\mathcal{W}_s(\Omega) + \mathcal{W}_f(\Omega) = \int_{\partial\Omega} (\boldsymbol{\sigma_s}\mathbf{n}\cdot\mathbf{v_s} + \boldsymbol{\sigma_f}\mathbf{n}\cdot\mathbf{v_f}) da + \int_\Omega (\bar{\rho}_s\mathbf{g}\cdot\mathbf{v_s} + \bar{\rho}_f\mathbf{g}\cdot\mathbf{v_f}) dv$$

Applying the divergence theorem to the above expression, we find the final integral form for the combined external power acting on the volume Ω.

$$\begin{aligned}\mathcal{W}_s(\Omega) + \mathcal{W}_f(\Omega) = &\int_\Omega \left[(\operatorname{div}(\boldsymbol{\sigma_s}) + \bar{\rho}_s\mathbf{g})\cdot\mathbf{v_s} + (\operatorname{div}(\boldsymbol{\sigma_f}) + \bar{\rho}_f\mathbf{g})\cdot\mathbf{v_f}\right] dv \\ &+ \int_\Omega \left[\boldsymbol{\sigma_s} : \operatorname{grad}(\mathbf{v_s}) + \boldsymbol{\sigma_f} : \operatorname{grad}(\mathbf{v_f})\right] dv\end{aligned} \tag{2.50}$$

Lastly, we consider the third and fourth terms on the right hand side of Equation (2.42). These are the expressions for the external heat flow into the mixed volume Ω. Applying the definitions from Equation (2.45) to these terms, we find that,

$$\mathcal{Q}_s(\Omega) + \mathcal{Q}_f(\Omega) = -\int_{\partial\Omega} (\mathbf{q_s}\cdot\mathbf{n} + \mathbf{q_f}\cdot\mathbf{n}) da + \int_\Omega (q_s + q_f) dv$$

Applying the divergence theorem to the above expression, we arrive at the final integral form for the combined heat flow into the volume Ω.

$$\mathcal{Q}_s(\Omega) + \mathcal{Q}_f(\Omega) = \int_\Omega \big(- \operatorname{div}(\mathbf{q_s} + \mathbf{q_f}) + q_s + q_f \big) dv \tag{2.51}$$

Substituting in the phase-wise energy conservation expressions from Equations (2.40), (2.41), (2.50), and (2.51) into the combined energy conservation expression in Equation (2.42), we find the integral form of the combined conservation of energy in the mixture,

$$\begin{aligned}\int_\Omega \left(\bar{\rho}_s \frac{D^s \varepsilon_s}{Dt} + \bar{\rho}_f \frac{D^f \varepsilon_f}{Dt} + \bar{\rho}_s \frac{D^s \mathbf{v_s}}{Dt} \cdot \mathbf{v_s} + \bar{\rho}_f \frac{D^f \mathbf{v_f}}{Dt} \cdot \mathbf{v_f} \right) dv = &\int_\Omega \big((\operatorname{div}(\boldsymbol{\sigma_s}) + \bar{\rho}_s \mathbf{g}) \cdot \mathbf{v_s} \big) dv \\ &+ \int_\Omega \big((\operatorname{div}(\boldsymbol{\sigma_f}) + \bar{\rho}_f \mathbf{g}) \cdot \mathbf{v_f} \big) dv \\ &+ \int_\Omega \boldsymbol{\sigma_s} : \operatorname{grad}(\mathbf{v_s}) dv \\ &+ \int_\Omega \boldsymbol{\sigma_f} : \operatorname{grad}(\mathbf{v_f}) dv \\ &+ \int_\Omega \big(q_s + q_f - \operatorname{div}(\mathbf{q_s} + \mathbf{q_f}) \big) dv \end{aligned} \tag{2.52}$$

Since this expression must hold for any choice of volume Ω, the strong form must also be true. From here, we continue our analysis without the need for pesky integral expressions.

$$\begin{aligned}\bar{\rho}_s \frac{D^s \varepsilon_s}{Dt} + \bar{\rho}_f \frac{D^f \varepsilon_f}{Dt} + \bar{\rho}_s \frac{D^s \mathbf{v_s}}{Dt} \cdot \mathbf{v_s} + \bar{\rho}_f \frac{D^f \mathbf{v_f}}{Dt} \cdot \mathbf{v_f} = &(\operatorname{div}(\boldsymbol{\sigma_s}) + \bar{\rho}_s \mathbf{g}) \cdot \mathbf{v_s} \\ &+ (\operatorname{div}(\boldsymbol{\sigma_f}) + \bar{\rho}_f \mathbf{g}) \cdot \mathbf{v_f} \\ &+ \boldsymbol{\sigma_s} : \operatorname{grad}(\mathbf{v_s}) + \boldsymbol{\sigma_f} : \operatorname{grad}(\mathbf{v_f}) \\ &+ q_s + q_f - \operatorname{div}(\mathbf{q_s} + \mathbf{q_f}) \end{aligned}$$

By momentum balance in Equation (2.16) and the definition of the buoyant term in Equation (2.20), this is equivalent to

$$\begin{aligned}\bar{\rho}_s \frac{D^s \varepsilon_s}{Dt} + \bar{\rho}_f \frac{D^f \varepsilon_f}{Dt} = &\, p_f \operatorname{grad}(n) \cdot (\mathbf{v_s} - \mathbf{v_f}) \\ &+ \mathbf{f_d} \cdot (\mathbf{v_s} - \mathbf{v_f}) \\ &+ \boldsymbol{\sigma_s} : \operatorname{grad}(\mathbf{v_s}) + \boldsymbol{\sigma_f} : \operatorname{grad}(\mathbf{v_f}) \\ &+ q_s + q_f - \operatorname{div}(\mathbf{q_s} + \mathbf{q_f}) \end{aligned}$$

Substituting in the expressions for the specific form of the phase stresses in Equations (2.17), (2.18), and (2.9), this further reduces to the final strong form expression for conservation of

energy in the mixture,

$$\begin{aligned}\bar{\rho}_s \frac{D^s \varepsilon_s}{Dt} + \bar{\rho}_f \frac{D^f \varepsilon_f}{Dt} = p_f \left(\frac{n}{\rho_f} \frac{D^f \rho_f}{Dt} \right) \\ + \mathbf{f_d} \cdot (\mathbf{v_s} - \mathbf{v_f}) \\ + \tilde{\boldsymbol{\sigma}} : \operatorname{grad}(\mathbf{v_s}) + \boldsymbol{\tau_f} : \operatorname{grad}(\mathbf{v_f}) \\ + q_s + q_f - \operatorname{div}(\mathbf{q_s} + \mathbf{q_f})\end{aligned} \tag{2.53}$$

2.3.2 Second Law of Thermodynamics

The second law of thermodynamics states that the rate of change of the *total entropy* within a volume Ω must always be greater than or equal to the *combined entropy flow* into the volume. Drumheller [2000] gives the following *necessary* condition for entropy imbalance of a mixed volume Ω,

$$\frac{D^s \mathcal{S}_s(\Omega)}{Dt} + \frac{D^f \mathcal{S}_f(\Omega)}{Dt} - \mathcal{J}_s(\Omega) - \mathcal{J}_f(\Omega) \geq 0 \tag{2.54}$$

We add two additional conditions by considering the entropy flow into the part of the solid body defined by the volume Ω,

$$\frac{D^s \mathcal{S}_s(\Omega)}{Dt} - \mathcal{J}_s(\Omega) + \mathcal{J}_{is}(\Omega) \geq 0 \tag{2.55}$$

and the entropy flow into the fluid of the solid body defined by the volume Ω,

$$\frac{D^f \mathcal{S}_f(\Omega)}{Dt} - \mathcal{J}_f(\Omega) - \mathcal{J}_{if}(\Omega) \geq 0 \tag{2.56}$$

where,

- $\mathcal{S}_s(\Omega)$ is the *entropy* of the solid part.
- $\mathcal{J}_s(\Omega)$ is the *external entropy flow* into the solid part.
- $\mathcal{S}_f(\Omega)$ is the *entropy* of the fluid part.
- $\mathcal{J}_f(\Omega)$ is the *external entropy flow* into the fluid part.
- $\mathcal{J}_{is}(\Omega)$ is the *inter-phase solid entropy flow* due to heat flowing from the solid part into fluid part (defined by the volume Ω).
- $\mathcal{J}_{if}(\Omega)$ is the *inter-phase fluid entropy flow* due to the heat flow into the fluid part from solid part.

Together, Equations (2.54), (2.55), and (2.56) give the *necessary* and *sufficient* conditions for satisfying the second law of thermodynamics within a mixed volume Ω. We now define

the integral forms of the terms in these expressions. We let the *total entropies*, $\mathcal{S}_s(\Omega)$ and $\mathcal{S}_f(\Omega)$, within a volume Ω be defined in terms of the phase-wise *specific entropies*, η_s and η_f,

$$\begin{aligned} \mathcal{S}_s(\Omega) &= \int_\Omega \bar{\rho}_s \eta_s dv \\ \mathcal{S}_f(\Omega) &= \int_\Omega \bar{\rho}_f \eta_f dv \end{aligned} \tag{2.57}$$

The first term in Equation (2.54) can be rewritten with the definition for the solid phase entropy in Equation (2.57) as follows,

$$\frac{D^s \mathcal{S}_s(\Omega)}{Dt} = \frac{D^s}{Dt} \int_\Omega \bar{\rho}_s \eta_s dv$$

Using Reynolds' transport relation,

$$\frac{D^s \mathcal{S}_s(\Omega)}{Dt} = \int_\Omega \left[\frac{D^s}{Dt}(\bar{\rho}_s \eta_s) + \bar{\rho}_s \eta_s \operatorname{div}(\mathbf{v_s}) \right] dv$$

which, by solid phase mass conservation in Equation (2.7), is equivalent to

$$\frac{D^s \mathcal{S}_s(\Omega)}{Dt} = \int_\Omega \bar{\rho}_s \frac{D^s \eta_s}{Dt} dv \tag{2.58}$$

By similarity, the second term in Equation (2.54) is equivalently,

$$\frac{D^f \mathcal{S}_f(\Omega)}{Dt} = \int_\Omega \bar{\rho}_f \frac{D^f \eta_f}{Dt} dv \tag{2.59}$$

We let the *external entropy flows*, $\mathcal{J}_s(\Omega)$ and $\mathcal{J}_f(\Omega)$, into the volume Ω be given as follows,

$$\begin{aligned} \mathcal{J}_s(\Omega) &= -\int_{\partial\Omega} \left(\frac{\mathbf{q_s}}{\vartheta_s} \cdot \mathbf{n} \right) da + \int_\Omega \frac{q_s}{\vartheta_s} dv \\ \mathcal{J}_f(\Omega) &= -\int_{\partial\Omega} \left(\frac{\mathbf{q_f}}{\vartheta_f} \cdot \mathbf{n} \right) da + \int_\Omega \frac{q_f}{\vartheta_f} dv \end{aligned}$$

which, by the divergence theorem, are equivalent to,

$$\begin{aligned} \mathcal{J}_s(\Omega) &= -\int_\Omega \left[\operatorname{div}\left(\frac{\mathbf{q_s}}{\vartheta_s} \right) - \frac{q_s}{\vartheta_s} \right] dv \\ \mathcal{J}_f(\Omega) &= -\int_\Omega \left[\operatorname{div}\left(\frac{\mathbf{q_f}}{\vartheta_f} \right) - \frac{q_f}{\vartheta_f} \right] dv \end{aligned} \tag{2.60}$$

where $\vartheta_s > 0$ and $\vartheta_f > 0$ are the phase-wise *absolute temperatures*.

Unlike the *inter-phase heat flow*, $\mathcal{Q}_i$, which represents the heat flow out of the solid phase

and into the fluid phase, the *inter-phase entropy flows*, $\mathcal{J}_{is}(\Omega)$ and $\mathcal{J}_{if}(\Omega)$, are *not* equal,

$$\begin{aligned}\mathcal{J}_{is}(\Omega) &= \int_{\Omega} \frac{q_i}{\vartheta_s} dv \\ \mathcal{J}_{if}(\Omega) &= \int_{\Omega} \frac{q_i}{\vartheta_f} dv\end{aligned} \tag{2.61}$$

Substituting in the expressions from Equations (2.58), (2.59), and (2.60) into Equation (2.54), we arrive at the integral form of the Drumheller entropy imbalance for the mixed volume Ω,

$$\int_{\Omega} \left[\bar{\rho_s} \frac{D^s \eta_s}{Dt} + \bar{\rho_f} \frac{D^f \eta_f}{Dt} + \operatorname{div}\left(\frac{\mathbf{q_s}}{\vartheta_s} + \frac{\mathbf{q_f}}{\vartheta_f} \right) - \frac{q_s}{\vartheta_s} - \frac{q_f}{\vartheta_f} \right] dv \geq 0$$

Since this must hold for any choice of volume Ω, the strong form must also be true. This is the first condition of entropy imbalance in the mixture,

$$\bar{\rho_s} \frac{D^s \eta_s}{Dt} + \bar{\rho_f} \frac{D^f \eta_f}{Dt} + \operatorname{div}\left(\frac{\mathbf{q_s}}{\vartheta_s} + \frac{\mathbf{q_f}}{\vartheta_f} \right) - \frac{q_s}{\vartheta_s} - \frac{q_f}{\vartheta_f} \geq 0 \tag{2.62}$$

For the second and third conditions, we substitute in the expressions for the phase-wise entropy integrals and entropy flow integrals from Equations (2.58), (2.59), (2.60), and (2.61) into the phase-wise entropy imbalance conditions in Equations (2.55) and (2.56) to find,

$$\int_{\Omega} \left[\bar{\rho_s} \frac{D^s \eta_s}{Dt} + \operatorname{div}\left(\frac{\mathbf{q_s}}{\vartheta_s} \right) - \frac{q_s - q_i}{\vartheta_s} \right] dv \geq 0$$

$$\int_{\Omega} \left[\bar{\rho_f} \frac{D^f \eta_f}{Dt} + \operatorname{div}\left(\frac{\mathbf{q_f}}{\vartheta_f} \right) - \frac{q_f + q_i}{\vartheta_f} \right] dv \geq 0$$

Since these expressions must hold for any choice of volume Ω, the strong form conditions must also be true,

$$\begin{aligned}\bar{\rho_s} \frac{D^s \eta_s}{Dt} + \operatorname{div}\left(\frac{\mathbf{q_s}}{\vartheta_s} \right) - \frac{q_s - q_i}{\vartheta_s} &\geq 0 \\ \bar{\rho_f} \frac{D^f \eta_f}{Dt} + \operatorname{div}\left(\frac{\mathbf{q_f}}{\vartheta_f} \right) - \frac{q_f + q_i}{\vartheta_f} &\geq 0\end{aligned} \tag{2.63}$$

These can be re-expressed equivalently as,

$$\bar{\rho_s} \vartheta_s \frac{D^s \eta_s}{Dt} - \mathbf{q_s} \cdot \left(\frac{\operatorname{grad}(\vartheta_s)}{\vartheta_s} \right) + \operatorname{div}(\mathbf{q_s}) - q_s + q_i \geq 0$$

$$\bar{\rho_f} \vartheta_f \frac{D^f \eta_f}{Dt} - \mathbf{q_f} \cdot \left(\frac{\operatorname{grad}(\vartheta_f)}{\vartheta_f} \right) + \operatorname{div}(\mathbf{q_f}) - q_f - q_i \geq 0$$

which when summed gives us the final strong form condition for entropy imbalance for the

mixture,

$$\bar{\rho}_s\vartheta_s\frac{D^s\eta_s}{Dt}+\bar{\rho}_f\vartheta_f\frac{D^f\eta_f}{Dt}-\left(\frac{\mathbf{q_s}\cdot\mathrm{grad}(\vartheta_s)}{\vartheta_s}+\frac{\mathbf{q_f}\cdot\mathrm{grad}(\vartheta_f)}{\vartheta_f}\right)+\mathrm{div}(\mathbf{q_s}+\mathbf{q_f})-(q_s+q_f)\geq 0 \quad (2.64)$$

2.3.3 Rules for Inter-Phase Heat Transfer

Though it is not used later in this work, Equations (2.62) and (2.63) have an important consequence on the form of the *inter-phase heat transfer*, q_i. In particular, we observe that the sum of the expressions in Equation (2.63) yields,

$$\bar{\rho}_s\frac{D^s\eta_s}{Dt}+\bar{\rho}_f\frac{D^f\eta_f}{Dt}+\mathrm{div}\left(\frac{\mathbf{q_s}}{\vartheta_s}+\frac{\mathbf{q_f}}{\vartheta_f}\right)-\frac{q_s}{\vartheta_s}-\frac{q_f}{\vartheta_f}+q_i\left(\frac{\vartheta_s-\vartheta_f}{\vartheta_s\vartheta_f}\right)\geq 0$$

which, when compared with Equation (2.62),

$$\bar{\rho}_s\frac{D^s\eta_s}{Dt}+\bar{\rho}_f\frac{D^f\eta_f}{Dt}+\mathrm{div}\left(\frac{\mathbf{q_s}}{\vartheta_s}+\frac{\mathbf{q_f}}{\vartheta_f}\right)-\frac{q_s}{\vartheta_s}-\frac{q_f}{\vartheta_f}\geq 0$$

implies the result,

$$q_i\left(\frac{\vartheta_s-\vartheta_f}{\vartheta_s\vartheta_f}\right)\geq 0$$

or, equivalently,

$$\mathrm{sgn}(q_i)=\mathrm{sgn}(\vartheta_s-\vartheta_f)$$

This matches the intuition that the heat transfer *from* the solid phase *into* the fluid phase must have the same sign as the difference in temperature between the solid and fluid phases. That is, heat will flow from the solid phase to the fluid phase only when the solid phase temperature is greater than the fluid phase temperature.

2.3.4 Helmholtz Free Energy

We now introduce the definition for the phase-wise Helmholtz free energies, ψ_s and ψ_f,

$$\begin{aligned}\psi_s&=\varepsilon_s-\eta_s\vartheta_s\\ \psi_f&=\varepsilon_f-\eta_f\vartheta_f\end{aligned} \quad (2.65)$$

or, equivalently,

$$\begin{aligned}\varepsilon_s&=\psi_s+\eta_s\vartheta_s\\ \varepsilon_f&=\psi_f+\eta_f\vartheta_f\end{aligned}$$

Therefore, the material derivatives of the phase-wise internal energies in Equation (2.53) can be re-expressed as follows,

$$\frac{D^s\varepsilon_s}{Dt} = \frac{D^s\psi_s}{Dt} + \vartheta_s\frac{D^s\eta_s}{Dt} + \eta_s\frac{D^s\vartheta_s}{Dt}$$

$$\frac{D^f\varepsilon_f}{Dt} = \frac{D^f\psi_f}{Dt} + \vartheta_f\frac{D^f\eta_f}{Dt} + \eta_f\frac{D^f\vartheta_f}{Dt}$$

which, when substituted into Equation (2.53), results in the following expression for conservation of energy in the mixture,

$$\begin{aligned}\bar{\rho}_s\vartheta_s\frac{D^s\eta_s}{Dt} + \bar{\rho}_f\vartheta_f\frac{D^f\eta_f}{Dt} = &-\bar{\rho}_s\frac{D^s\psi_s}{Dt} - \bar{\rho}_f\frac{D^f\psi_f}{Dt}\\ &-\bar{\rho}_s\eta_s\frac{D^s\vartheta_s}{Dt} - \bar{\rho}_f\eta_f\frac{D^f\vartheta_f}{Dt}\\ &+p_f\left(\frac{n}{\rho_f}\frac{D^f\rho_f}{Dt}\right)\\ &+\mathbf{f_d}\cdot(\mathbf{v_s}-\mathbf{v_f})\\ &+\tilde{\boldsymbol{\sigma}}:\mathrm{grad}(\mathbf{v_s}) + \boldsymbol{\tau_f}:\mathrm{grad}(\mathbf{v_f})\\ &+q_s + q_f - \mathrm{div}(\mathbf{q_s}+\mathbf{q_f})\end{aligned}$$

Combining this expression with the expression of entropy imbalance in Equation (2.64), the following free energy inequality is found,

$$\begin{aligned}0 \leq &-\bar{\rho}_s\frac{D^s\psi_s}{Dt} - \bar{\rho}_f\frac{D^f\psi_f}{Dt}\\ &-\bar{\rho}_s\eta_s\frac{D^s\vartheta_s}{Dt} - \bar{\rho}_f\eta_f\frac{D^f\vartheta_f}{Dt}\\ &+p_f\left(\frac{n}{\rho_f}\frac{D^f\rho_f}{Dt}\right)\\ &+\mathbf{f_d}\cdot(\mathbf{v_s}-\mathbf{v_f})\\ &+\tilde{\boldsymbol{\sigma}}:\mathrm{grad}(\mathbf{v_s}) + \boldsymbol{\tau_f}:\mathrm{grad}(\mathbf{v_f})\\ &-\frac{\mathbf{q_s}\cdot\mathrm{grad}(\vartheta_s)}{\vartheta_s} - \frac{\mathbf{q_f}\cdot\mathrm{grad}(\vartheta_f)}{\vartheta_f}\end{aligned} \tag{2.66}$$

2.3.5 Isothermal Assumption

In this work we assume that the solid and fluid phases have uniform and constant temperatures, ϑ_s and ϑ_f.

$$\frac{D^s\vartheta_s}{Dt} = \frac{D^f\vartheta_f}{Dt} = 0$$

and,

$$\text{grad}(\vartheta_s) = \text{grad}(\vartheta_f) = \mathbf{0}$$

These simplifications reduce the statement of free energy imbalance in Equation (2.66) to the following form,

$$\begin{aligned} 0 \leq & -\bar{\rho}_s \frac{D^s \psi_s}{Dt} - \bar{\rho}_f \frac{D^f \psi_f}{Dt} \\ & + p_f \left(\frac{n}{\rho_f} \frac{D^f \rho_f}{Dt} \right) \\ & + \tilde{\boldsymbol{\sigma}} : \text{grad}(\mathbf{v_s}) + \boldsymbol{\tau_f} : \text{grad}(\mathbf{v_f}) \\ & + \mathbf{f_d} \cdot (\mathbf{v_s} - \mathbf{v_f}) \end{aligned} \tag{2.67}$$

2.3.6 Strain-Rate Definitions

We let the spatial fluid phase velocity gradient be expressed as,

$$\mathbf{L_f} \equiv \text{grad}(\mathbf{v_f})$$

which has a unique decomposition into a fluid spin tensor, $\mathbf{W_f}$, and a fluid strain-rate tensor, $\mathbf{D_f}$, such that

$$\mathbf{L_f} = \mathbf{D_f} + \mathbf{W_f}$$

and,

$$\mathbf{D_f} = \text{sym}(\mathbf{L_f}) = \frac{1}{2}(\mathbf{L_f} + \mathbf{L_f}^\top)$$

$$\mathbf{W_f} = \text{skw}(\mathbf{L_f}) = \frac{1}{2}(\mathbf{L_f} - \mathbf{L_f}^\top)$$

We previously stated that the fluid shear stress tensor, $\boldsymbol{\tau_f}$, is assumed to be symmetric and deviatoric. Therefore, the contraction of this tensor with the fluid phase velocity gradient can be re-expressed,

$$\boldsymbol{\tau_f} : \text{grad}(\mathbf{v_f}) = \boldsymbol{\tau_f} : \mathbf{D_{0f}} \tag{2.68}$$

where $\mathbf{D_{0f}}$ is the deviatoric part of the fluid strain-rate tensor.

The solid phase velocity gradient is similarly defined,

$$\mathbf{L_p} \equiv \text{grad}(\mathbf{v_s})$$

which is expressible in terms of the solid spin tensor, $\mathbf{W_s}$, and the solid strain-rate tensor, $\mathbf{D_s}$, such that,

$$\mathbf{L_s} = \mathbf{D_s} + \mathbf{W_s}$$

and,

$$\mathbf{D_s} = \text{sym}(\mathbf{L_s}) = \frac{1}{2}(\mathbf{L_s} + \mathbf{L_s}^\top)$$

$$\mathbf{W_s} = \text{skw}(\mathbf{L_s}) = \frac{1}{2}(\mathbf{L_s} - \mathbf{L_s}^\top)$$

The solid phase effective granular stress, $\tilde{\boldsymbol{\sigma}}$, is symmetric but not deviatoric. Therefore the contraction of this tensor with the solid phase velocity gradient can be re-expressed,

$$\tilde{\boldsymbol{\sigma}} : \text{grad}(\mathbf{v_s}) = \tilde{\boldsymbol{\sigma}} : \mathbf{D_s} \tag{2.69}$$

Substituting in the expressions from Equations (2.68) and (2.69) into the free energy imbalance statement in Equation (2.67), we find,

$$-\bar{\rho}_s \frac{D^s \psi_s}{Dt} - \bar{\rho}_f \frac{D^f \psi_f}{Dt} + p_f \left(\frac{n}{\rho_f} \frac{D^f \rho_f}{Dt} \right) + (\tilde{\boldsymbol{\sigma}} : \mathbf{D_s}) + (\boldsymbol{\tau_f} : \mathbf{D_{0f}}) + \mathbf{f_d} \cdot (\mathbf{v_s} - \mathbf{v_f}) \geq 0 \tag{2.70}$$

2.3.7 Fluid Phase Free Energy Function

The conservative constitutive behavior of the fluid phase is governed by the fluid phase specific free energy, ψ_f. We assume that the functional form of the free energy only depends on the true fluid density ρ_f,

$$\psi_f = \hat{\psi}_f(\rho_f)$$

The material derivative of this function,

$$\frac{D^f \hat{\psi}_f(\rho_f)}{Dt} = \frac{\partial \hat{\psi}_f(\rho_f)}{\partial \rho_f} \frac{D^f \rho_f}{Dt}$$

can be substituted into the expression for free energy imbalance in Equation (2.70), to find,

$$-\bar{\rho}_s \frac{D^s \psi_s}{Dt} + (\tilde{\boldsymbol{\sigma}} : \mathbf{D_s}) - \frac{n}{\rho_f} \frac{D^f \rho_f}{Dt} \left(p_f - \rho_f^2 \frac{\partial \hat{\psi}_f(\rho_f)}{\partial \rho_f} \right) + (\boldsymbol{\tau_f} : \mathbf{D_{0f}}) + \mathbf{f_d} \cdot (\mathbf{v_s} - \mathbf{v_f}) \geq 0 \tag{2.71}$$

2.3.8 Solid Phase Free Energy Function

The solid phase behavior will be governed by an elastic-plastic constitutive relation derived from that given in Anand and Su [2005]. We begin with the definition of the solid phase deformation gradient,

$$\mathbf{F} = \frac{\partial \boldsymbol{\chi_s}(\mathbf{X}, t)}{\partial \mathbf{X}}$$

where $\boldsymbol{\chi_s}(\mathbf{X}, t)$ is the motion function mapping from a position, $\mathbf{X}$, in the reference configuration to a position in the deformed (current) configuration at time t. It follows that the material derivative of the deformation gradient can be expressed in terms of the solid phase velocity gradient,

$$\frac{D^s \mathbf{F}}{Dt} = \mathbf{L_s F}$$

We continue this formulation using the Kroner-Lee decomposition of the deformation gradient,

$$\mathbf{F} = \mathbf{F^e F^p}$$

With this, the velocity gradient can be separated into an *elastic* and *plastic* flow,

$$\mathbf{L_s} = \mathbf{L^e} + \mathbf{F^e L^p F^{e-1}} \tag{2.72}$$

with,

$$\frac{D^s \mathbf{F^e}}{Dt} = \mathbf{L^e F^e}, \quad \frac{D^s \mathbf{F^p}}{Dt} = \mathbf{L^p F^p}$$

As with the solid and fluid phase velocity gradients, we define

$$\mathbf{D^e} = \text{sym}(\mathbf{L^e}), \quad \mathbf{W^e} = \text{skw}(\mathbf{L^e})$$

$$\mathbf{D^p} = \text{sym}(\mathbf{L^p}), \quad \mathbf{W^p} = \text{skw}(\mathbf{L^p})$$

such that $\mathbf{L^e} = \mathbf{D^e} + \mathbf{W^e}$ and $\mathbf{L^p} = \mathbf{D^p} + \mathbf{W^p}$. It is also necessary in this analysis to define the right polar decomposition of the elastic deformation,

$$\mathbf{F^e} = \mathbf{R^e U^e} \tag{2.73}$$

with $\mathbf{R^e}$ an orthogonal tensor and $\mathbf{U^e}$ a symmetric positive definite *elastic stretch* tensor. The right Cauchy-Green tensor is then,

$$\mathbf{C^e} = \mathbf{U^{e2}} = \mathbf{F^{e\top} F^e} \tag{2.74}$$

Since $\mathbf{U^e}$ is symmetric and positive definite, it admits the spectral decomposition,

$$\mathbf{U^e} = \sum_{\alpha=1}^{3} \lambda_\alpha \mathbf{r}_\alpha \otimes \mathbf{r}_\alpha$$

where $\{\lambda_\alpha\}$ are the principal stretches, $\{\mathbf{r}_\alpha\}$ are the principal directions, and each $\lambda_\alpha > 0$. This allows us to define a *logarithmic strain tensor*,

$$\mathbf{E^e} = \ln(\mathbf{U^e}) = \sum_{\alpha=1}^{3} \ln(\lambda_\alpha) \mathbf{r}_\alpha \otimes \mathbf{r}_\alpha \tag{2.75}$$

Further we define,

$$J \equiv \det(\mathbf{F}) = J^e J^p > 0$$

with,

$$J^e \equiv \det(\mathbf{F^e}) > 0, \quad J^p \equiv \det(\mathbf{F^p}) > 0$$

and,

$$\frac{D^s J}{Dt} = \mathrm{tr}(\mathbf{L_s}), \quad \frac{D^s J^e}{Dt} = \mathrm{tr}(\mathbf{L^e}), \quad \frac{D^s J^p}{Dt} = \mathrm{tr}(\mathbf{L^p})$$

Here we introduce the solid phase *volumetric free energy*, φ_s, which we let take the form,

$$\varphi_s = J^e \bar{\rho}_s \psi_s \tag{2.76}$$

such that this free energy function takes a form similar to that given in Anand and Su [2005],

$$\varphi_s = \hat{\varphi}_s(\mathbf{C^e}) = \tilde{\varphi}_s(\mathbf{E^e}) \tag{2.77}$$

Taking the material derivative of the volumetric free energy, and using the conservation of mass expression from Equation (2.7), the following identity is found

$$\bar{\rho}_s \frac{D^s \psi_s}{Dt} = J^{e-1}\left(\frac{D^s \varphi_s}{Dt} - \varphi_s \,\mathrm{tr}(\mathbf{D^p})\right) \tag{2.78}$$

Further, the functional form of the free energy function given by $\hat{\varphi}_s(\mathbf{C^e})$ allows us to re-express the material derivative above,

$$\frac{D^s \varphi_s}{Dt} = \frac{D^s \hat{\varphi}_s(\mathbf{C^e})}{Dt} = \frac{\partial \hat{\varphi}_s(\mathbf{C^e})}{\partial \mathbf{C^e}} : \frac{D^s \mathbf{C^e}}{Dt}$$

which is equivalent to,

$$\frac{D^s \varphi_s}{Dt} = 2\mathbf{F^e}\frac{\partial \hat{\varphi}_s(\mathbf{C^e})}{\partial \mathbf{C^e}}\mathbf{F^{e\top}} : \mathbf{D^e}$$

and therefore the material derivative of the solid phase *specific free energy* from Equations (2.65) and (2.78) is given by,

$$\bar{\rho}_s \frac{D^s \psi_s}{Dt} = \left(2J^{e-1}\mathbf{F^e}\frac{\partial \hat{\varphi}_s(\mathbf{C^e})}{\partial \mathbf{C^e}}\mathbf{F^{e\top}}\right) : \mathbf{D^e} + (J^{e-1}\varphi_s \mathbf{1}) : \mathbf{D^p} \tag{2.79}$$

Substituting Equation (2.79) into the free energy imbalance expression in Equation (2.71), we find

$$\begin{aligned}\left(\tilde{\boldsymbol{\sigma}} - 2J^{e-1}\mathbf{F^e}\frac{\partial \hat{\varphi}_s(\mathbf{C^e})}{\partial \mathbf{C^e}}\mathbf{F^{e\top}}\right) : \mathbf{D^e} + \left(\tilde{\boldsymbol{\sigma}} : (\mathbf{F^e D^p F^{e-1}}) - (J^{e-1}\varphi_s \mathbf{1}) : \mathbf{D^p}\right) \\ -\frac{n}{\rho_f}\frac{D^f \rho_f}{Dt}\left(p_f - \rho_f^2 \frac{\partial \hat{\psi}_f(\rho_f)}{\partial \rho_f}\right) + (\boldsymbol{\tau_f} : \mathbf{D_{0f}}) + \mathbf{f_d} \cdot (\mathbf{v_s} - \mathbf{v_f}) \geq 0\end{aligned} \tag{2.80}$$

2.3.9 Rules for Constitutive Relations

The expression in Equation (2.80) results in very useful rules governing admissible constitutive relations for the mixture. Since it is possible to conceive of mixture motions with independently varying (and possibly vanishing) values for $\mathbf{D^e}$, $\mathbf{D^p}$, $D^s\rho_f/Dt$, $\mathbf{D_{0f}}$, and $(\mathbf{v_s} - \mathbf{v_f})$,

the following relations must each individually be satisfied,

$$\tilde{\boldsymbol{\sigma}} - 2J^{e-1}\mathbf{F^e}\frac{\partial\hat{\varphi}_s(\mathbf{C^e})}{\partial\mathbf{C^e}}\mathbf{F^{e\top}} = 0 \tag{2.81}$$

$$p_f - \rho_f^2\frac{\partial\hat{\psi}_f(\rho_f)}{\partial\rho_f} = 0 \tag{2.82}$$

$$\tilde{\boldsymbol{\sigma}} : (\mathbf{F^e}\mathbf{D^p}\mathbf{F^{e-1}}) - (J^{e-1}\varphi_s\mathbf{1}) : \mathbf{D^p} \geq 0 \tag{2.83}$$

$$\boldsymbol{\tau_f} : \mathbf{D_{0f}} \geq 0 \tag{2.84}$$

$$\mathbf{f_d} \cdot (\mathbf{v_s} - \mathbf{v_f}) \geq 0 \tag{2.85}$$

2.3.10 Rules for Drag Law

The inter-phase viscous drag, $\mathbf{f_d}$, must obey the dissipative inequality given in Equation (2.85).

$$\mathbf{f_d} \cdot (\mathbf{v_s} - \mathbf{v_f}) \geq 0$$

In Section 2.2, we find a functional form for $\mathbf{f_d}$ which is given in Equation (2.39) as,

$$\mathbf{f_d} = \frac{18\phi(1-\phi)\eta_0}{d^2} \cdot \hat{F}(\phi, \mathrm{Re}) \cdot (\mathbf{v_s} - \mathbf{v_f})$$

Therefore,

$$\frac{18\phi(1-\phi)\eta_0}{d^2} \cdot \hat{F}(\phi, \mathrm{Re}) \cdot \|\mathbf{v_s} - \mathbf{v_f}\|^2 \geq 0$$

which places the following constraint on the drag function $\hat{F}(\phi, \mathrm{Re})$,

$$\hat{F}(\phi, \mathrm{Re}) \geq 0$$

This rule is clearly satisfied by the expressions in Equations (2.37) and (2.38).

2.3.11 Fluid Phase Pore Pressure

The fluid phase pore pressure is governed by the constitutive relation given in Equation (2.82),

$$p_f - \rho_f^2\frac{\partial\hat{\psi}_f(\rho_f)}{\partial\rho_f} = 0$$

or, equivalently,

$$p_f = \rho_f^2\frac{\partial\hat{\psi}_f(\rho_f)}{\partial\rho_f}$$

We let the fluid phase free energy function, $\hat{\psi}(\rho_f)$, be given by,

$$\hat{\psi}_f(\rho_f) = \kappa\left(\frac{\ln(\rho_{0f}) - \ln(\rho_f) - 1}{\rho_f^2}\right) \tag{2.86}$$

such that,

$$\frac{\partial\hat{\psi}_f(\rho_f)}{\partial\rho_f} = \kappa\left(\frac{\ln(\rho_f) - \ln(\rho_{0f})}{\rho_f^2}\right)$$

Therefore the fluid phase pore pressure is given by the expression,

$$p_f = \kappa \ln\left(\frac{\rho_f}{\rho_{0f}}\right) \tag{2.87}$$

where ρ_{0f} is the true fluid density for which $p_f = 0$.

2.3.12 Fluid Phase Shear Stress

We assume that the functional form of $\boldsymbol{\tau_f}$ is given by,

$$\boldsymbol{\tau_f} = \hat{\boldsymbol{\tau}}_{\boldsymbol{f}}(\mathbf{D_{0f}}, \phi)$$

with $\hat{\boldsymbol{\tau}}_{\boldsymbol{f}}$ isotropic and linear in $\mathbf{D_{0f}}$. From Truesdell and Noll [1965], the representation theorem for isotropic linear tensor functions yields,

$$\hat{\boldsymbol{\tau}}_{\boldsymbol{f}}(\mathbf{D_{0f}}, \phi) = 2\mu(\phi)\mathbf{D_{0f}} + \lambda(\phi)\,\mathrm{tr}(\mathbf{D_{0f}})\mathbf{1}$$

Since $\mathbf{D_{0f}}$ is deviatoric, $\mathrm{tr}(\mathbf{D_{0f}}) = 0$. By the inequality in Equation (2.84), we require that,

$$2\mu(\phi)\|\mathbf{D_{0f}}\|^2 \geq 0$$

or,

$$\mu(\phi) \geq 0$$

We let the effective fluid phase viscosity, $\mu(\phi)$, be given by the linear relation from Einstein [1906] such that,

$$\boldsymbol{\tau_f} = 2\eta_0\left(1 + \tfrac{5}{2}\phi\right)\mathbf{D_{0f}} \tag{2.88}$$

with η_0 defined previously as the *true* fluid viscosity (i.e. the viscosity of the fluid without suspended grains).

2.3.13 Solid Phase Effective Granular Stress

The solid phase effective granular stress $\tilde{\boldsymbol{\sigma}}$ is constrained by the thermodynamic rules set in Equations (2.81) and (2.83). We begin with the equality in Equation (2.81),

$$\tilde{\boldsymbol{\sigma}} - 2J^{e-1}\mathbf{F}^{\mathbf{e}}\frac{\partial\hat{\varphi}_s(\mathbf{C}^{\mathbf{e}})}{\partial\mathbf{C}^{\mathbf{e}}}\mathbf{F}^{\mathbf{e}\top} = 0$$

which is equivalently,

$$\tilde{\boldsymbol{\sigma}} = 2J^{e-1}\mathbf{F}^{\mathbf{e}}\frac{\partial\hat{\varphi}_s(\mathbf{C}^{\mathbf{e}})}{\partial\mathbf{C}^{\mathbf{e}}}\mathbf{F}^{\mathbf{e}\top} \tag{2.89}$$

We define an elastic stress measure, $\mathbf{T}^{\mathbf{e}}$, such that,

$$\mathbf{T}^{\mathbf{e}} = J^{e}\mathbf{F}^{\mathbf{e}\top}\tilde{\boldsymbol{\sigma}}\mathbf{F}^{\mathbf{e}-\top} \tag{2.90}$$

By Equations (2.89), (2.90), and (2.74),

$$\mathbf{T}^{\mathbf{e}} = 2\mathbf{C}^{\mathbf{e}}\frac{\partial\hat{\varphi}_s(\mathbf{C}^{\mathbf{e}})}{\partial\mathbf{C}^{\mathbf{e}}} \tag{2.91}$$

and as shown in Anand and Su [2005], this is equivalent to,

$$\mathbf{T}^{\mathbf{e}} = \frac{\partial\tilde{\varphi}_s(\mathbf{E}^{\mathbf{e}})}{\partial\mathbf{E}^{\mathbf{e}}} \tag{2.92}$$

Here we let the solid phase free energy function have the form,

$$\tilde{\varphi}_s(\mathbf{E}^{\mathbf{e}}) = G\|\mathbf{E}^{\mathbf{e}}_{\mathbf{0}}\|^2 + \tfrac{1}{2}K\,\mathrm{tr}(\mathbf{E}^{\mathbf{e}})^2 \tag{2.93}$$

where $\|\mathbf{E}^{\mathbf{e}}_{\mathbf{0}}\|^2 = \mathbf{E}^{\mathbf{e}}_{\mathbf{0}} : \mathbf{E}^{\mathbf{e}}_{\mathbf{0}}$. Therefore, the elastic stress $\mathbf{T}^{\mathbf{e}}$ is given by,

$$\mathbf{T}^{\mathbf{e}} = 2G\mathbf{E}^{\mathbf{e}}_{\mathbf{0}} + K\,\mathrm{tr}(\mathbf{E}^{\mathbf{e}}) = \mathscr{C}[\mathbf{E}^{\mathbf{e}}] \tag{2.94}$$

and the effective granular stress, $\tilde{\boldsymbol{\sigma}}$, is given by,

$$\tilde{\boldsymbol{\sigma}} = J^{e-1}\mathbf{F}^{\mathbf{e}-\top}\mathbf{T}^{\mathbf{e}}\mathbf{F}^{\mathbf{e}\top} \tag{2.95}$$

2.3.14 Solid Phase Plastic Strain-Rate

The rules governing the solid phase plastic flow rate, $\mathbf{D}^{\mathbf{p}}$, are given by the inequality in Equation (2.83),

$$\tilde{\boldsymbol{\sigma}} : (\mathbf{F}^{\mathbf{e}}\mathbf{D}^{\mathbf{p}}\mathbf{F}^{\mathbf{e}-\mathbf{1}}) - (J^{e-1}\varphi_s\mathbf{1}) : \mathbf{D}^{\mathbf{p}} \geq 0$$

Substituting in the expression from Equation (2.95), we find,

$$J^{e-1}\mathbf{F}^{\mathbf{e}-\top}\mathbf{T}^{\mathbf{e}}\mathbf{F}^{\mathbf{e}\top} : (\mathbf{F}^{\mathbf{e}}\mathbf{D}^{\mathbf{p}}\mathbf{F}^{\mathbf{e}-\mathbf{1}}) - (J^{e-1}\varphi_s\mathbf{1}) : \mathbf{D}^{\mathbf{p}} \geq 0$$

which is equivalently,

$$(\mathbf{T^e} - \varphi_s \mathbf{1}) : \mathbf{D^p} \geq 0 \tag{2.96}$$

We assume that the granular skeleton in the mixture is *elastically stiff*, that is $\mathbf{U^e} \approx \mathbf{1}$, $J^e \approx 1$, and $\mathbf{E^e} \ll \mathbf{1}$. In this limit, $\|\mathbf{T^e}\| \gg \varphi_s$ and the thermodynamic inequality in Equation (2.96) reduces to the following expression for the *stiff plastic dissipation* of the granular skeleton,

$$\mathcal{D} \equiv \mathbf{T^e} : \mathbf{D^p} \geq 0 \tag{2.97}$$

It is convenient to introduce another measure of the plastic strain-rate, $\mathbf{\Gamma^p}$, which we define as follows,

$$\mathbf{\Gamma^p} = \mathbf{F^e D^p F^{e-1}} \tag{2.98}$$

This choice of flow rule has two useful consequences. First, Equation (2.72) gives the following expression for the solid phase strain-rate,

$$\mathbf{D_s} = \mathbf{D^e} + \mathbf{F^e D^p F^{e-1}}$$

which, by Equation (2.98), is equivalently,

$$\mathbf{D_s} = \mathbf{D^e} + \mathbf{\Gamma^p} \tag{2.99}$$

Second, Equation (2.98) lets the dissipation rule in Equation (2.97) be re-expressed as,

$$\mathcal{D} = \mathbf{F^{e-\top} T^e F^{e\top}} : \mathbf{\Gamma^p} \geq 0$$

which, in the limit that $J^e \approx 1$, is

$$\mathcal{D} = \tilde{\boldsymbol{\sigma}} : \mathbf{\Gamma^p} \geq 0 \tag{2.100}$$

Therefore, we satisfy the dissipation inequality in Equation (2.97) by defining the plastic strain-rate $\mathbf{D^p}$ implicitly via $\mathbf{\Gamma^p}$ subject to Equation (2.100).

2.3.15 Solid Phase Stress Evolution

The solid phase effective granular stress $\tilde{\boldsymbol{\sigma}}$ can be determined through time by evolving the elastic deformation gradient $\mathbf{F^e}$, calculating $\mathbf{E^e}$, and applying the definitions from Equations (2.94) and (2.95). However, it is more convenient to use the Jaumann objective rate of $\tilde{\boldsymbol{\sigma}}$ to evolve the solid phase granular effective stress directly. This rate is defined as,

$$\overset{\triangle}{\tilde{\boldsymbol{\sigma}}} \equiv \frac{D^s \tilde{\boldsymbol{\sigma}}}{Dt} - \mathbf{W_s}\tilde{\boldsymbol{\sigma}} + \tilde{\boldsymbol{\sigma}}\mathbf{W_s}$$

which in the *stiff* elastic limit can be shown to be well approximated by,

$$\overset{\triangle}{\tilde{\boldsymbol{\sigma}}} \approx \mathscr{C}[\mathbf{D^e}]$$

Combining these expressions, we define the material derivative of the effective granular stress in terms of the solid phase elastic strain-rate $\mathbf{D^e}$,

$$\frac{D^s\tilde{\boldsymbol{\sigma}}}{Dt} = 2G\mathbf{D_0^e} + K\,\mathrm{tr}(\mathbf{D^e})\mathbf{1} + \mathbf{W_s}\tilde{\boldsymbol{\sigma}} - \tilde{\boldsymbol{\sigma}}\mathbf{W_s} \tag{2.101}$$

With $\mathbf{D^e}$ defined in Equation (2.99) as,

$$\mathbf{D^e} = \mathbf{D_s} - \boldsymbol{\Gamma^p}$$

Simply stated, we evolve the effective granular stress according to how the solid phase is straining ($\mathbf{D_s}$) minus how much of that strain is plastic ($\boldsymbol{\Gamma^p}$).

2.3.16 Solid Phase Plastic Flow Rules

We let $\boldsymbol{\Gamma^p}$ have the following form,

$$\boldsymbol{\Gamma^p} = \frac{\dot{\bar{\gamma}}^p}{\sqrt{2}}\frac{\tilde{\boldsymbol{\sigma}}_\mathbf{0}}{\|\tilde{\boldsymbol{\sigma}}_\mathbf{0}\|} + \frac{1}{3}\left(\beta\dot{\bar{\gamma}}^p + \dot{\xi}_1 + \dot{\xi}_2\right)\mathbf{1} \tag{2.102}$$

where,

$$\tilde{\boldsymbol{\sigma}}_\mathbf{0} = \tilde{\boldsymbol{\sigma}} - \frac{1}{3}\,\mathrm{tr}(\tilde{\boldsymbol{\sigma}})\mathbf{1}$$

and the 'over-dot' operator $\dot{\langle\cdot\rangle}$ is equivalent to $\frac{D^s\langle\cdot\rangle}{Dt}$. $\dot{\bar{\gamma}}^p$, $\dot{\xi}_1$, and $\dot{\xi}_2$ are scalar measures of the solid phase equivalent plastic flow rates. $\bar{\gamma}^p$ is the accumulated *equivalent plastic shear* deformation. $\dot{\xi}_1$ is the rate of *plastic expansion* (Figure 2-7b), $\dot{\xi}_2$ is the negative rate of *plastic compaction* (Figure 2-7c), and $\beta\dot{\bar{\gamma}}^p$ is the rate of *plastic dilation* (Figure 2-7a).

The *dilation angle*, β, governs the rate of shear-dilation as in the simple critical state model from defined in Roux and Radjai [1998] and Roux and Radjai [2001] (and first proposed in Rudnicki and Rice [1975]). The functional form of β is the same as that given in Pailha and Pouliquen [2009] with a slight adjustment differentiating between dense and dilute behaviors,

$$\beta = \begin{cases} K_3(\phi - \phi_m) + K_4(\phi - \phi_{eq}) & \text{if} \quad \phi \geq \phi_m \\ K_4(\phi - \phi_{eq}) & \text{if} \quad \phi < \phi_m \end{cases} \tag{2.103}$$

where ϕ_m is the critical packing fraction for *sustained* granular contact, and ϕ_{eq} is the rate-dependent critical packing fraction given by,

$$\phi_{eq} = \frac{\phi_m}{1 + aI_m} \tag{2.104}$$

with a a material parameter. For $\phi > \phi_m$, we assume that the grains are *always* touching. Therefore, the dilation angle in this regime must have a rate-independent component, which we let be governed by the K_3 term. For $\phi \leq \phi_m$, the granular contacts are assumed to be collisional, and therefore only governed by the rate-dependent K_4 term. K_3 and K_4 are

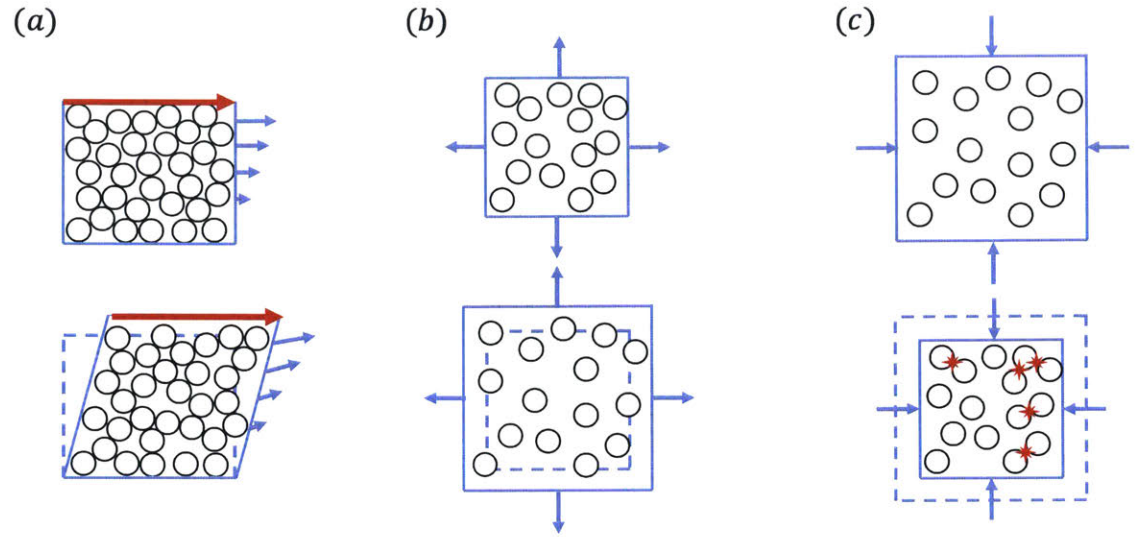

Figure 2-7: (a) In shear, the granular phase will obey critical state behavior and 'open-up'. This phenomena is called Reynolds' dilation and is captured by the rate of *plastic dilation*, $\beta\dot{\tilde{\gamma}}^p$. (b) In expansion, the granular phase will 'open' freely. This phenomena is stress-free and is captured by the negative rate of *plastic expansion*, $\dot{\xi}_1$. (c) In compaction, granular collisions will result in a macroscopic pressure. This phenomena is governed by the rate of *plastic compaction*, $\dot{\xi}_2$.

unit-less material parameters.

We define the f_1 yield surface and flow rule for the *equivalent plastic shear strain-rate*, $\dot{\tilde{\gamma}}^p$, as follows,

$$\begin{aligned} & f_1 = \bar{\tau} - s(\mu_p, \beta)\tilde{p} \\ & f_1 \leq 0 \\ & \dot{\tilde{\gamma}}^p = 0 \quad \text{if} \quad f_1 < 0 \quad \text{or} \quad \dot{f}_1 < 0 \\ \text{if} \quad & \dot{\tilde{\gamma}}^p > 0 \quad \text{then,} \quad f_1 = 0 \quad \text{and} \quad \dot{f}_1 = 0 \end{aligned} \tag{2.105}$$

with,

$$\bar{\tau} = \frac{\|\tilde{\boldsymbol{\sigma}}_{\mathbf{0}}\|}{\sqrt{2}}, \qquad \tilde{p} = -\frac{1}{3}\operatorname{tr}(\tilde{\boldsymbol{\sigma}}) \tag{2.106}$$

and,

$$s(\mu_p, \beta) = \max(\mu_p + \beta,\ 0) \tag{2.107}$$

The *internal friction coefficient*, μ_p, is given as a function of the *inertial number*, I, and the *viscous inertial number*, I_v. The specific form of this function follows from the definition of $\mu(I_m)$ given in Amarsid et al. [2017] with slight adjustments to account for the viscous inertial rheology found in Boyer et al. [2011]. These inertial numbers are defined as follows,

$$I = \dot{\tilde{\gamma}}^p d\sqrt{\frac{\rho_s}{\tilde{p}}}, \qquad I_v = \frac{\eta_0 \dot{\tilde{\gamma}}^p}{\tilde{p}} \tag{2.108}$$

$$I_m = \sqrt{I^2 + 2I_v} \tag{2.109}$$

We let $\mu_p = \hat{\mu}_p(I_v, I_m)$ with $\hat{\mu}_p(I_v, I_m)$ formulated to capture both the $\mu(I)$ dry granular rheology from Jop et al. [2006] and the $\mu(I_v)$ low stokes mixture rheology from Boyer et al. [2011], as will be shown in Section 3. The functional form of $\hat{\mu}_p$ is given as follows,

$$\hat{\mu}_p(I_v, I_m) = \mu_1 + \frac{\mu_2 - \mu_1}{1 + (b/I_m)} + \tfrac{5}{2}\phi\left(\frac{I_v}{aI_m}\right) \tag{2.110}$$

The f_2 yield surface and flow rule govern the rate of *plastic expansion*, $\dot{\xi}_1$, as follows,

$$\begin{aligned} & f_2 = -\tilde{p} \\ & f_2 \leq 0 \\ & \dot{\xi}_1 = 0 \quad \text{if} \quad f_2 < 0 \quad \text{or} \quad \dot{f}_2 < 0 \\ \text{if} \quad & \dot{\xi}_1 > 0 \quad \text{then,} \quad f_2 = 0 \quad \text{and} \quad \dot{f}_2 = 0 \end{aligned} \tag{2.111}$$

with $\tilde{p}$ given in Equation (2.106). This flow rule reflects our assumption that the granular phase is able to come apart freely, that is we constrain $\tilde{p} \geq 0$, which is common for non-cohesive granular materials.

The f_3 yield surface and flow rule govern the negative rate of *plastic compaction*, $\dot{\xi}_2$, as follows,

$$\begin{aligned} & f_3 = g(\phi)\tilde{p} - (a\phi)^2\left[(\dot{\bar{\gamma}}^p - K_5\dot{\xi}_2)^2 d^2 \rho_s + 2\eta_0(\dot{\bar{\gamma}}^p - K_5\dot{\xi}_2)\right] \\ & f_3 \leq 0 \\ & \dot{\xi}_2 = 0 \quad \text{if} \quad f_3 < 0 \quad \text{or} \quad \dot{f}_3 < 0 \\ \text{if} \quad & \dot{\xi}_2 < 0 \quad \text{then,} \quad f_3 = 0 \quad \text{and} \quad \dot{f}_3 = 0 \end{aligned} \tag{2.112}$$

with,

$$g(\phi) = \begin{cases} (\phi_m - \phi)^2 & \text{if} \quad \phi < \phi_m \\ 0 & \text{if} \quad \phi \geq \phi_m \end{cases} \tag{2.113}$$

The form of $g(\phi)$ is chosen such that when the material does not support sustained contacts, $\phi < \phi_m$, there is a rate-dependent upper bound on the admissible effective pressure $\tilde{p}$. However, in the compacted regime, $\phi \geq \phi_m$, any pressure is admissible, as the granular skeleton is physically capable of forming lasting force chains. The upper bound on the value of $\tilde{p}$ is determined by inverting the expression for ϕ_{eq} defined in Equation (2.104). The unitless K_5 coefficient defines the relative importance of the negative rate of compaction $\dot{\xi}_2$ in determining this upper bound, compared to the plastic shear rate $\dot{\bar{\gamma}}^p$.

2.3.17 Proof of Dissipation

With the definition of $\mathbf{\Gamma^p}$ in Equation (2.102), we return to the dissipation inequality defined in Equation (2.100),

$$\mathcal{D} = \tilde{\boldsymbol{\sigma}} : \mathbf{\Gamma^p} \geq 0$$

which is equivalently,

$$\mathcal{D} = \tilde{\boldsymbol{\sigma}} : \left(\frac{\dot{\bar{\gamma}}^p}{\sqrt{2}} \frac{\tilde{\boldsymbol{\sigma}}_{\mathbf{0}}}{\|\tilde{\boldsymbol{\sigma}}_{\mathbf{0}}\|} + \frac{1}{3}\big(\beta\dot{\bar{\gamma}}^p + \dot{\xi}_1 + \dot{\xi}_2\big)\mathbf{1} \right) \geq 0$$

or,

$$\mathcal{D} = \frac{\dot{\bar{\gamma}}^p}{\sqrt{2}} \frac{(\tilde{\boldsymbol{\sigma}}_{\mathbf{0}} : \tilde{\boldsymbol{\sigma}}_{\mathbf{0}})}{\|\tilde{\boldsymbol{\sigma}}_{\mathbf{0}}\|} + \frac{1}{3}\operatorname{tr}(\tilde{\boldsymbol{\sigma}})\big(\beta\dot{\bar{\gamma}}^p + \dot{\xi}_1 + \dot{\xi}_2\big) \geq 0$$

By the definition of $\bar{\tau}$ and $\tilde{p}$ in Equation (2.106), we therefore have,

$$\mathcal{D} = \bar{\tau}\dot{\bar{\gamma}}^p - \tilde{p}\big(\beta\dot{\bar{\gamma}}^p + \dot{\xi}_1 + \dot{\xi}_2\big) \geq 0$$

and,

$$\mathcal{D} = \dot{\bar{\gamma}}^p(\bar{\tau} - \beta\tilde{p}) - \dot{\xi}_1\tilde{p} - \dot{\xi}_2\tilde{p} \geq 0 \tag{2.114}$$

From the definition of the f_1 yield surface and flow rule in Equation (2.105), we have the following equality,

$$f_1\dot{\bar{\gamma}}^p = 0$$

which, by Equation (2.107), is equivalent to

$$\dot{\bar{\gamma}}^p\big(\bar{\tau} - \max(\mu_p + \beta,\ 0)\tilde{p}\big) = 0$$

or,

$$\dot{\bar{\gamma}}^p(\bar{\tau} - \beta\tilde{p}) = \dot{\bar{\gamma}}^p\tilde{p}\max(\mu_p,\ -\beta)$$

Since $\mu_p > 0$, $\dot{\bar{\gamma}}^p > 0$, and $\tilde{p} > 0$, this reduces to,

$$\dot{\bar{\gamma}}^p(\bar{\tau} - \beta\tilde{p}) \geq 0 \tag{2.115}$$

From the definition of the f_2 yield surface and flow rule in Equation (2.111), we have the following equality,

$$f_2\dot{\xi}_1 = 0$$

or,

$$-\dot{\xi}_1\tilde{p} = 0 \tag{2.116}$$

From the definition of the f_3 flow rule in Equation (2.112), we have $\dot{\xi}_2 \leq 0$ and therefore,

$$-\dot{\xi}_2\tilde{p} \geq 0 \tag{2.117}$$

By Equations (2.115), (2.116), (2.117), we have shown that each of the components of the dissipation inequality in Equation (2.114) are non-negative. Therefore, for the choice of plastic strain-rate $\boldsymbol{\Gamma}^{\mathbf{p}}$ in Section 2.3.14, we have proven that $\mathcal{D} \geq 0$.

Chapter 3

Verification of Model

In this section we verify that the model laid out in Section 2 has the correct limiting behavior. In particular we are interested in showing that under the appropriate conditions, the following rheologies are captured.

- $\tilde{\boldsymbol{\sigma}}$ Terzaghi's effective granular behavior.
- $\mu(I)$, $\phi(I)$ steady-state dry granular inertial rheology.
- $\mu(I_v)$, $\phi(I_v)$ steady-state viscous inertial rheology.
- $\eta_r(\phi)$ slurry/suspension effective viscosity.
- $\hat{F}(\phi, \mathrm{Re})$ Darcy's law drag behavior.

We have previously shown, in Section 2.2, that the Stokes' and Carman-Kozeny limits of the drag law, $\hat{F}(\phi, \mathrm{Re})$, are captured by Equations (2.37) and (2.38). For this reason, we will not repeat this analysis here. Instead, we will focus on the steady-state behavior of a uniform mixture under other applied flows.

3.1 Compaction

First, we consider the behavior of the mixture under an applied, distributed load $\boldsymbol{f}$ (as shown in Figure 3-1), such that $\boldsymbol{f}$ has units N/m^2. We let the velocities of the two phases be exactly zero,

$$\mathbf{v_s} = \mathbf{v_f} = \mathbf{0}$$

Under the applied load, we expect the entire volume of mixture to compress into a smaller volume such that the effective densities of both phases will *increase*,

$$\bar{\rho}_s > \bar{\rho}_{0s}$$

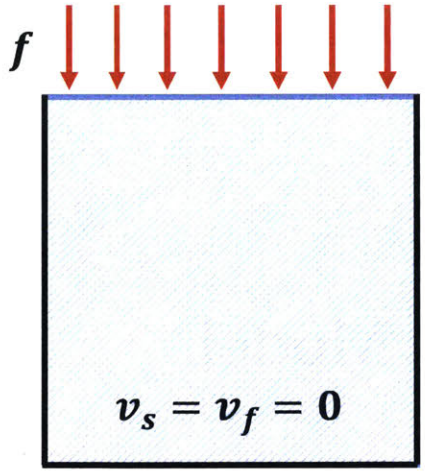

Figure 3-1: Pictorial representation of a volume of mixture being compacted by a distributed load $\boldsymbol{f}$. For the purposes of verifying the model described in Section 2, it is convenient to consider a flow where $\mathbf{v_s}$ and $\mathbf{v_f}$ are both zero.

where $\bar{\rho}_{0s}$ is the initial effective density of the stress-free mixture (before the load is applied). Clearly then, by Equation (2.2),

$$\phi > \phi_0, \quad \text{and} \quad n < n_0 \tag{3.1}$$

with ϕ_0 the initial packing fraction associated with the stress-free mixture and n the initial porosity. We also have,

$$\bar{\rho}_f > \bar{\rho}_{0f}$$

or,

$$n\rho_f > n_0\rho_{0f}$$

with ρ_{0f} the true fluid density in the stress-free mixture. By Equation (3.1),

$$\frac{\rho_f}{\rho_{0f}} > 1 \tag{3.2}$$

Since the fluid phase velocity is zero, we can use Equations (2.18) and (2.87) to determine the fluid phase stress, $\boldsymbol{\sigma_f}$,

$$\boldsymbol{\sigma_f} = -n\kappa \ln\left(\frac{\rho_f}{\rho_{0f}}\right)\mathbf{1} \tag{3.3}$$

Under the applied compaction, the granular effective stress will take on some value $\tilde{\boldsymbol{\sigma}}$ which (by Equation (2.17)) is given by,

$$\boldsymbol{\sigma_s} = \tilde{\boldsymbol{\sigma}}_0 - \tilde{p}\mathbf{1} - (1-n)\kappa \ln\left(\frac{\rho_f}{\rho_{0f}}\right)\mathbf{1} \tag{3.4}$$

Combined, Equations (3.3) and (3.4) give,

$$\boldsymbol{\sigma} = \tilde{\boldsymbol{\sigma}}_0 - \left(\tilde{p} + \kappa \ln\left(\frac{\rho_f}{\rho_{0f}}\right)\right)\mathbf{1} \tag{3.5}$$

with the total pressure response of the mixture being given by,

$$p = \tfrac{1}{3}\,\mathrm{tr}(\boldsymbol{\sigma}) = \tilde{p} + \kappa \ln\left(\frac{\rho_f}{\rho_{0f}}\right)$$

or,

$$\tilde{p} = p - \kappa \ln\left(\frac{\rho_f}{\rho_{0f}}\right) \tag{3.6}$$

with (by Equation (3.2)),

$$\kappa \ln\left(\frac{\rho_f}{\rho_{0f}}\right) > 0$$

Equation (3.6) for the effective granular pressure is the same as that reported by Terzaghi [1943], and we see that by Equations (2.105), (2.111), and (2.112), it is this same pressure (the Terzaghi effective pressure $\tilde{p}$) that governs the plastic behavior of the solid phase.

3.2 Simple Shear Flow

We now consider the behavior of the mixture under an applied shear flow (as in Figure 3-2) such that,

$$\mathbf{v_s} = \mathbf{v_f}$$

and,

$$\mathrm{grad}(\mathbf{v_s}) = \mathrm{grad}(\mathbf{v_f}) = \mathbf{L} = \begin{bmatrix} 0 & \dot{\gamma} & 0 \\ 0 & 0 & 0 \\ 0 & 0 & 0 \end{bmatrix}$$

where $\dot{\gamma}$ is the *steady shear-rate.*

3.2.1 Fluid Phase Behavior Under Simple Shear Flow

First, under an applied steady shear flow, we have

$$\mathrm{div}(\mathbf{v_s}) = \mathrm{tr}(\mathbf{L}) = 0$$

$$\mathrm{div}(\mathbf{v_f}) = \mathrm{tr}(\mathbf{L}) = 0$$

and,

$$\mathbf{D_f} = \tfrac{1}{2}(\mathbf{L} + \mathbf{L}^\top) = \begin{bmatrix} 0 & \frac{\dot{\gamma}}{2} & 0 \\ \frac{\dot{\gamma}}{2} & 0 & 0 \\ 0 & 0 & 0 \end{bmatrix}$$

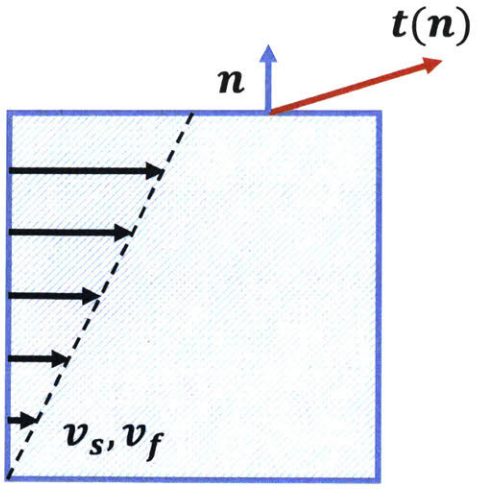

Figure 3-2: Pictorial representation of a simple shear flow within a volume of mixture. For the purposes of verifying the model described in Section 2, it is convenient to consider a flow where $\mathbf{v_s}$ and $\mathbf{v_f}$ are co-moving with a uniform velocity gradient and uniform mixture properties. $\mathbf{t(n)}$ in the image represents the surface traction associated with the normal vector to the surface $\mathbf{n}$.

Since mixture is assumed to be uniform and n is constant, the rate of change of density in Equation (2.10) reduces to,

$$\frac{D^f \rho_f}{Dt} = (1-n)\,\mathrm{div}(\mathbf{v_s}) + n\,\mathrm{div}(\mathbf{v_f}) = 0$$

By Equation (2.87) the expression above has the intuitive consequence that, under uniform shear, the fluid phase pore pressure remains constant,

$$\frac{D^f p_f}{Dt} = 0, \quad p_f = p_{eq} \tag{3.7}$$

with p_{eq} some equilibrium pressure. The fluid phase shear stress, $\boldsymbol{\tau_f}$, is given by Equation (2.88) as follows,

$$\boldsymbol{\tau_f} = 2\eta_0(1+\tfrac{5}{2}\phi)\begin{bmatrix} 0 & \frac{\dot{\gamma}}{2} & 0 \\ \frac{\dot{\gamma}}{2} & 0 & 0 \\ 0 & 0 & 0 \end{bmatrix} \tag{3.8}$$

3.2.2 Solid Phase Behavior Under Simple Shear Flow

By Equation (2.99), under an applied steady shear flow, we have,

$$\mathbf{D_s} = \mathbf{D^e} + \mathbf{\Gamma^p}$$

with,

$$\mathbf{D_s} = \tfrac{1}{2}(\mathbf{L} + \mathbf{L}^\top) = \begin{bmatrix} 0 & \frac{\dot\gamma}{2} & 0 \\ \frac{\dot\gamma}{2} & 0 & 0 \\ 0 & 0 & 0 \end{bmatrix}$$

and,

$$\mathbf{W} = \tfrac{1}{2}(\mathbf{L} - \mathbf{L}^\top) = \begin{bmatrix} 0 & \frac{\dot\gamma}{2} & 0 \\ -\frac{\dot\gamma}{2} & 0 & 0 \\ 0 & 0 & 0 \end{bmatrix}$$

In the solid phase there are two regimes of interest, the compacted regime with $\phi \geq \phi_m$ and the non-compacted regime with $\phi < \phi_m$. In the compacted regime, the sustained granular contacts result in non-steady behavior (the positivity of the dilatancy angle β from Equation (2.103) results in continuous growth of the pressure $\tilde{p}$). For this reason, we will be more interested in the behavior of the non-compacted regime, where granular stresses result from intermittent granular contacts and interactions via the fluid medium. Assuming the solid phase begins in a stress-free state, the evolution law for the solid phase effective stress given in Equation (2.101) suggests the following form for $\tilde{\boldsymbol{\sigma}}$ in the fully developed shear flow,

$$\tilde{\boldsymbol{\sigma}} = \begin{bmatrix} \epsilon & t & 0 \\ t & -\epsilon & 0 \\ 0 & 0 & 0 \end{bmatrix} + \begin{bmatrix} \tilde{p} & 0 & 0 \\ 0 & \tilde{p} & 0 \\ 0 & 0 & \tilde{p} \end{bmatrix} \tag{3.9}$$

where ϵ and t have units of stress and $\epsilon < t$. If we let, $\tilde{p}$ be given by,

$$\tilde{p} = \left(\frac{a\phi}{\phi_m - \phi}\right)^2 \left[(\dot{\bar{\gamma}}^p)^2 d^2 \rho_s + 2\eta_0 \dot{\bar{\gamma}}^p\right] - p_\epsilon \tag{3.10}$$

with,

$$0 < p_\epsilon \ll 1$$

By Equations (2.111) and (2.112), we have,

$$f_2 < 0 \implies \dot{\xi}_1 = 0, \qquad \text{and} \qquad f_3 < 0 \implies \dot{\xi}_2 = 0$$

Further, Equation (3.10) gives,

$$\left(\frac{\phi_m - \phi}{a\phi}\right)^2 \approx \left[\frac{(\dot{\bar{\gamma}}^p)^2 d^2 \rho_s}{\tilde{p}} + 2\frac{\eta_0 \dot{\bar{\gamma}}^p}{\tilde{p}}\right]$$

or, from the definition of the inertial numbers in Equation (2.108) and the mixed inertial number in Equation (2.109),

$$\frac{\phi_m - \phi}{a\phi} \approx I_m$$

and,

$$\phi \approx \frac{\phi_m}{1 - I_m} \tag{3.11}$$

Since this expression is identical to the value of ϕ_{eq} given in Equation (2.104), Equation (2.103) gives,

$$\beta = 0$$

which therefore yields, by Equation (2.102),

$$\mathrm{tr}(\mathbf{\Gamma^p}) = 0$$

and, in combination with Equation (3.9),

$$\mathbf{\Gamma^p} = \frac{\dot{\bar{\gamma}}^p}{\sqrt{2}} \frac{\tilde{\boldsymbol{\sigma}}_\mathbf{0}}{\|\tilde{\boldsymbol{\sigma}}_\mathbf{0}\|} = \frac{\dot{\bar{\gamma}}^p}{2\sqrt{t^2 + \epsilon^2}} \begin{bmatrix} \epsilon & t & 0 \\ t & -\epsilon & 0 \\ 0 & 0 & 0 \end{bmatrix}$$

Intuitively, in steady shearing flow, the *equivalent plastic shear rate* $\dot{\bar{\gamma}}^p$ will be non-zero and very nearly equivalent to total *steady shear rate* $\dot{\gamma}$. Therefore, by Equation (2.105), $f_1 = 0$. And, if we let $\dot{\bar{\gamma}}^p$ be given as follows,

$$\dot{\bar{\gamma}}^p = \frac{\dot{\gamma} t}{\sqrt{t^2 + \epsilon^2}}$$

then,

$$\mathbf{\Gamma^p} = \frac{\dot{\gamma} t}{2(t^2 + \epsilon^2)} \begin{bmatrix} \epsilon & t & 0 \\ t & -\epsilon & 0 \\ 0 & 0 & 0 \end{bmatrix}$$

We can now solve for the evolution of the granular effective stress according to Equation (2.101),

$$\frac{D^s \tilde{\boldsymbol{\sigma}}}{Dt} = 2G(\mathbf{D_0} - \mathbf{\Gamma_0^p}) + K\,\mathrm{tr}(\mathbf{D})\mathbf{1} - \mathrm{tr}(\mathbf{\Gamma^p})\mathbf{1} + \mathbf{W}\tilde{\boldsymbol{\sigma}} - \tilde{\boldsymbol{\sigma}}\mathbf{W}$$

which becomes,

$$\frac{D^s \tilde{\boldsymbol{\sigma}}}{Dt} = G\frac{\dot{\gamma}\epsilon}{(t^2 + \epsilon^2)} \begin{bmatrix} -t & \epsilon & 0 \\ \epsilon & t & 0 \\ 0 & 0 & 0 \end{bmatrix} + \dot{\gamma} \begin{bmatrix} t & -\epsilon & 0 \\ -\epsilon & -t & 0 \\ 0 & 0 & 0 \end{bmatrix}$$

Clearly then, if we let $G\epsilon - \epsilon^2 = t^2$ and let the material be elastically stiff, such that $G \gg t$, we find,

$$\frac{D^s \tilde{\boldsymbol{\sigma}}}{Dt} = \mathbf{0}$$

with,

$$\epsilon \approx 0, \quad \text{and} \quad \dot{\bar{\gamma}}^p \approx \dot{\gamma}$$

Therefore, the solid phase effective stress is well approximated by,

$$\tilde{\boldsymbol{\sigma}} \approx \begin{bmatrix} 0 & t & 0 \\ t & 0 & 0 \\ 0 & 0 & 0 \end{bmatrix} + \begin{bmatrix} \tilde{p} & 0 & 0 \\ 0 & \tilde{p} & 0 \\ 0 & 0 & \tilde{p} \end{bmatrix}$$

and, by $f_1 = 0$ in Equation (2.105),

$$\tilde{\boldsymbol{\sigma}} \approx \begin{bmatrix} \tilde{p} & \mu_p \tilde{p} & 0 \\ \mu_p \tilde{p} & \tilde{p} & 0 \\ 0 & 0 & \tilde{p} \end{bmatrix} \tag{3.12}$$

3.2.3 Combined Behavior Under Simple Shear Flow

Given the steady-state phase stresses defined in Equations (3.7), (3.8), and (3.12), the total mixture stress as defined in Equation (2.5) is given by,

$$\boldsymbol{\sigma} = 2\eta_0(1 + \tfrac{5}{2}\phi) \begin{bmatrix} 0 & \frac{\dot{\gamma}}{2} & 0 \\ \frac{\dot{\gamma}}{2} & 0 & 0 \\ 0 & 0 & 0 \end{bmatrix} + \begin{bmatrix} 0 & \mu_p \tilde{p} & 0 \\ \mu_p \tilde{p} & 0 & 0 \\ 0 & 0 & 0 \end{bmatrix} + (p_{eq} + \tilde{p})\mathbf{1} \tag{3.13}$$

According to the Equation (2.4), we let the surface traction vector be given by,

$$\mathbf{t}(\mathbf{n}) = \boldsymbol{\sigma}\mathbf{n}$$

in particular, we are interested in the measured behavior perpendicular to the flow gradient, that is,

$$\mathbf{n} = \begin{bmatrix} 0 \\ 1 \\ 0 \end{bmatrix}$$

and the traction vector for this normal,

$$\mathbf{t}(\mathbf{n}) = \begin{bmatrix} t_t \\ t_n \\ 0 \end{bmatrix} = \begin{bmatrix} \eta_0 \dot{\gamma}\left(1 + \frac{5}{2}\phi\right) + \mu_p \tilde{p} \\ p_{eq} + \tilde{p} \\ 0 \end{bmatrix} \tag{3.14}$$

where t_t is the shear component of the traction vector and t_n is the normal component of the traction vector.

3.2.4 Dry Granular Rheology

In steady simple shear flow, dry granular materials have been shown to obey the $\mu(I)$ and $\phi(I)$ rheology. As given in Jop et al. [2006] and Da Cruz et al. [2005],

$$\mu(I) = \mu_1 + \frac{\mu_2 - \mu_1}{1 + (I_0/I)}, \qquad \text{and} \qquad \phi(I) = \phi_m - cI$$

with c some material constant and $\mu(I)$ is the ratio between the measured shear traction component t_t and the measured normal traction component t_n for the entire mixture. This behavior is captured by our model in the limit that $\eta_0 \to 0$ and $p_{eq} \to 0$. By our definition of the inertial numbers in Equations (2.108) and (2.109),

$$\eta_0 \to 0 \implies I_v \to 0 \implies I_m \to I$$

Equation (3.11) gives the relation for the steady packing fraction under an applied shear flow as,

$$\phi = \frac{\phi_m}{1 + aI_m}$$

Expanding around $I_m \approx I \approx 0$, we find

$$\phi = \phi_m - a\phi_m I + O(I^2)$$

which is a reasonable approximation of the $\phi(I)$ rheology if $a = (c/\phi_m)$. We also note that with t_t and t_n given as in Equation (3.14), and in the limit of $\eta_0 \to 0$, the ratio of t_t/t_n is given as,

$$\eta_0 \to 0, \quad p_{eq} \to 0 \quad \implies \quad \frac{t_t}{t_n} = \mu_p$$

where μ_p is defined in Equation (2.110), which for $I_m \to I$ and $I_v \to 0$ becomes,

$$\mu_p = \mu_1 + \frac{\mu_2 - \mu_1}{1 + (b/I)}$$

This clearly matches the $\mu(I)$ rheology for $b = I_0$.

3.2.5 Viscous Granular Rheology

Boyer et al. [2011] experimentally investigates the steady-state rheology of mixtures undergoing steady quasi-2D shear flow at low Stokes numbers with $p_{eq} = 0$. The Stokes number of interest in this context is defined in Amarsid et al. [2017] as,

$$\mathrm{St} = \frac{\rho_s d^2 \dot{\gamma}}{\eta_0} = \frac{I^2}{I_v} \tag{3.15}$$

Conceptually, the Stokes number of the flow relates the relative importance of the two basic

inertial numbers, I and I_v. In the limit that the Stokes number goes to zero, we find that the mixed inertial number I_m depends only on the viscous inertial number,

$$\mathrm{St} \to 0 \quad \Longrightarrow \quad I_m \to \sqrt{2I_v}$$

Through dimensional analysis and fitting lines to experimental data, Boyer et al. [2011] define the $\mu(I_v)$ and $\phi(I_v)$ rheologies as follows,

$$\mu(I_v) = \mu_1 + \frac{\mu_2 - \mu_1}{1 + (I_0/I_v)} + I_v + \tfrac{5}{2}\phi_m\sqrt{I_v}$$

and,

$$\phi(I_v) = \frac{\phi_m}{1 + \sqrt{I_v}}$$

Again, in the steady flow predicted by our model, Equation (3.11) gives,

$$\phi = \frac{\phi_m}{1 + aI_m}$$

which, with $I_m \approx \sqrt{2I_v}$, becomes,

$$\phi = \frac{\phi_m}{1 + a\sqrt{2I_v}}$$

This is clearly identical to the relation given by $\phi(I_v)$ when $a = \frac{1}{\sqrt{2}}$. For the $\mu(I_v)$ rheology, it is important to note that Boyer et al. [2011] measures $\mu = (t_t/t_n)$. In the viscous limit, this includes both granular and fluid stresses.

$$\mu = \frac{t_t}{t_n} = \frac{\eta_0\dot{\gamma}\left(1 + \frac{5}{2}\phi\right) + \mu_p\tilde{p}}{\tilde{p}}$$

or equivalently,

$$\mu = I_v\left(1 + \tfrac{5}{2}\phi\right) + \mu_p$$

Substituting in the steady state packing fraction from Equation (3.11) and the expression for the friction coefficient from Equation (2.110) we find,

$$\mu = \mu_1 + \frac{\mu_2 - \mu_1}{1 + (b/\sqrt{2I_v})} + I_v + \tfrac{5}{2}\phi_m\sqrt{\frac{I_v}{2a^2}} \tag{3.16}$$

Exact recovery of the $\mu(I_v)$ rheology is not possible with our model; however, as shown in Figure 3-3, we can fit our model for $\mu(I_v, I_m)$ to the the data directly. Strong agreement is found between our model fit, the model fit in Boyer et al. [2011], and the data collected in that work. The fit parameters for the plot in Figure 3-3 are given in Table 3.1

Table 3.1: Fit Parameters for Figure 3-3

Parameter	$\mu(I_v)$	$\mu(I_v, I_m)$
μ_1	0.32	0.2764
μ_2	0.7	0.8797
I_0	0.005	-
ϕ_m	0.585	0.585
a	-	0.7071
b	-	0.1931

3.2.6 Suspension Effective Viscosity

Significant work has been done on understanding the behavior of co-moving suspensions of granular material in fluids. We are particularly interested in the viscous thickening of suspensions due to the solid phase volume fraction as reviewed and summarized in Stickel and Powell [2005] with η_r, the *relative viscosity*, given as,

$$\eta_r = \frac{t_t}{\eta_0 \dot{\gamma}} = f\left(\frac{\phi}{\phi_m}\right)$$

which has two important limits. In the dense limit ($\phi \to \phi_m$), the viscosity of the suspension approaches infinity, that is,

$$\lim_{\phi \to \phi_m} \eta_r = \infty$$

In the dilute limit ($\phi \to 0$), the viscosity of the mixture should obey,

$$\lim_{\phi \to 0} \frac{\eta_r - 1}{\phi} = [\eta]$$

with $[\eta] = \frac{5}{2}$ for hard spheres (Stickel and Powell [2005]).

As in Section 3.2.5, we are concerned with the behavior of our mixture model in the low stokes limit such that,

$$I_m \approx \sqrt{2I_v}$$

Therefore,

$$\eta_r = \frac{t_t}{\eta_0 \dot{\gamma}} = \frac{\eta_0 \dot{\gamma}\left(1 + \frac{5}{2}\phi\right) + \mu_p \tilde{p}}{\eta_0 \dot{\gamma}}$$

or,

$$\eta_r = 1 + \frac{5}{2}\phi + \frac{\mu_p}{I_v}$$

Recalling the relationship found for the steady state packing fraction in Equation (3.11)

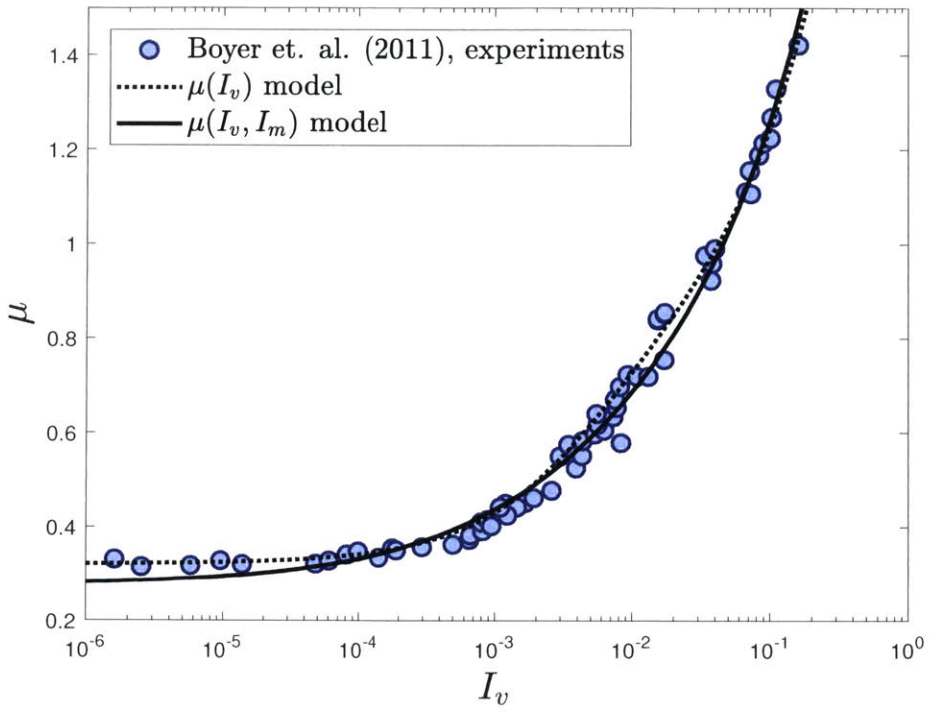

Figure 3-3: Plot of the ratio between the shear traction and normal traction (μ) against the inertial number I_v. Data collected by Boyer et al. [2011] is shown as the shaded blue circles. The $\mu(I_v)$ rheology from that work is shown in the dashed line. The combined mixture model presented in this work is shown in the solid line.

and the functional form of μ_p given in Equation (2.110), we find,

$$I_v = \frac{1}{2}\left(\frac{a\phi}{\phi_m - \phi}\right)^{-2}$$

and,

$$\eta_r(\phi) = 1 + \frac{5}{2}\phi\left(\frac{\phi_m}{\phi_m - \phi}\right) + 2\left(\frac{a\phi}{\phi_m - \phi}\right)^2\left(\mu_1 + \frac{\mu_2 - \mu_1}{1 + ab\phi/(\phi_m - \phi)}\right) \tag{3.17}$$

It can be shown that this relation achieves both limiting behaviors required of effective viscosity models. For comparison, we look at three empirical relations for the effective viscosity of fluid-sediment mixtures reported in Stickel and Powell [2005]. The first is the classic result from Einstein [1906] which gives the correct dilute suspension behavior,

$$\eta_r = 1 + \tfrac{5}{2}\phi + O(\phi^2) \tag{3.18}$$

Another relationship given by Eilers (Eilers [1949] and Ferrini et al. [1979]) predicts the

correct behavior in both the dense and dilute phases,

$$\eta_r = \left(1 + \frac{\frac{5}{4}\phi}{1 - \phi/\phi_m}\right)^2 \tag{3.19}$$

A third relationship, given by Krieger and Dougherty [1959], predicts similar behavior,

$$\eta_r = \left(1 - \frac{\phi}{\phi_m}\right)^{-\frac{5}{2}\phi_m} \tag{3.20}$$

In Figure 3-4, we show how each of these empirical models (in addition to the model proposed here, $\eta_r(\phi)$) compares to the experimental measurements reported in Chang and Powell [1994] (from Chong et al. [1971], Poslinski et al. [1988], Storms et al. [1990], Shapiro and Probstein [1992], Chang and Powell [1993], and Chang and Powell [1994]). By noting the similarity of the materials used by Chang and Powell [1994] (PS and PMMA), to that used in Boyer et al. [2011], we simply reuse the coefficients determined in Section 3.2.5 and as given in Table 3.1 for plotting Equation (3.17) in Figure 3-4. The collapse of the data onto the curves is good for low values of ϕ/ϕ_m; however the predictions seem to deviate at higher values. This may be due to the significant difference in ϕ_m reported in Chang and Powell [1994] ($\phi_m \approx 0.7$) to the value used in this work ($\phi_m = 0.585$).

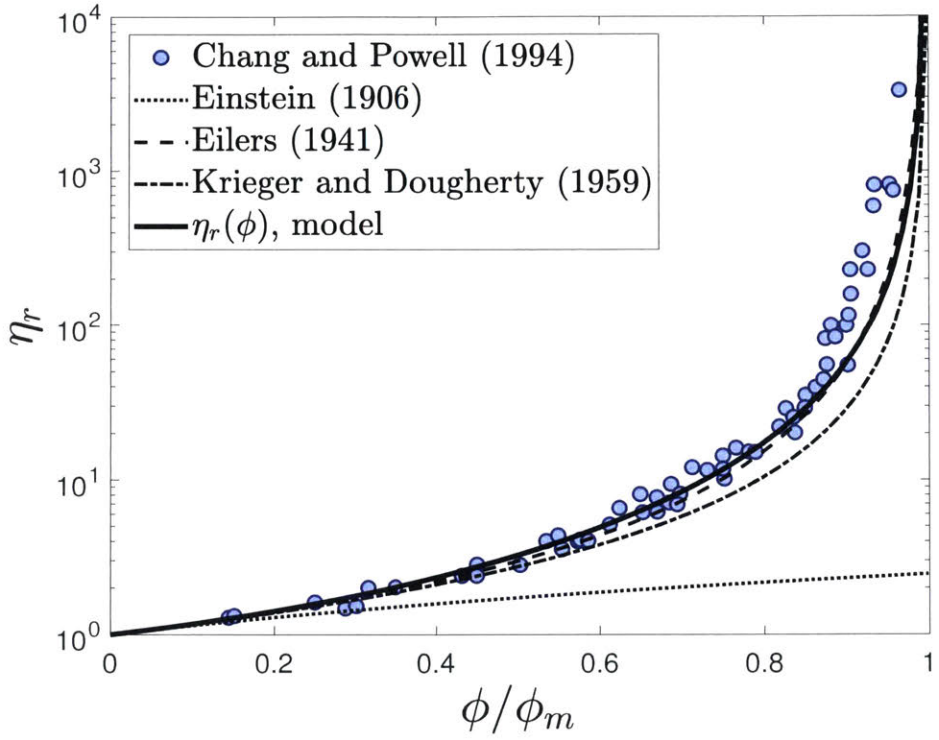

Figure 3-4: Plot of the effective viscosity η_r versus the relative packing fraction ϕ/ϕ_m. The model given by Einstein [1906] (Equation (3.18)) is shown in the small dotted line. The model given by Eilers [1949] (Equation (3.19)) is shown in the dashed/dotted line. The model given by Krieger and Dougherty [1959] (Equation (3.20)) is shown by the dashed line. The model given in this work by Equation (3.17) is shown by the solid line. The circles represent the experimental results reported in Chang and Powell [1994] (from Chong et al. [1971], Poslinski et al. [1988], Storms et al. [1990], Shapiro and Probstein [1992], Chang and Powell [1993], and Chang and Powell [1994])

Chapter 4

Numerical Implementation

In this section we describe the numerical implementation of the theory described in Section 2. In particular, we are interested in time-accurate simulations of fluid-sediment mixtures undergoing arbitrarily large deformations. To do this, we use a material point method framework capable of simultaneously solving all of the governing equations shown in Table 4.1 (including solving the equations for plastic flow given in Table 4.2). The material point method framework we present is a derivative of that shown in Dunatunga and Kamrin [2015] and borrows heavily from methods described in Abe et al. [2013] and Bandara and Soga [2015].

Figure 4-1 shows the basic method we implement. First, the mixture problem is defined and the material configurations are given (Figure 4-1(1)). The two phases are then separated into the continuum bodies described in Figure 2-2 (Figure 4-1(2)). These continuum bodies are discretized into two sets of Largrangian material point tracers. These tracers carry the full description of the continuum bodies (stress, strain, density, velocity) and serve to advect material properties through space (Figure 4-1(3)). These two sets of tracers are then placed into a simulation domain which is discretized into a background grid. The background grid is where the equation of motion are solved in the weak form (Figure 4-1(4)).

4.1 Material Point Method Discretization

The material point method, as first derived by Sulsky et al. [1994], is a numerical scheme for solving dynamic problems in solid mechanics where materials undergo large deformations. The basic algorithm defined in Sulsky et al. [1994] and generalized by Bardenhagen and Kober [2004] involves discretizing material fields (such as density and stress) on a set of material point tracers and solving the equations of motion on a background grid.

In Abe et al. [2013] and Bandara and Soga [2015], the material point method is extended to solve the equations of mixtures defined in Jackson [2000] (here in Equations (2.21) and (2.22)). Our material point method algorithm is not significantly different (as far as we can tell) from that given in prior works; however, we will briefly review our method here prior to covering the results of our implementation.

Table 4.1: Summary of Governing Equations

Rule	Expression	Number
Solid Phase Mass Conservation	$\frac{D^s \bar{\rho}_s}{Dt} + \bar{\rho}_s \operatorname{div} \mathbf{v_s} = 0$	(2.7)
Fluid Phase Mass Conservation	$\frac{D^f \bar{\rho}_f}{Dt} + \bar{\rho}_f \operatorname{div} \mathbf{v_f} = 0$	(2.9)
Fluid Phase True Density	$\frac{n}{\rho_f}\frac{D^f \rho_f}{Dt} = -\operatorname{div}\left((1-n)\mathbf{v_s} + n\mathbf{v_f}\right)$	(2.10)
Solid Phase Momentum Balance	$\bar{\rho}_s \frac{D^s \mathbf{v_s}}{Dt} = \bar{\rho}_s \mathbf{g} - \mathbf{f_d} + \operatorname{div}(\tilde{\boldsymbol{\sigma}}) - (1-n)\operatorname{grad}(p_f)$	(2.21)
Fluid Phase Momentum Balance	$\bar{\rho}_f \frac{D^f \mathbf{v_f}}{Dt} = \bar{\rho}_f \mathbf{g} + \mathbf{f_d} + \operatorname{div}(\boldsymbol{\tau_f}) - n\operatorname{grad}(p_f)$	(2.22)
Darcy's Drag Law	$\mathbf{f_d} = \frac{18\phi(1-\phi)\eta_0}{d^2}\,\hat{F}(\phi, \mathrm{Re})\,(\mathbf{v_s} - \mathbf{v_f})$	(2.39)
	$\hat{F}(\phi, \mathrm{Re}) = \hat{F}(\phi, 0) + f(\phi, \mathrm{Re})$	(2.38)
	$\hat{F}(\phi, 0) = \frac{10\phi}{(1-\phi)^2} + (1-\phi)^2(1 + 1.5\sqrt{\phi})$	(2.37)
Fluid Phase Pore Pressure	$p_f = \kappa \ln\left(\frac{\rho_f}{\rho_{0f}}\right)$	(2.87)
Fluid Phase Shear Stress	$\boldsymbol{\tau_f} = 2\eta_0\left(1 + \frac{5}{2}\phi\right)\mathbf{D_{0f}}$	(2.88)
Solid Phase Effective Stress	$\frac{D^s \tilde{\boldsymbol{\sigma}}}{Dt} = 2G\mathbf{D_0^e} + K\operatorname{tr}(\mathbf{D^e})\mathbf{1} + \mathbf{W_s}\tilde{\boldsymbol{\sigma}} - \tilde{\boldsymbol{\sigma}}\mathbf{W_s}$	(2.101)
	$\mathbf{D^e} = \mathbf{D_s} - \boldsymbol{\Gamma^p}$	(2.99)
	$\boldsymbol{\Gamma^p} = \frac{\dot{\bar{\gamma}}^p}{\sqrt{2}}\frac{\tilde{\boldsymbol{\sigma}}_\mathbf{0}}{\|\tilde{\boldsymbol{\sigma}}_\mathbf{0}\|} + \frac{1}{3}\left(\beta\dot{\bar{\gamma}}^p + \dot{\xi}_1 + \dot{\xi}_2\right)\mathbf{1}$	(2.102)

Table 4.2: Summary of Plastic Flow Equations

Rule	**Expression**	**Number**
Solid Phase Plastic Flow Rate	$\mathbf{\Gamma^p} = \frac{\dot{\bar{\gamma}}^p}{\sqrt{2}} \frac{\tilde{\boldsymbol{\sigma}}_\mathbf{0}}{\|\tilde{\boldsymbol{\sigma}}_\mathbf{0}\|} + \frac{1}{3}\left(\beta \dot{\bar{\gamma}}^p + \dot{\xi}_1 + \dot{\xi}_2\right)\mathbf{1}$	(2.102)
Dilation Angle	$\beta = \begin{cases} K_3(\phi - \phi_m) + K_4(\phi - \phi_{eq}) & \text{if} \quad \phi \geq \phi_m \\ K_4(\phi - \phi_{eq}) & \text{if} \quad \phi < \phi_m \end{cases}$	(2.103)
Critical State Packing Fraction	$\phi_{eq} = \frac{\phi_m}{1 + aI_m}$	(2.104)
Internal Friction Coefficient	$\mu_p = \mu_1 + \frac{\mu_2 - \mu_1}{1 + (b/I_m)} + \frac{5}{2}\phi\left(\frac{I_v}{aI_m}\right)$	(2.110)
f_1 Yield Condition	$f_1 = \bar{\tau} - \max\left((\mu_p + \beta)\tilde{p},\ 0\right)$ $f_1 \leq 0, \qquad \dot{\bar{\gamma}}^p \geq 0, \qquad f_1 \dot{\bar{\gamma}}^p = 0$	(2.105)
f_2 Yield Condition	$f_2 = -\tilde{p}$ $f_2 \leq 0, \qquad \dot{\xi}_1 \geq 0, \qquad f_2 \dot{\xi}_1 = 0$	(2.111)
f_3 Yield Condition	$f_3 = \tilde{p} - g(\phi)\left[(\dot{\bar{\gamma}}^p - K_5\dot{\xi}_2)^2 d^2 \rho_s + 2\eta_0(\dot{\bar{\gamma}}^p - K_5\dot{\xi}_2)\right]$ $f_3 \leq 0, \qquad \dot{\xi}_2 \leq 0, \qquad f_3 \dot{\xi}_2 = 0$	(2.112)
	$g(\phi) = \begin{cases} \left(\frac{a\phi}{\phi_m - \phi}\right) & \text{if} \quad \phi < \phi_m \\ \infty & \text{if} \quad \phi \geq \phi_m \end{cases}$	(2.113)

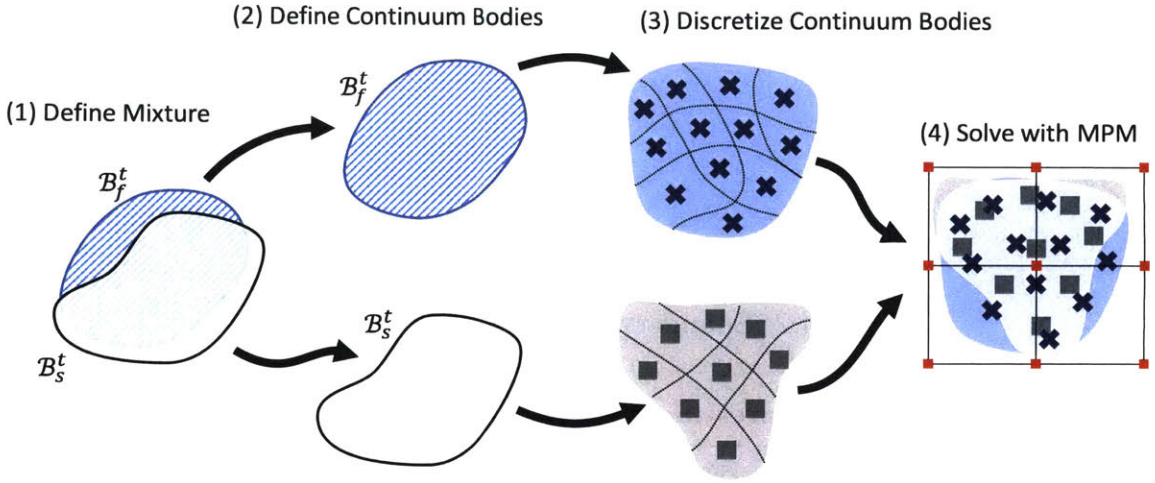

Figure 4-1: The basic method of solving mixture problems using the material point method. (1) Define the mixture and initial configuration including densities, porosities, stresses. (2) Define the solid and fluid phase continuum bodies. (3) Break the continuum bodies into piecewise-defined blocks of material represented by discrete material points. (4) Solve the equations of motion for the mixture on a background grid according to the material point method algorithm described in Section 4.2

4.1.1 Definition of Material Point Tracers

As shown in Figure 4-1(3), the two continuum bodies defined in Figure 2-2 by $\mathcal{B}_s^t$ and $\mathcal{B}_f^t$ are discretized into material blocks represented by discrete material points. We therefore let the continuum representation of the bodies be given by,

$$\begin{aligned} \sum_{p=1}^{N_s} U_{sp}(\mathbf{x}) &= \begin{cases} 1 & \mathbf{x} \in \mathcal{B}_s^t \\ 0 & \text{else} \end{cases} \\ \sum_{p=1}^{N_f} U_{fp}(\mathbf{x}) &= \begin{cases} 1 & \mathbf{x} \in \mathcal{B}_f^t \\ 0 & \text{else} \end{cases} \end{aligned} \tag{4.1}$$

where $\mathbf{x}$ is the position vector in the domain Ω, $U_{sp}(\mathbf{x})$ and $U_{fp}(\mathbf{x})$ are the pth material point characteristic functions (as in Bardenhagen and Kober [2004]) that are *co-moving with the material*, and N_s and N_f are the number of solid and fluid material point tracers. Intuitively, the total sum of the characteristic functions defines a spatial field which is equal to 1 within the body and 0 outside.

Clearly then, we can construct the solid continuum fields using the U_{sp} functions as

follows,

$$\begin{aligned}\bar{\rho}_s(\mathbf{x}) &= \sum_{p=1}^{N_s} \bar{\rho}_{sp} U_{sp}(\mathbf{x}) \\ \tilde{\boldsymbol{\sigma}}(\mathbf{x}) &= \sum_{p=1}^{N_s} \tilde{\boldsymbol{\sigma}}_p U_{sp}(\mathbf{x})\end{aligned} \tag{4.2}$$

where ψ_p represents a constant (scalar, vector, or tensor) associated with the field $\psi(\mathbf{x})$ and the pth material point. The fluid continuum fields are constructed as follows,

$$\begin{aligned}\bar{\rho}_f(\mathbf{x}) &= \sum_{p=1}^{N_f} \bar{\rho}_{fp} U_{fp}(\mathbf{x}) \\ \rho_f(\mathbf{x}) &= \sum_{p=1}^{N_f} \rho_{fp} U_{fp}(\mathbf{x}) \\ \boldsymbol{\tau_f}(\mathbf{x}) &= \sum_{p=1}^{N_f} \boldsymbol{\tau_f}_p U_{fp}(\mathbf{x}) \\ p_f(\mathbf{x}) &= \sum_{p=1}^{N_f} p_{fp} U_{fp}(\mathbf{x})\end{aligned} \tag{4.3}$$

We also introduce a measure of material point weight, v_{sp} and v_{fp},

$$\begin{aligned}v_{sp} &= \int_\Omega U_{sp}(\mathbf{x}) dv \\ v_{fp} &= \int_\Omega U_{fp}(\mathbf{x}) dv\end{aligned} \tag{4.4}$$

In addition to the fields above, we let each material point have a centroid (center of mass) which maps to a location $\mathbf{x_s}_p$ for the pth solid material point and $\mathbf{x_f}_p$ for the pth fluid material point (see Figure 4-2). This centroid moves through the domain and has an associated momentum $m_{sp}\mathbf{v_s}_p$ or $m_{vp}\mathbf{v_f}_p$ respectively with,

$$\begin{aligned}m_{sp} &= v_{sp}\bar{\rho}_{sp}, \qquad & \frac{d}{dt}(m_{sp}) &= 0 \\ m_{fp} &= v_{fp}\bar{\rho}_{fp}, \qquad & \frac{d}{dt}(m_{fp}) &= 0\end{aligned} \tag{4.5}$$

For our formulation, we also require that the material characteristic functions obey the following rule,

$$\begin{aligned}U_{sp}(\mathbf{x_s}_q) &= \delta_{pq} \quad \forall p, q \in [1, N_s] \\ U_{fp}(\mathbf{x_f}_q) &= \delta_{pq} \quad \forall p, q \in [1, N_f]\end{aligned} \tag{4.6}$$

with δ_{pq} the Kronecker delta function,

$$\delta_{pq} = \begin{cases} 1 & \text{if} \quad p = q \\ 0 & \text{if} \quad p \neq q \end{cases} \tag{4.7}$$

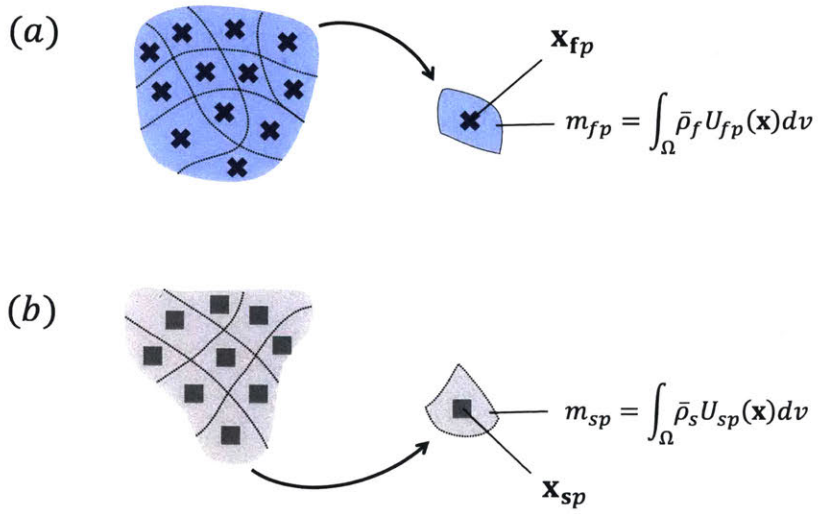

Figure 4-2: (a) The fluid phase is discretized into N_f material points with centroid locations $\{\mathbf{x}_{\mathbf{f}p}\}$ and masses $\{m_{fp}\}$. (b) The solid phase is discretized into N_s material points with centroid locations $\{\mathbf{x}_{\mathbf{s}p}\}$ and masses $\{m_{sp}\}$.

4.1.2 Definition of Background Grid Basis

In addition to the material point representation of the continuum bodies, we also use a grid or nodal basis for the purpose of solving the weak form equations of motion and approximating material fields (for post-processing and simplifying intermediate calculations). Since both bodies live within the same computational domain, Ω, we let one discrete grid serve this purpose for the entire mixture. The grid is defined by continuous piece-wise basis functions,

$$\sum_{i=1}^{[n]} \mathcal{N}_i(\mathbf{x}) = 1 \quad \forall \mathbf{x} \in \Omega \tag{4.8}$$

where $\mathcal{N}_i(\mathbf{x})$ is the ith nodal basis function and $[n]$ is the total number of nodes (or degrees of freedom if discontinuous shape functions are used). With this definition we can then define

the following nodal fields,

$$\begin{aligned}
\frac{D^s\mathbf{v_s}}{Dt}(\mathbf{x}) = \mathbf{a_s}(\mathbf{x}) &= \sum_{i=1}^{[n]} \mathbf{a}_{\mathbf{s}i}\mathcal{N}_i(\mathbf{x}) \\
\mathbf{v_s}(\mathbf{x}) &= \sum_{i=1}^{[n]} \mathbf{v}_{\mathbf{s}i}\mathcal{N}_i(\mathbf{x}) \\
\frac{D^f\mathbf{v_f}}{Dt}(\mathbf{x}) = \mathbf{a_f}(\mathbf{x}) &= \sum_{i=1}^{[n]} \mathbf{a}_{\mathbf{f}i}\mathcal{N}_i(\mathbf{x}) \\
\mathbf{v_f}(\mathbf{x}) &= \sum_{i=1}^{[n]} \mathbf{v}_{\mathbf{f}i}\mathcal{N}_i(\mathbf{x}) \\
\mathbf{w}(\mathbf{x}) &= \sum_{i=1}^{[n]} \mathbf{w}_i\mathcal{N}_i(\mathbf{x}) \\
n(\mathbf{x}) &= \sum_{i=1}^{[n]} n_i\mathcal{N}_i(\mathbf{x})
\end{aligned} \tag{4.9}$$

where ψ_i represents a constant (scalar, vector, or tensor) associated with the field $\psi(\mathbf{x})$ and the ith nodal basis. $\mathbf{w}(\mathbf{x})$ is an arbitrary test function which is used in forming the discrete system of equations from the weak form of the governing equations.

In addition to the fields above, we also introduce a measure of the nodal basis weight, V_i,

$$V_i = \int_\Omega \mathcal{N}_i(\mathbf{x})dv \tag{4.10}$$

It is numerically convenient to let the background grid be composed of regular Cartesian elements. We therefore let the construction of the basis functions $\{\mathcal{N}_i(\mathbf{x})\}$ be the tensor product of 1D functions $\mathcal{N}_{1\mathrm{D}}(x)$ (see Figure 4-3) with x a measure of the distance from the grid node to the spatial position $\mathbf{x}$ along one of the primary Cartesian directions, $\{\hat{x}, \hat{y}, \hat{z}\}$,

$$\begin{aligned}
&\text{1D} \quad \mathcal{N}_i(\mathbf{x}) = \mathcal{N}_{1\mathrm{D}}(x) \\
&\text{2D} \quad \mathcal{N}_i(\mathbf{x}) = \mathcal{N}_{1\mathrm{D}}(x)\, \mathcal{N}_{1\mathrm{D}}(y) \\
&\text{3D} \quad \mathcal{N}_i(\mathbf{x}) = \mathcal{N}_{1\mathrm{D}}(x)\, \mathcal{N}_{1\mathrm{D}}(y)\, \mathcal{N}_{1\mathrm{D}}(z)
\end{aligned} \tag{4.11}$$

The choice of $\mathcal{N}_{1\mathrm{D}}(x)$ can have significant impact on the accuracy of the material point method especially for reduction of 'grid-crossing' error (see Bardenhagen and Kober [2004]) and quadrature error (see Steffen et al. [2008]).

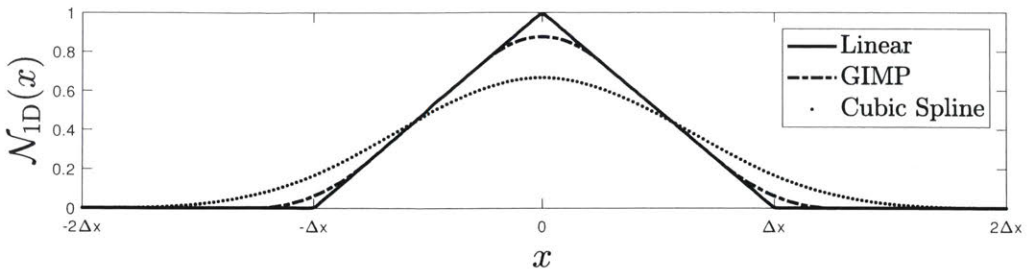

Figure 4-3: The nodal basis functions $\{\mathcal{N}_i(\mathbf{x})\}$ are defined on a Cartesian grid by the product of 1D functions $\mathcal{N}_{1D}(x)$ in each of the primary directions $\{\hat{x}, \hat{y}, \hat{z}\}$. In this work, we use the basic linear shape functions from Sulsky et al. [1994] (shown by the solid curve), the GIMP shape functions from Bardenhagen and Kober [2004] (shown by dashed curve), or the cubic splines defined in Steffen et al. [2008] (shown by the dotted curve).

4.1.3 Definition of Lagrangian Motion

As stated in Section 4.1.1, we define the material point characteristic functions $U_{sp}(\mathbf{x})$ and $U_{fp}(\mathbf{x})$ to be co-moving with the material. We therefore require that the material point centroids move according to the following rule,

$$\begin{aligned} \frac{d}{dt}(\mathbf{x}_{\mathbf{s}p}) &= \mathbf{v}_{\mathbf{s}}(\mathbf{x}_{\mathbf{s}p}) \qquad \forall p \in [1, N_s] \\ \frac{d}{dt}(\mathbf{x}_{\mathbf{f}p}) &= \mathbf{v}_{\mathbf{f}}(\mathbf{x}_{\mathbf{f}p}) \qquad \forall p \in [1, N_f] \end{aligned} \tag{4.12}$$

and, as in Brackbill and Ruppel [1986] and Brackbill et al. [1988], we separately evolve the material point velocity coefficients according to,

$$\begin{aligned} \frac{d}{dt}(\mathbf{v}_{\mathbf{s}p}) &= \mathbf{a}_{\mathbf{s}}(\mathbf{x}_{\mathbf{s}p}) \qquad \forall p \in [1, N_s] \\ \frac{d}{dt}(\mathbf{v}_{\mathbf{f}p}) &= \mathbf{a}_{\mathbf{f}}(\mathbf{x}_{\mathbf{f}p}) \qquad \forall p \in [1, N_f] \end{aligned} \tag{4.13}$$

Therefore, arbitrary functions $f_s(\mathbf{x})$ and $f_f(\mathbf{x})$ defined by the sets of coefficients $\{f_{sp}\}$ and $\{f_{fp}\}$ as follows,

$$f_s(\mathbf{x}) = \sum_{p=1}^{N_s} f_{sp} U_{sp}(\mathbf{x})$$

$$f_f(\mathbf{x}) = \sum_{p=1}^{N_f} f_{fp} U_{fp}(\mathbf{x})$$

have the following useful properties. First, by Equation (4.6), the function coefficients are collocated with the material point centroids,

$$f_{sp} = f_s(\mathbf{x}_{\mathbf{s}p}) \quad \forall p \in [1, N_s]$$

$$f_{fp} = f_s(\mathbf{x}_{\mathbf{f}p}) \quad \forall p \in [1, N_f]$$

and, as a consequence of the definition of the material point centroid motion from Equation (4.12), the coefficients of $f_s(\mathbf{x})$ and $f_f(\mathbf{x})$ evolve according to,

$$\frac{d}{dt}(f_{sp}) \equiv \left.\frac{D^s f_s(\mathbf{x})}{Dt}\right|_{\mathbf{x}_{\mathbf{s}p}} \quad \forall p \in [1, N_s]$$

$$\frac{d}{dt}(f_{fp}) \equiv \left.\frac{D^f f_f(\mathbf{x})}{Dt}\right|_{\mathbf{x}_{\mathbf{f}p}} \quad \forall p \in [1, N_f]$$

4.1.4 Weak Form of Momentum Balance Equations

We consider an expression for the weak form of the solid and fluid phase momentum balance given in Equations (2.21) and (2.22),

$$\int_\Omega \left(\bar{\rho}_s \frac{D^s \mathbf{v_s}}{Dt} \cdot \mathbf{w}\right) dv = \int_\Omega \left(\bar{\rho}_s \mathbf{g} \cdot \mathbf{w} - \mathbf{f_d} \cdot \mathbf{w} + \operatorname{div}(\tilde{\boldsymbol{\sigma}}) \cdot \mathbf{w} - (1-n)\operatorname{grad}(p_f) \cdot \mathbf{w}\right) dv$$

$$\int_\Omega \left(\bar{\rho}_f \frac{D^f \mathbf{v_f}}{Dt} \cdot \mathbf{w}\right) dv = \int_\Omega \left(\bar{\rho}_f \mathbf{g} \cdot \mathbf{w} + \mathbf{f_d} \cdot \mathbf{w} + \operatorname{div}(\boldsymbol{\tau_f}) \cdot \mathbf{w} - n\operatorname{grad}(p_f) \cdot \mathbf{w}\right) dv$$

or equivalently,

$$\begin{aligned}
\int_\Omega \left(\bar{\rho}_s \frac{D^s \mathbf{v_s}}{Dt} \cdot \mathbf{w}\right) dv &= \int_\Omega \left((\bar{\rho}_s \mathbf{g} - \mathbf{f_d}) \cdot \mathbf{w} + (1-n) p_f \operatorname{grad}(\mathbf{w}) - \tilde{\boldsymbol{\sigma}} : \operatorname{grad}(\mathbf{w})\right) dv + \int_{\partial\Omega} (\mathbf{t_s}(\mathbf{n}) \cdot \mathbf{w}) da \\
\int_\Omega \left(\bar{\rho}_f \frac{D^f \mathbf{v_f}}{Dt} \cdot \mathbf{w}\right) dv &= \int_\Omega \left((\bar{\rho}_f \mathbf{g} \cdot \mathbf{w} + \mathbf{f_d}) \cdot \mathbf{w} + n p_f \operatorname{grad}(\mathbf{w}) - \boldsymbol{\tau_f} : \operatorname{grad}(\mathbf{w})\right) dv + \int_{\partial\Omega} (\mathbf{t_f}(\mathbf{n}) \cdot \mathbf{w}) da
\end{aligned} \tag{4.14}$$

where we let Ω be the entire domain of interest, $\partial\Omega$ be the boundary of that domain, and $\mathbf{w}$ a test function. Using the point and nodal representations of the continuum fields from

Sections 4.1.1 and 4.1.2, we create a system of $2[n]$ equations given as follows,

$$\begin{aligned}\sum_{p=1}^{N_s}\sum_{j=1}^{[n]}\bar{\rho}_{sp}\mathbf{a_s}_j\int_\Omega \mathcal{N}_j(\mathbf{x})\mathcal{N}_i(\mathbf{x})U_{sp}(\mathbf{x})dv = &\sum_{p=1}^{N_s}\bar{\rho}_{sp}\mathbf{g}\int_\Omega \mathcal{N}_i(\mathbf{x})U_{sp}(\mathbf{x})dv\\ &-\sum_{p=1}^{N_s}\tilde{\boldsymbol{\sigma}}_p\int_\Omega \text{grad}\left(\mathcal{N}_i(\mathbf{x})\right)U_{sp}(\mathbf{x})dv\\ &+\sum_{p=1}^{N_f}(1-n_i)p_{fp}\int_\Omega \text{grad}\left(\mathcal{N}_i(\mathbf{x})\right)U_{sp}(\mathbf{x})dv\\ &-\int_\Omega \mathbf{f_d}\mathcal{N}_i(\mathbf{x})dv+\int_{\partial\Omega}(\mathbf{t_s}(\mathbf{n})\mathcal{N}_i(\mathbf{x}))da\\ &\forall i\in[1,[n]]\end{aligned} \tag{4.15}$$

and,

$$\begin{aligned}\sum_{p=1}^{N_s}\sum_{j=1}^{[n]}\bar{\rho}_{fp}\mathbf{a_f}_j\int_\Omega \mathcal{N}_j(\mathbf{x})\mathcal{N}_i(\mathbf{x})U_{fp}(\mathbf{x})dv = &\sum_{p=1}^{N_f}\bar{\rho}_{fp}\mathbf{g}\int_\Omega \mathcal{N}_i(\mathbf{x})U_{fp}(\mathbf{x})dv\\ &-\sum_{p=1}^{N_f}\boldsymbol{\tau}_{\boldsymbol{f}p}\int_\Omega \text{grad}\left(\mathcal{N}_i(\mathbf{x})\right)U_{fp}(\mathbf{x})dv\\ &+\sum_{p=1}^{N_f}n_ip_{fi}\int_\Omega \text{grad}\left(\mathcal{N}_i(\mathbf{x})\right)U_{fp}(\mathbf{x})dv\\ &+\int_\Omega \mathbf{f_d}\mathcal{N}_i(\mathbf{x})dv+\int_{\partial\Omega}(\mathbf{t_f}(\mathbf{n})\mathcal{N}_i(\mathbf{x}))da\\ &\forall i\in[1,[n]]\end{aligned} \tag{4.16}$$

For numerical efficiency, we assume the following simplifications. First, we use a one point quadrature scheme to simplify the following integral expressions,

$$\begin{aligned}\mathcal{S}_{sip}\equiv&\frac{1}{v_{sp}}\int_\Omega \mathcal{N}_i(\mathbf{x})U_{sp}(\mathbf{x})dv \quad\approx\quad \mathcal{N}_i(\mathbf{x_s}_p)\\ \mathcal{S}_{fip}\equiv&\frac{1}{v_{fp}}\int_\Omega \mathcal{N}_i(\mathbf{x})U_{fp}(\mathbf{x})dv \quad\approx\quad \mathcal{N}_i(\mathbf{x_f}_p)\end{aligned} \tag{4.17}$$

and,

$$\begin{aligned}\nabla\mathcal{S}_{sip}\equiv&\frac{1}{v_{sp}}\int_\Omega \text{grad}\left(\mathcal{N}_i(\mathbf{x})\right)U_{sp}(\mathbf{x})dv \quad\approx\quad \text{grad}\left(\mathcal{N}_i(\mathbf{x})\right)\big|_{\mathbf{x_s}_p}\\ \nabla\mathcal{S}_{fip}\equiv&\frac{1}{v_{fp}}\int_\Omega \text{grad}\left(\mathcal{N}_i(\mathbf{x})\right)U_{fp}(\mathbf{x})dv \quad\approx\quad \text{grad}\left(\mathcal{N}_i(\mathbf{x})\right)\big|_{\mathbf{x_f}_p}\end{aligned} \tag{4.18}$$

Second, the left hand side of the expressions in Equations (4.15) and (4.16) can be expressed as a matrix vector product acting on a vector of the acceleration coefficients $\mathbf{a}_{\mathbf{s}i}$ or $\mathbf{a}_{\mathbf{f}i}$. As in Sulsky et al. [1994], we diagonalize the matrix and find the following reductions,

$$\begin{aligned}
\sum_{j=1}^{[n]} \mathbf{a}_{\mathbf{s}j} \int_\Omega \mathcal{N}_j(\mathbf{x})\mathcal{N}_i(\mathbf{x})U_{sp}(\mathbf{x})dv &\approx v_{sp}\mathcal{S}_{sip}\mathbf{a}_{\mathbf{s}i} \\
\sum_{j=1}^{[n]} \mathbf{a}_{\mathbf{f}j} \int_\Omega \mathcal{N}_j(\mathbf{x})\mathcal{N}_i(\mathbf{x})U_{fp}(\mathbf{x})dv &\approx v_{fp}\mathcal{S}_{fip}\mathbf{a}_{\mathbf{f}i}
\end{aligned} \tag{4.19}$$

These simplifications reduce the weak form system of $2[n]$ equations into the following form,

$$\begin{aligned}
m_{si}\mathbf{a}_{\mathbf{s}i} &= m_{si}\mathbf{g} - \mathbf{f}_{\mathbf{d}i} - \sum_{p=1}^{N_s}\left(v_{sp}\tilde{\boldsymbol{\sigma}}_p\nabla\mathcal{S}_{sip}\right) + (1-n_i)\sum_{p=1}^{N_f}\left(v_{fp}p_{fp}\nabla\mathcal{S}_{sip}\right) + \mathbf{s}_{\mathbf{s}i} \qquad \forall i \in [1,[n]] \\
m_{fi}\mathbf{a}_{\mathbf{f}i} &= m_{fi}\mathbf{g} + \mathbf{f}_{\mathbf{d}i} - \sum_{p=1}^{N_f}\left(v_{fp}\boldsymbol{\tau}_{\boldsymbol{f}_p}\nabla\mathcal{S}_{fip}\right) + n_i\sum_{p=1}^{N_f}\left(v_{fp}p_{fp}\nabla\mathcal{S}_{sip}\right) + \mathbf{s}_{\mathbf{f}i} \qquad \forall i \in [1,[n]]
\end{aligned} \tag{4.20}$$

where m_{si} and m_{fi} are nodal mass coefficients given by,

$$\begin{aligned}
m_{si} &= \sum_{p=1}^{N_s} m_{sp}\mathcal{S}_{sip} \\
m_{fi} &= \sum_{p=1}^{N_f} m_{fp}\mathcal{S}_{fip}
\end{aligned} \tag{4.21}$$

and where n_i are the $[n]$ coefficients which define the nodal approximation of the porosity field given by,

$$n_i = 1 - \frac{m_{si}}{V_i\rho_s} \tag{4.22}$$

and $\mathbf{f}_{\mathbf{d}i}$, $\mathbf{s}_{\mathbf{s}i}$, and $\mathbf{s}_{\mathbf{f}i}$ approximates the remaining integrals in Equations (4.15) and (4.16). $\mathbf{s}_{\mathbf{s}i}$ and $\mathbf{s}_{\mathbf{f}i}$ are given by the boundary conditions defined on $\partial\Omega$. $\mathbf{f}_{\mathbf{d}i}$ is given as follows,

$$\mathbf{f}_{\mathbf{d}i} = \frac{18n_i(1-n_i)\eta_0}{d^2}\,\hat{F}((1-n_i),\mathrm{Re}_i)\,(\mathbf{v}_{\mathbf{s}i} - \mathbf{v}_{\mathbf{f}i})\sum_{p=1}^{N_f} v_{pf}\mathcal{S}_{fip} \tag{4.23}$$

with $\hat{F}$ defined in Equation (2.38) and,

$$\mathrm{Re}_i = \frac{n_i\|\mathbf{v}_{\mathbf{s}i} - \mathbf{v}_{\mathbf{f}i}\|\rho_{f0}\,d}{\eta_0} \tag{4.24}$$

4.1.5 Discrete Mass Balance

By defining the material point characteristic functions according to the rules in Section 4.1.1, we can define a set of N_s solid phase and N_f fluid phase equations governing the evolution of the coefficients $\bar{\rho}_{sp}$ and $\bar{\rho}_{fp}$ respectively,

$$\begin{aligned} \frac{d}{dt}(\bar{\rho}_{sp}) &\equiv \left.\frac{D^s\bar{\rho}_s}{Dt}\right|_{\mathbf{x_s}_p} = -\bar{\rho}_{sp}\,\mathrm{div}\,\mathbf{v_s}\big|_{\mathbf{x_s}_p} \qquad \forall p \in [1, N_s] \\ \frac{d}{dt}(\bar{\rho}_{fp}) &\equiv \left.\frac{D^f\bar{\rho}_f}{Dt}\right|_{\mathbf{x_f}_p} = -\bar{\rho}_{fp}\,\mathrm{div}\,\mathbf{v_f}\big|_{\mathbf{x_f}_p} \qquad \forall p \in [1, N_f] \end{aligned} \tag{4.25}$$

where,

$$\begin{aligned} \mathrm{div}(\mathbf{v_s})\big|_{\mathbf{x_s}_p} &= \mathrm{tr}\left(\sum_{i=1}^{[n]} \mathbf{v_s}_i \otimes \nabla\mathcal{S}_{sip}\right) \\ \mathrm{div}(\mathbf{v_f})\big|_{\mathbf{x_f}_p} &= \mathrm{tr}\left(\sum_{i=1}^{[n]} \mathbf{v_f}_i \otimes \nabla\mathcal{S}_{fip}\right) \end{aligned} \tag{4.26}$$

and $\otimes$ is the tensor product operator such that

$$\mathbf{u} \otimes \mathbf{v} = \mathbf{u} * (\mathbf{v}^\top) = \begin{bmatrix} \mathbf{u}_1\mathbf{v}_1 & \mathbf{u}_1\mathbf{v}_2 & \mathbf{u}_1\mathbf{v}_3 \\ \mathbf{u}_2\mathbf{v}_1 & \mathbf{u}_2\mathbf{v}_2 & \mathbf{u}_2\mathbf{v}_3 \\ \mathbf{u}_3\mathbf{v}_1 & \mathbf{u}_3\mathbf{v}_2 & \mathbf{u}_3\mathbf{v}_3 \end{bmatrix}$$

Then, by Equation (4.5) we also have,

$$\begin{aligned} \frac{d}{dt}(v_{sp}) &= v_{sp}\,\mathrm{div}\,\mathbf{v_s}\big|_{\mathbf{x_s}_p} \qquad \forall p \in [1, N_s] \\ \frac{d}{dt}(v_{fp}) &= v_{fp}\,\mathrm{div}\,\mathbf{v_f}\big|_{\mathbf{x_f}_p} \qquad \forall p \in [1, N_f] \end{aligned} \tag{4.27}$$

4.1.6 Discrete True Fluid Density Evolution

As in Equation (4.25), we define N_f equations which govern the evolution of the set of coefficients $\{\rho_{fp}\}$ as follows,

$$\frac{d}{dt}(\rho_{fp}) \equiv \left.\frac{D^f\rho_f}{Dt}\right|_{\mathbf{x_f}_p} = -\left(\frac{\rho_f}{n}\,\mathrm{div}\left((1-n)\mathbf{v_s} + n\mathbf{v_f}\right)\right)\Bigg|_{\mathbf{x_f}_p} \qquad \forall p \in [1, N_f] \tag{4.28}$$

which can be approximated by the system,

$$\frac{d}{dt}(\rho_{fp}) \approx -\frac{\rho_{fp}}{n_p}\,\mathrm{tr}\left(\sum_{i=1}^{[n]} \left[(1-n_i)\mathbf{v_s}_i + n_i\mathbf{v_f}_i\right] \otimes \nabla\mathcal{S}_{fip}\right) \qquad \forall p \in [1, N_f] \tag{4.29}$$

where n_p is given by,

$$n_p = \sum_{i=1}^{[n]} n_i \mathcal{S}_{fip} \tag{4.30}$$

4.1.7 Discrete Fluid Pore Pressure

The set of coefficients $\{p_{fp}\}$ are determined by collocation of Equation (2.87) with the material point centroids according to,

$$p_{fp} = \kappa \ln\left(\frac{\rho_{fp}}{\rho_{0f}}\right) \quad \forall p \in [1, N_f] \tag{4.31}$$

4.1.8 Discrete Fluid Shear Stress

The set of coefficients $\{\boldsymbol{\tau}_{\boldsymbol{f}_p}\}$ are determined by collocation of Equation (2.88) with the material point centroids according to,

$$\boldsymbol{\tau}_{\boldsymbol{f}_p} = 2\eta_0\big(1 + \tfrac{5}{2}(1 - n_p)\big)\mathbf{D}_{\mathbf{0f}p} \quad \forall p \in [1, N_f] \tag{4.32}$$

with n_p given by Equation (4.30) and $\mathbf{D}_{\mathbf{f}p}$ the symmetric part of the velocity gradient at the material point centroid,

$$\mathbf{D}_{\mathbf{f}p} = \operatorname{sym}\left(\sum_{i=1}^{[n]} \mathbf{v}_{\mathbf{f}i} \otimes \nabla \mathcal{S}_{fip}\right) \tag{4.33}$$

4.1.9 Discrete Effective Granular Stress Evolution

The discretized solid phase effective granular stress field evolves according to the N_s equations derived by collocating Equation (2.101) at the material point centroids,

$$\frac{d}{dt}(\tilde{\boldsymbol{\sigma}}_p) \equiv \left.\frac{D^s\tilde{\boldsymbol{\sigma}}}{Dt}\right|_{\mathbf{x}_{\mathbf{s}p}} = 2G\mathbf{D}^{\mathbf{e}}_{\mathbf{0}p} + K\operatorname{tr}(\mathbf{D}^{\mathbf{e}}{}_p)\mathbf{1} + \mathbf{W}_{\mathbf{s}p}\tilde{\boldsymbol{\sigma}}_p - \tilde{\boldsymbol{\sigma}}_p\mathbf{W}_{\mathbf{s}p} \quad \forall p \in [1, N_s] \tag{4.34}$$

with,

$$\mathbf{D}^{\mathbf{e}}_{\mathbf{0}p} = \mathbf{D}^{\mathbf{e}}{}_p - \tfrac{1}{3}\operatorname{tr}\left(\mathbf{D}^{\mathbf{e}}{}_p\right)\mathbf{1}$$

and,

$$\mathbf{D}^{\mathbf{e}}{}_p = \mathbf{D}_{\mathbf{s}p} - \boldsymbol{\Gamma}^{\mathbf{p}}{}_p$$

The symmetric and skew symmetric parts of the solid phase velocity gradient at the material centroids are given by,

$$\mathbf{D}_{\mathbf{s}p} = \operatorname{sym}(\mathbf{L}_{\mathbf{s}p}), \qquad \mathbf{W}_{\mathbf{s}p} = \operatorname{skw}(\mathbf{L}_{\mathbf{s}p})$$

where,

$$\mathbf{L}_{\mathbf{s}p} = \sum_{i=1}^{[n]} \mathbf{v}_{\mathbf{s}i} \otimes \nabla \mathcal{S}_{sip} \tag{4.35}$$

The set of plastic flow rates $\{\mathbf{\Gamma^p}_p\}$ must be determined at each material point independently according to the rules developed in Section 2.3.16 and summarized in Table 4.2.

4.2 Time Marching Procedure

For time integration, we consider an explicit method for determining the state of the system at discrete time-steps. The following procedure (shown in Figure 4-4) is used to step from time t^k to time t^{k+1} where,

$$t^{k+1} = t^k + \Delta t = k\Delta t \tag{4.36}$$

We let the superscript k above a scalar value ψ_α^k represent the value of $\psi_\alpha(t)$ at the discrete time t^k.

1. The discrete material point states of the two phases are known at time t^k.

$$\begin{aligned} &\text{solid phase:} && \{\bar{\rho}_{sp}^k, \tilde{\boldsymbol{\sigma}}_p^k, m_{sp}, \mathbf{x}_{\mathbf{s}p}^k, \mathbf{v}_{\mathbf{s}p}^k\} \\ &\text{fluid phase:} && \{\bar{\rho}_{fp}^k, \rho_{fp}^k, \boldsymbol{\tau}_{\boldsymbol{f}p}^k, p_{fp}^k, m_{fp}, \mathbf{x}_{\mathbf{f}p}^k, \mathbf{v}_{\mathbf{f}p}^k\} \end{aligned}$$

2. The material point centroids, $\{\mathbf{x}_{\mathbf{s}p}^k\}$ and $\{\mathbf{x}_{\mathbf{f}p}^k\}$ are used to generate the mapping coefficients $\{\mathcal{S}_{sip}^k\}$, $\{\mathcal{S}_{fip}^k\}$, $\{\nabla\mathcal{S}_{sip}^k\}$, and $\{\nabla\mathcal{S}_{fip}^k\}$ according to Equations (4.17) and (4.18).

$$\begin{aligned} \mathcal{S}_{sip}^k &= \mathcal{N}_i(\mathbf{x}_{\mathbf{s}p}^k), & \nabla\mathcal{S}_{sip}^k &= \text{grad}\left(\mathcal{N}_i(\mathbf{x})\right)\big|_{\mathbf{x}_{\mathbf{s}p}^k} \\ \mathcal{S}_{fip}^k &= \mathcal{N}_i(\mathbf{x}_{\mathbf{f}p}^k), & \nabla\mathcal{S}_{fip}^k &= \text{grad}\left(\mathcal{N}_i(\mathbf{x})\right)\big|_{\mathbf{x}_{\mathbf{f}p}^k} \end{aligned}$$

3. The nodal mass coefficients, $\{m_{si}^k\}$ and $\{m_{fi}^k\}$, are determined according to Equation (4.21).

$$m_{si}^k = \sum_{p=1}^{N_s} m_{sp}\mathcal{S}_{sip}^k, \qquad m_{fi}^k = \sum_{p=1}^{N_f} m_{fp}\mathcal{S}_{fip}^k$$

4. An intermediate nodal representation of the phase velocity fields, given by the coefficients $\{\mathbf{v}_{\mathbf{s}i}^*\}$ and $\{\mathbf{v}_{\mathbf{f}i}^*\}$, is determined by approximating the material point velocity

field, given by the coefficients $\{\mathbf{v}_{\mathbf{s}p}^k\}$ and $\{\mathbf{v}_{\mathbf{f}p}^k\}$.

$$\begin{aligned} m_{si}^k \mathbf{v}_{\mathbf{s}i}^* &= \sum_{p=1}^{N_s} m_{sp} \mathbf{v}_{\mathbf{s}p}^k \mathcal{S}_{sip}^k \\ m_{fi}^k \mathbf{v}_{\mathbf{f}i}^* &= \sum_{p=1}^{N_f} m_{fp} \mathbf{v}_{\mathbf{f}p}^k \mathcal{S}_{sip}^k \end{aligned} \tag{4.37}$$

5. The nodal porosity coefficients, $\{n_i^k\}$, are determined according to Equation (4.22).

$$n_i^k = 1 - \frac{m_{si}^k}{V_i \rho_s}$$

6. The nodal approximation of the inter-phase drag, given by $\{\mathbf{f}_{\mathbf{d}i}^*\}$, is determined according to Equation (4.23).

$$\mathbf{f}_{\mathbf{d}i}^* = \frac{18 n_i^k (1 - n_i^k) \eta_0}{d^2} \hat{F}((1 - n_i^k), \mathrm{Re}_i^*) \, (\mathbf{v}_{\mathbf{s}i}^* - \mathbf{v}_{\mathbf{f}i}^*) \sum_{p=1}^{N_f} v_{pf}^k \mathcal{S}_{fip}^k$$

7. The acceleration of the solid phase at time t^{k+1}, given by $\{\mathbf{a}_{\mathbf{s}i}^{k+1}\}$, is determined by solving the explicit form of Equation (4.20).

$$m_{si}^k \mathbf{a}_{\mathbf{s}i}^{k+1} = m_{si}^k \mathbf{g} - \mathbf{f}_{\mathbf{d}i}^k - \sum_{p=1}^{N_s} \left(v_{sp}^k \tilde{\boldsymbol{\sigma}}_p^k \nabla \mathcal{S}_{sip}^k \right) + (1 - n_i^k) \sum_{p=1}^{N_f} \left(v_{fp}^k p_{fp}^k \nabla \mathcal{S}_{sip}^k \right) + \mathbf{s}_{\mathbf{s}i}^k$$

8. The acceleration of the fluid phase at time t^{k+1}, given by $\{\mathbf{a}_{\mathbf{f}i}^{k+1}\}$, is determined by solving the explicit form of Equation (4.20).

$$m_{fi}^k \mathbf{a}_{\mathbf{f}i}^{k+1} = m_{fi}^k \mathbf{g} + \mathbf{f}_{\mathbf{d}i}^k - \sum_{p=1}^{N_f} \left(v_{fp}^k \boldsymbol{\tau}_{\boldsymbol{f}p}^k \nabla \mathcal{S}_{fip}^k \right) + n_i^k \sum_{p=1}^{N_f} \left(v_{fp}^k p_{fp}^k \nabla \mathcal{S}_{fip}^k \right) + \mathbf{s}_{\mathbf{f}i}^k$$

9. The phase velocity fields at time t^{k+1}, given by $\{\mathbf{v}_{\mathbf{s}i}^{k+1}\}$ and $\{\mathbf{v}_{\mathbf{f}i}^{k+1}\}$, is determined explicitly according to,

$$\begin{aligned} \mathbf{v}_{\mathbf{s}i}^{k+1} &= \mathbf{v}_{\mathbf{s}i}^* + \Delta t \; \mathbf{a}_{\mathbf{s}i}^{k+1} \\ \mathbf{v}_{\mathbf{f}i}^{k+1} &= \mathbf{v}_{\mathbf{f}i}^* + \Delta t \; \mathbf{a}_{\mathbf{f}i}^{k+1} \end{aligned} \tag{4.38}$$

10. The material point centroid positions and velocities are updated explicitly according

to Equations (4.12) and (4.13),

$$\begin{aligned}
\mathbf{x}_{\mathbf{s}p}^{k+1} &= \mathbf{x}_{\mathbf{s}p}^{k} + \Delta t \sum_{i=1}^{[n]} \mathbf{v}_{\mathbf{s}i}^{k+1} \mathcal{S}_{sip}^{k} + (\boldsymbol{\delta}_{\boldsymbol{s}p}^{k}) \\
\mathbf{x}_{\mathbf{f}p}^{k+1} &= \mathbf{x}_{\mathbf{f}p}^{k} + \Delta t \sum_{i=1}^{[n]} \mathbf{v}_{\mathbf{f}i}^{k+1} \mathcal{S}_{fip}^{k} + (\boldsymbol{\delta}_{\boldsymbol{f}p}^{k}) \\
\mathbf{v}_{\mathbf{s}p}^{k+1} &= \mathbf{v}_{\mathbf{s}p}^{k} + \Delta t \sum_{i=1}^{[n]} \mathbf{a}_{\mathbf{s}i}^{k+1} \mathcal{S}_{sip}^{k} \\
\mathbf{v}_{\mathbf{f}p}^{k+1} &= \mathbf{v}_{\mathbf{f}p}^{k} + \Delta t \sum_{i=1}^{[n]} \mathbf{a}_{\mathbf{f}i}^{k+1} \mathcal{S}_{fip}^{k}
\end{aligned} \tag{4.39}$$

where $\boldsymbol{\delta}_{\boldsymbol{s}p}^{k+1}$ and $\boldsymbol{\delta}_{\boldsymbol{f}p}^{k+1}$ are the δ *position* correction described in Section 4.4.5.

11. The material point densities at time t^{k+1}, $\{\bar{\rho}_s^{k+1}\}$ and $\{\bar{\rho}_s^{k+1}\}$, are updated according to an explicit integration of Equation (4.25).

$$\begin{aligned}
\bar{\rho}_{sp}^{k+1} &= \bar{\rho}_{sp}^{k} \exp\left(- (\Delta t) \operatorname{tr}\left(\sum_{i=1}^{[n]} \mathbf{v}_{\mathbf{s}i}^{k+1} \otimes \nabla \mathcal{S}_{sip}^{k} \right) \right) \\
\bar{\rho}_{fp}^{k+1} &= \bar{\rho}_{fp}^{k} \exp\left(- (\Delta t) \operatorname{tr}\left(\sum_{i=1}^{[n]} \mathbf{v}_{\mathbf{f}i}^{k+1} \otimes \nabla \mathcal{S}_{fip}^{k} \right) \right)
\end{aligned}$$

12. The fluid phase material point *true* densities, $\{\rho_{fp}^{k+1}\}$, are determined by explicit integration of Equation (4.29). (Note that for numerical stability, we do not require that $\{n_p^{k+1}\}$, $\{\bar{\rho}_{fp}^{k+1}\}$, and $\{\rho_{fp}^{k+1}\}$ be consistent.)

$$n_p^{k+1} = \sum_{i=1}^{[n]} n_i^k \mathcal{S}_{fip}^k$$

$$\rho_{fp}^{k+1} = \rho_{fp}^{k} \exp\left(- \left(\frac{\Delta t}{n_p^{k+1}} \right) \operatorname{tr}\left(\sum_{i=1}^{[n]} [(1 - n_i^k)\mathbf{v}_{\mathbf{s}i}^{k+1} + n_i^k \mathbf{v}_{\mathbf{f}i}^{k+1}] \otimes \nabla \mathcal{S}_{fip}^{k} \right) \right)$$

13. The fluid phase material point pore pressure state is determined directly from the *true* fluid density by Equation (4.31).

$$p_{fp}^{k+1} = \kappa \ln\left(\frac{\rho_{fp}^{k+1}}{\rho_{0f}} \right)$$

14. The fluid phase material point shear stresses, $\{\boldsymbol{\tau}_{\boldsymbol{f}_p}^{k+1}\}$, are determined directly from the fluid phase velocity gradient according to Equation (4.32).

$$\boldsymbol{\tau}_{\boldsymbol{f}_p}^{k+1} = 2\eta_0\big(1 + \tfrac{5}{2}(1 - n_p^{k+1})\big)\mathbf{D}_{\mathbf{0f}_p}^{k+1}$$

$$\mathbf{D}_{\mathbf{f}_p}^{k+1} = \operatorname{sym}\left(\sum_{i=1}^{[n]} \mathbf{v}_{\mathbf{f}_i}^{k+1} \otimes \nabla \mathcal{S}_{fip}^{k}\right)$$

15. The solid phase material point effective stresses, $\{\tilde{\boldsymbol{\sigma}}_p^{k+1}\}$, are determined by integrating Equation (4.34) with a semi-implicit method described in Section 4.3.

$$\tilde{\boldsymbol{\sigma}}_p^{k+1} = \tilde{\boldsymbol{\sigma}}_p^{k} + \Delta t\big[2G\big(\mathbf{D}_{\mathbf{0s}p}^{k+1} - \boldsymbol{\Gamma}_{\mathbf{0}p}^{\mathbf{p}k+1}\big) + K\,\mathrm{tr}(\mathbf{D}_{\mathbf{s}p}^{k+1} - \boldsymbol{\Gamma}^{\mathbf{p}k+1}_{p})\mathbf{1} + \mathbf{W}_{\mathbf{s}p}^{k+1}\tilde{\boldsymbol{\sigma}}_p^{k} - \tilde{\boldsymbol{\sigma}}_p^{k}\mathbf{W}_{\mathbf{s}p}^{k+1}\big] \tag{4.40}$$

16. With discrete material point states of the two phases determined for time t^{k+1},

$$\begin{aligned} &\text{solid phase:} \quad \{\bar{\rho}_{sp}^{k+1}, \tilde{\boldsymbol{\sigma}}_p^{k+1}, m_{sp}, \mathbf{x}_{\mathbf{s}p}^{k+1}, \mathbf{v}_{\mathbf{s}p}^{k+1}\} \\ &\text{fluid phase:} \quad \{\bar{\rho}_{fp}^{k+1}, \rho_{fp}^{k+1}, \boldsymbol{\tau}_{\boldsymbol{f}_p}^{k+1}, p_{fp}^{k+1}, m_{fp}, \mathbf{x}_{\mathbf{f}p}^{k+1}, \mathbf{v}_{\mathbf{f}p}^{k+1}\} \end{aligned}$$

the procedure is repeated for the $k+1$ time-step.

4.3 Semi-Implicit Effective Stress Algorithm

The material point effective stress is updated at each time-step with the semi-implicit time integration scheme described in this section. Given the material point stress states at time t^k,

$$\{\tilde{\boldsymbol{\sigma}}_p^{k}\},$$

and the total material point flow rates at time t^{k+1}, $\{\mathbf{D}_{\mathbf{s}p}^{k+1}\}$ and $\{\mathbf{W}_{\mathbf{s}p}^{k+1}\}$ with,

$$\mathbf{D}_{\mathbf{s}p}^{k+1} = \operatorname{sym}(\mathbf{L}_{\mathbf{s}p}^{k+1}), \qquad \mathbf{W}_{\mathbf{s}p}^{k+1} = \operatorname{skw}(\mathbf{L}_{\mathbf{s}p}^{k+1}) \tag{4.41}$$

and,

$$\mathbf{L}_{\mathbf{s}p}^{k+1} = \sum_{i=1}^{[n]} \mathbf{v}_{\mathbf{s}i}^{k+1} \otimes \nabla \mathcal{S}_{sip}^{k}, \tag{4.42}$$

we solve for the plastic flow rates $\{\boldsymbol{\Gamma}^{\mathbf{p}k+1}_{p}\}$ given by,

$$\boldsymbol{\Gamma}^{\mathbf{p}k+1}_{p} = \frac{(\dot{\bar{\gamma}}^{p})_p^{k+1}}{\sqrt{2}} \frac{\tilde{\boldsymbol{\sigma}}_{\mathbf{0}p}^{k+1}}{\|\tilde{\boldsymbol{\sigma}}_{\mathbf{0}p}^{k+1}\|} + \frac{1}{3}\big(\beta(\dot{\bar{\gamma}}^{p})_p^{k+1} + (\dot{\xi}_1)_p^{k+1} + (\dot{\xi}_2)_p^{k+1}\big)\mathbf{1} \tag{4.43}$$

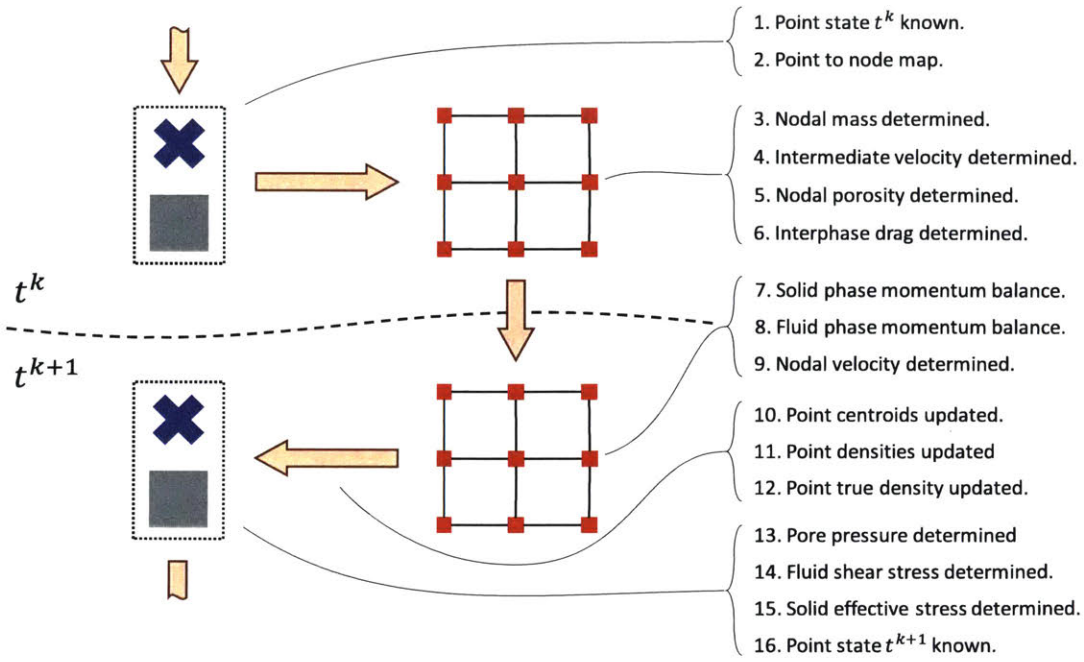

Figure 4-4: The explicit time integration procedure described in Section 4.2 is shown. At the beginning of the step, the material points carry the full state of the mixture. The mixture state is then mapped from the points to the background grid nodes, where the equations of motion are solved according to the weak form of momentum balance. At the end of the step, the solved equations of motion are used to update the mixture state on the material points.

such that (with $\{(\dot{\bar{\gamma}}^p)_p^{k+1},\ (\dot{\xi}_1)_p^{k+1}\ (\dot{\xi}_2)_p^{k+1}\}$ determined for each material point) the material point stress state at time t^{k+1} is given by Equation (4.40),

$$\tilde{\boldsymbol{\sigma}}_p^{k+1} = \tilde{\boldsymbol{\sigma}}_p^k + \Delta t\big[2G\big(\mathbf{D}_{0\mathbf{s}p}{}^{k+1} - \boldsymbol{\Gamma}_{0p}^{\mathbf{p}k+1}\big) + K\,\mathrm{tr}(\mathbf{D}_{\mathbf{s}p}{}^{k+1} - \boldsymbol{\Gamma}^{\mathbf{p}k+1}_p)\mathbf{1} + \mathbf{W}_{\mathbf{s}p}{}^{k+1}\tilde{\boldsymbol{\sigma}}_p^k - \tilde{\boldsymbol{\sigma}}_p^k\mathbf{W}_{\mathbf{s}p}{}^{k+1}\big]$$

4.3.1 Definition of Trial Stress

The update from Equation (4.40) can be separated into a trial step,

$$\tilde{\boldsymbol{\sigma}}_p^{tr} = \tilde{\boldsymbol{\sigma}}_p^k + \Delta t\big[2G\mathbf{D}_{0\mathbf{s}p}{}^{k+1} + K\,\mathrm{tr}(\mathbf{D}_{\mathbf{s}p}{}^{k+1})\mathbf{1} + \mathbf{W}_{\mathbf{s}p}{}^{k+1}\tilde{\boldsymbol{\sigma}}_p^k - \tilde{\boldsymbol{\sigma}}_p^k\mathbf{W}_{\mathbf{s}p}{}^{k+1}\big] \tag{4.44}$$

and a plastic step,

$$\tilde{\boldsymbol{\sigma}}_p^{k+1} = \tilde{\boldsymbol{\sigma}}_p^{tr} - \Delta t\big[2G\boldsymbol{\Gamma}_{0p}^{\mathbf{p}k+1} + K\,\mathrm{tr}(\boldsymbol{\Gamma}^{\mathbf{p}k+1}_p)\mathbf{1}\big] \tag{4.45}$$

where $\tilde{\boldsymbol{\sigma}}_p^{tr}$ is a *trial stress* found between times t^k and t^{k+1}. Since the trial stress given in Equation (4.44) is an explicit function of the strain-rates in Equations (4.41) and (4.42), we use it as the starting point of our implicit algorithm for solving Equation (4.45).

4.3.2 Simplification to Scalar Relation

The relation in Equation (4.45) is separable into a deviatoric part,

$$\tilde{\boldsymbol{\sigma}}_{\mathbf{0}_p}^{k+1} = \tilde{\boldsymbol{\sigma}}_{\mathbf{0}_p}^{tr} - 2G\Delta t \boldsymbol{\Gamma}_{\mathbf{0}_p}^{\mathbf{p}k+1} \tag{4.46}$$

and a spherical part,

$$\operatorname{tr}(\tilde{\boldsymbol{\sigma}})_p^{k+1} = \operatorname{tr}(\tilde{\boldsymbol{\sigma}})_p^{tr} - 3K\Delta \operatorname{tr}(\boldsymbol{\Gamma}^{\mathbf{p}}{}_p^{k+1}) \tag{4.47}$$

At first glance, these implicit expressions appear to be tensor relations; however, by introducing the following scalar stress measures, we reduce the implicit tensor relations to a set of implicit scalar relations (which are much simpler to solve numerically).

$$\begin{aligned} \bar{\tau}_p^{tr} &= \frac{\|\tilde{\boldsymbol{\sigma}}_{\mathbf{0}_p}^{tr}\|}{\sqrt{2}}, & \bar{\tau}_p^{k+1} &= \frac{\|\tilde{\boldsymbol{\sigma}}_p^{k+1}\|}{\sqrt{2}} \\ \tilde{p}_p^{tr} &= -\tfrac{1}{3}\operatorname{tr}(\tilde{\boldsymbol{\sigma}}_{\mathbf{0}_p}^{tr}), & \tilde{p}_p^{k+1} &= -\tfrac{1}{3}\operatorname{tr}(\tilde{\boldsymbol{\sigma}}_p^{k+1}) \end{aligned} \tag{4.48}$$

Returning to Equation (4.46), we substitute in the expression for the discretized plastic flow rate from Equation (4.43) to find,

$$\tilde{\boldsymbol{\sigma}}_{\mathbf{0}_p}^{k+1} = \tilde{\boldsymbol{\sigma}}_{\mathbf{0}_p}^{tr} - G\Delta t(\dot{\bar{\gamma}}^p)_p^{k+1}\sqrt{2}\frac{\tilde{\boldsymbol{\sigma}}_{\mathbf{0}_p}^{k+1}}{\|\tilde{\boldsymbol{\sigma}}_{\mathbf{0}_p}^{k+1}\|}$$

which suggest that $\tilde{\boldsymbol{\sigma}}_{\mathbf{0}_p}^{k+1}$ and $\tilde{\boldsymbol{\sigma}}_{\mathbf{0}_p}^{tr}$ are *co-directional* with,

$$\tilde{\boldsymbol{\sigma}}_{\mathbf{0}_p}^{k+1} = \frac{\bar{\tau}_p^{k+1}}{\bar{\tau}_p^{tr}}\tilde{\boldsymbol{\sigma}}_{\mathbf{0}_p}^{tr} \tag{4.49}$$

and,

$$\bar{\tau}_p^{k+1} = \bar{\tau}_p^{tr} - G\Delta t\ (\dot{\bar{\gamma}}^p)_p^{k+1} \tag{4.50}$$

Similarly, Equation (4.47) can be reduced to the simple relation,

$$\tilde{p}_p^{k+1} = \tilde{p}_p^{tr} + K\Delta t\big(\beta(\dot{\bar{\gamma}}^p)_p^{k+1} + (\dot{\xi}_1)_p^{k+1} + (\dot{\xi}_2)_p^{k+1}\big) \tag{4.51}$$

By solving the system of equations in (4.50) and (4.51) subject to the following discrete

yield conditions,

$$
\begin{aligned}
&(f_1)_p^{k+1} = \bar{\tau}_p^{k+1} - \max\left((\mu_p + \beta)\tilde{p}_p^{k+1},\ 0\right) \\
&(f_1)_p^{k+1} \leq 0, \qquad (\dot{\bar{\gamma}}^p)_p^{k+1} \geq 0, \qquad (f_1)_p^{k+1}(\dot{\bar{\gamma}}^p)_p^{k+1} = 0 \\
&\\
&(f_2)_p^{k+1} = -\tilde{p}_p^{k+1} \\
&(f_2)_p^{k+1} \leq 0, \qquad (\dot{\xi}_1)_p^{k+1} \geq 0, \qquad (f_2)_p^{k+1}(\dot{\xi}_1)_p^{k+1} = 0 \\
&\\
&(f_3)_p^{k+1} = \tilde{p}_p^{k+1} - g(\phi)\left[((\dot{\bar{\gamma}}^p)_p^{k+1} - K_5(\dot{\xi}_2)_p^{k+1})^2 d^2 \rho_s + 2\eta_0((\dot{\bar{\gamma}}^p)_p^{k+1} - K_5(\dot{\xi}_2)_p^{k+1})\right] \\
&(f_3)_p^{k+1} \leq 0, \qquad (\dot{\xi}_2)_p^{k+1} \leq 0, \qquad (f_3)_p^{k+1}(\dot{\xi}_2)_p^{k+1} = 0
\end{aligned}
\tag{4.52}
$$

we arrive at the final effective granular stresses at time t^{k+1},

$$
\tilde{\boldsymbol{\sigma}}_p^{k+1} = \frac{\bar{\tau}_p^{k+1}}{\bar{\tau}_p^{tr}} \tilde{\boldsymbol{\sigma}}_{\mathbf{0}p}^{tr} - \tilde{p}_p^{k+1}\mathbf{1} \tag{4.53}
$$

4.3.3 Complete Algorithm for Stress Update

The following section describes our method of solving for $\{\tilde{p}_p^{k+1}\}$ and $\{\bar{\tau}_p^{k+1}\}$ (and therefore $\{\tilde{\boldsymbol{\sigma}}_p^{k+1}\}$) given $\{\bar{\rho}_{sp}^{k+1}\}$, $\{\tilde{p}_p^{tr}\}$, $\{\bar{\tau}_p^{tr}\}$. This algorithm is designed to simply (but perhaps inefficiently) solve the non-linear system of equations given in Equations (4.50) and (4.51) subject to the inequality constraints given by the yield conditions (Equation (4.52)).

As shown in Figure 4-5, the basic algorithm involves taking the scalar trial stresses ($\{\tilde{p}_p^{tr}\}$ and $\{\bar{\tau}_p^{tr}\}$) and solving a sequence of projections to yield conditions. Once an admissible stress update is found, the algorithm exits and proceeds to the next time-step.

The essential flow of the full algorithm (see Algorithms 2, 3, 4, and 5) is briefly summarized in Algorithm 1.

Algorithm 1 Outline of Stress Update Procedure

1: **procedure** STRESS UPDATE
2: Determine trial state.
3: Check if trial stress is admissible (if so, **exit**).
4: Solve assuming final stress is on f_2 yield surface
5: Check if solved state is admissible (if so, **exit**).
6: Solve assuming final stress is on f_1 yield surface only.
7: Check if solved state is admissible (if so, **exit**).
8: Solve assuming final stress is on f_1 and f_3 yield surfaces.
9: This state must be admissible, so **exit**.
10: **end procedure**

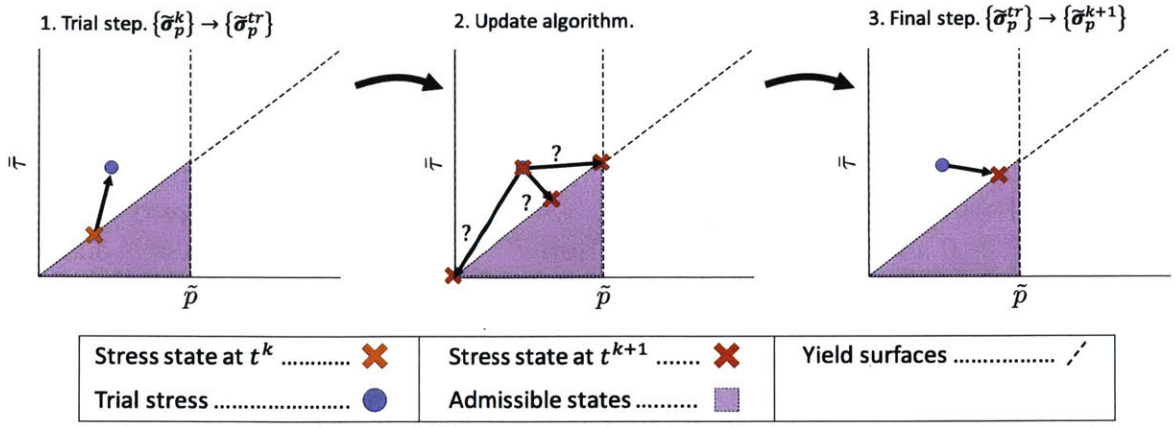

Figure 4-5: The basic solid phase effective stress update proceeds as follows. (1.) A trial step is taken from the stress state at time t^k assuming that all flow is elastic. (2.) The method described in Algorithm 4 and Algorithm 5 is used to determine how to project the trial stress to an admissible stress state. (3.) The final stress state is updated from the trial stress state.

Algorithm 2 Function for β

function BETA(ϕ, ϕ_m, $\dot{\tilde{\gamma}}^p$, $\tilde{p}$)
  $I_v = \eta_0 \dot{\tilde{\gamma}}^p / \tilde{p}$
  $I = \dot{\tilde{\gamma}} d \sqrt{\rho_s / \tilde{p}}$
  $I_m = \sqrt{I^2 + 2I_v}$
  $\phi_{eq} = \phi_m / (1 + aI_m)$
  if $\phi > \phi_m$ **then**
    $\beta = K_3(\phi - \phi_m) + K_4(\phi - \phi_{eq})$
  else
    $\beta = K_4(\phi - \phi_{eq})$
  end if
  return β
end function

Algorithm 3 Function for μ_p

function MU(ϕ, $\dot{\tilde{\gamma}}^p$, $\tilde{p}$)
  $I_v = \eta_0 \dot{\tilde{\gamma}}^p / \tilde{p}$
  $I = \dot{\tilde{\gamma}} d \sqrt{\rho_s / \tilde{p}}$
  $I_m = \sqrt{I^2 + 2I_v}$
  $\mu_p = \mu_1 + \dfrac{\mu_2 - \mu_1}{1 + b/I_m} + \frac{5}{2}\phi \dfrac{I_v}{aI_m}$
  return μ_p
end function

Algorithm 4 Stress Update Procedure (Part 1)

procedure STRESS UPDATE($\{\bar{\rho}_{sp}^{k+1}\}$, $\{\tilde{p}_p^{tr}\}$, $\{\bar{\tau}_p^{tr}\}$, τ_{min})
  for all $p \in [1, N_s]$ **do**
    $\phi = \bar{\rho}_{sp}^{k+1}/\rho_s$ ▷ calculate local packing fraction
    $\beta = \text{BETA}(\phi, \phi_m, 0, \tilde{p}_p^{tr})$ ▷ assume zero plastic flow
    if ($\tilde{p}_p^{tr} \geq 0$ and $\bar{\tau}_p^{tr} \leq (\mu_1 + \beta)\tilde{p}_p^{tr}$) **then** ▷ check if trial stress is admissible
      $\bar{\tau}_p^{k+1} = \bar{\tau}_p^{tr}$
      $\tilde{p}_p^{k+1} = \tilde{p}_p^{tr}$
      $(\dot{\bar{\gamma}}^p)_p^{k+1} = 0$
      EXIT ▷ continue to next p
    end if
    $\beta = \text{BETA}(\phi, \phi_m, \bar{\tau}_p^{tr}/(G\Delta t), 0)$ ▷ assume f_2 equality (zero pressure)
    if $\tilde{p}_p^{tr} + \bar{\tau}_p^{tr}\beta(K/G) \leq 0$ **then** ▷ check if f_2 stress is admissible
      $\bar{\tau}_p^{k+1} = 0$
      $\tilde{p}_p^{k+1} = 0$
      $(\dot{\bar{\gamma}}^p)_p^{k+1} = \bar{\tau}_p^{tr}/(G\Delta t)$
      EXIT ▷ continue to next p
    end if
    $\beta = \text{BETA}(\phi, \phi_m, 0, \tilde{p}_p^{tr})$ ▷ assume zero plastic flow
    $\bar{\tau}_0 = \tilde{p}_0 = 0$
    $\mathbf{r}_0 = \begin{bmatrix} \bar{\tau}_p^{tr} \\ -\left(\tilde{p}_p^{tr} + \bar{\tau}_p^{tr}\frac{\beta K}{G}\right) \end{bmatrix}$ ▷ initialize f_1 residual
    $\mathbf{b} = \mathbf{r}_0$
    $j = 0$
    while $\|\mathbf{r_k}\|/\|\mathbf{b}\| > \tau_{min}$ **do** ▷ assume f_1 equality (shear only)
      $\dot{\bar{\gamma}}_j^p = (\bar{\tau}_p^{tr} - \bar{\tau}_j)/(G\Delta t)$
      $\mu_p = \text{MU}(\phi, \dot{\bar{\gamma}}_j^p, \tilde{p}_j)$
      $\beta = \text{BETA}(\phi, \phi_m, \dot{\bar{\gamma}}_j^p, \tilde{p}_j)$
      $\mathbf{r}_j = \begin{bmatrix} \bar{\tau}_j - \max(0, \mu_p + \beta)\tilde{p}_j \\ \tilde{p}_j - \tilde{p}_p^{tr} - K\Delta t(\beta\dot{\bar{\gamma}}_j^p) \end{bmatrix}$ ▷ calculate f_1 residual
      $\mathbf{J} = \begin{bmatrix} \frac{\partial \mathbf{r}_{j1}}{\partial \bar{\tau}_j} & \frac{\partial \mathbf{r}_{j1}}{\partial \tilde{p}_j} \\ \frac{\partial \mathbf{r}_{j2}}{\partial \bar{\tau}_j} & \frac{\partial \mathbf{r}_{j2}}{\partial \tilde{p}_j} \end{bmatrix}$ ▷ determine f_1 residual Jacobian
      $\begin{bmatrix} \bar{\tau}_{j+1} \\ \tilde{p}_{j+1} \end{bmatrix} = \begin{bmatrix} \bar{\tau}_j \\ \tilde{p}_j \end{bmatrix} - \lambda\mathbf{J}^{-1}\mathbf{r_j}$ ▷ update guess with Newton method
      $j = j + 1$
    end while
    if ($\phi \geq \phi_m$ or $(\tilde{p}_j - g(\phi)[\dot{\bar{\gamma}}_j^{p2} d^2 \rho_s + 2\eta_0 \dot{\bar{\gamma}}_j^p]) \leq 0$) **then** ▷ check if f_1 stress is admissible
      $\bar{\tau}_p^{k+1} = \bar{\tau}_j$
      $\tilde{p}_p^{k+1} = \tilde{p}_j$
      $(\dot{\bar{\gamma}}^p)_p^{k+1} = (\bar{\tau}_p^{tr} - \bar{\tau}_p^{k+1})/(G\Delta t)$
      EXIT ▷ continue to next p
    end if
    ...

Algorithm 5 Stress Update Procedure (Part 2)

...

$\beta = \text{BETA}(\phi,\ \phi_m,\ \bar{\tau}_p^{tr}/(G\Delta t),\ 0)$ ▷ assume zero pressure

$\bar{\tau}_0 = \tilde{p}_0 = 0$

$\mathbf{r}_0 = \begin{bmatrix} \bar{\tau}_p^{tr} \\ -\left(\tilde{p}_p^{tr} + \bar{\tau}_p^{tr}\frac{\beta K}{G}\right) \end{bmatrix}$ ▷ initialize f_1, f_3 residual

$\mathbf{b} = \mathbf{r}_0$

$j = 0$

while $\|\mathbf{r_k}\|/\|\mathbf{b}\| > \tau_{min}$ **do** ▷ assume f_1, f_3 equality (shear and compaction)

$\dot{\bar{\gamma}}_j^p = (\bar{\tau}_p^{tr} - \bar{\tau}_j)/(G\Delta t)$

$\mu_p = \text{MU}(\phi,\ \dot{\bar{\gamma}}_j^p,\ \tilde{p}_j)$

$\beta = \text{BETA}(\phi,\ \phi_m,\ \dot{\bar{\gamma}}_j^p,\ \tilde{p}_j)$

$\dot{\xi}_2 = (\tilde{p}_j - \tilde{p}_p^{tr})/(K\Delta t) - \beta\dot{\bar{\gamma}}_j^p$

$\mathbf{r}_j = \begin{bmatrix} \bar{\tau}_j - \max(0, \mu_p + \beta)\tilde{p}_j \\ \tilde{p}_j - g(\phi)[(\dot{\bar{\gamma}}_j^p - K_5\dot{\xi}_2)^2 d^2 \rho_s + 2\eta_0(\dot{\bar{\gamma}}_j^p - K_5\dot{\xi}_2)] \end{bmatrix}$ ▷ calculate f_1, f_3 residual

$\mathbf{J} = \begin{bmatrix} \frac{\partial \mathbf{r}_{j1}}{\partial \bar{\tau}_j} & \frac{\partial \mathbf{r}_{j1}}{\partial \tilde{p}_j} \\ \frac{\partial \mathbf{r}_{j2}}{\partial \bar{\tau}_j} & \frac{\partial \mathbf{r}_{j2}}{\partial \tilde{p}_j} \end{bmatrix}$ ▷ determine f_1, f_3 residual Jacobian

$\begin{bmatrix} \bar{\tau}_{j+1} \\ \tilde{p}_{j+1} \end{bmatrix} = \begin{bmatrix} \bar{\tau}_j \\ \tilde{p}_j \end{bmatrix} - \lambda \mathbf{J}^{-1}\mathbf{r_j}$ ▷ update guess with Newton method

$j = j + 1$

end while

DONE ▷ continue to next p

end for

return $\{\tilde{p}_p^{k+1}\}, \{\bar{\tau}_p^{k+1}\}$

end procedure

4.4 Specific Notes About Implementation

In this section we briefly discuss the implementation of the boundary conditions, contact forces, partial saturation, and what we call the δ *position* correction.

4.4.1 Kinematic Boundary Conditions

The kinematic boundary condition used in this work is inherited from that used by Dunatunga and Kamrin [2015]. In this method, the components of the boundary force vectors, $\mathbf{s}_{\mathbf{s}_i}^k$ and $\mathbf{s}_{\mathbf{f}_i}^k$, on the boundary nodes are determined such that a given velocity, $\mathbf{v}_{\mathbf{s}final}$ and $\mathbf{v}_{\mathbf{f}final}$, is achieved at the end of the explicit time-step. In other words, $\mathbf{s}_{\mathbf{s}_i}^k$ and $\mathbf{s}_{\mathbf{f}_i}^k$ take on whatever value is necessary such that $\mathbf{a}_{\mathbf{s}_i}^{k+1}$ and $\mathbf{a}_{\mathbf{f}_i}^{k+1}$ (as given by Equation (4.20)) obey the following

relation,

$$\begin{aligned} \mathbf{s}_{\mathbf{s}i}^{k} \quad &\text{such that} \quad \mathbf{v}_{\mathbf{s}final} = \mathbf{v}_{\mathbf{s}i}^{*} + \Delta t \ \mathbf{a}_{\mathbf{s}i}^{k+1} \\ \mathbf{s}_{\mathbf{f}i}^{k} \quad &\text{such that} \quad \mathbf{v}_{\mathbf{f}final} = \mathbf{v}_{\mathbf{f}i}^{*} + \Delta t \ \mathbf{a}_{\mathbf{f}i}^{k+1} \end{aligned} \tag{4.54}$$

4.4.2 Mixed Boundary Conditions

In some simulations, we implement a frictional boundary condition on the solid phase. For these simulations, only the component of $\mathbf{v}_{\mathbf{s}final}$ normal to the boundary is prescribed (and therefore, the normal component of $\mathbf{s}_{\mathbf{s}i}^{k}$ is also determined). We then let the tangential force component obey the following rule,

$$\mathbf{s}_{\mathbf{s}i}^{k} - (\mathbf{s}_{\mathbf{s}i}^{k} \cdot \mathbf{n}_{\mathbf{b}i})\mathbf{n}_{\mathbf{b}i} = -\mu_1 \left\| \sum_{p=1}^{N_s} (v_{sp} \tilde{p}_p^k \nabla \mathcal{S}_{sip}) \right\| \frac{\mathbf{v}_{\mathbf{s}i}^{*} - (\mathbf{v}_{\mathbf{s}i}^{*} \cdot \mathbf{n}_{\mathbf{b}i})\mathbf{n}_{\mathbf{b}i}}{\|\mathbf{v}_{\mathbf{s}i}^{*} - (\mathbf{v}_{\mathbf{s}i}^{*} \cdot \mathbf{n}_{\mathbf{b}i})\mathbf{n}_{\mathbf{b}i}\|} \tag{4.55}$$

with the normal component given by,

$$(\mathbf{s}_{\mathbf{s}i}^{k} \cdot \mathbf{n}_{\mathbf{b}i}) \quad \text{such that} \quad (\mathbf{v}_{\mathbf{s}final} \cdot \mathbf{n}_{\mathbf{b}i}) = (\mathbf{v}_{\mathbf{s}i}^{*} + \Delta t \ \mathbf{a}_{\mathbf{s}i}^{k+1}) \cdot \mathbf{n}_{\mathbf{b}i} \tag{4.56}$$

where $\mathbf{n}_{\mathbf{b}i}$ is the boundary normal at the ith node.

4.4.3 Contact Algorithm

In some of the qualitative results presented in this work, we implement the contact algorithm from Huang et al. [2011]. This algorithm explicitly calculates an explicit inter-body force (when a third material body is introduced) which enforces a frictional, non-penetrating contact between the third body and each of the two phases presented in this work.

4.4.4 Partial Immersion

As mentioned in Section 2.1.2, in the parts of the solid body where there is no fluid, we say that the viscosity, η_0, is zero. Numerically, we accomplish this by constructing a nodal viscosity field at each time-step given by the coefficients $\{\eta_{0i}^k\}$ where,

$$\eta_{0i}^{k} = \begin{cases} \eta_0 & \text{if} \quad m_{fi}^{k} > 0 \\ 0 & \text{if} \quad m_{fi}^{k} = 0 \end{cases}$$

We then let the value of η_0 in Algorithms 2 and 3 be a function input. This input is equal to η_{0p} where,

$$\eta_{0p} = \sum_{i=1}^{[n]} \eta_{0i} \mathcal{S}_{sip}$$

for each solid phase material point.

4.4.5 Dynamic Quadrature Error Reduction

Particle methods for simulating fluid flows have an inherent problem with (among other things) point clumping (see recent work by Koh et al. [2012] and Maljaars [2016]). There are many physically admissible flows, such as those with stagnation points, which will result in material point tracers clumping together. By choosing the material point centroids as the quadrature points for our integral approximations, this clumping leads to quadrature error. In some fluid simulations, we see extremely spurious flows develop, which we attribute to this clumping error. To address this issue, we have developed a novel approach which intelligently 'nudges' material point centroids as the material flows. This nudge is the $\boldsymbol{\delta}_{\boldsymbol{sp}}^{k}$ and $\boldsymbol{\delta}_{\boldsymbol{fp}}^{k}$ from Equation (4.39).

The method we introduce relies on the nodal weight measure from Equation (4.10),

$$V_i = \int_\Omega \mathcal{N}_i(\mathbf{x}) dv$$

Importantly, we can calculate the value of this integral exactly through our choice of $\mathcal{N}_{1\mathrm{D}}(x)$. Since our material point characteristic functions are partitions of unity within the body (by Equation (4.1)),

$$\sum_{p=1}^{N_s} U_{sp}(\mathbf{x}) = \begin{cases} 1 & \mathbf{x} \in \mathcal{B}_s^t \\ 0 & \text{else} \end{cases}$$
$$\sum_{p=1}^{N_f} U_{fp}(\mathbf{x}) = \begin{cases} 1 & \mathbf{x} \in \mathcal{B}_f^t \\ 0 & \text{else} \end{cases}$$

we have,

$$\begin{aligned} V_i &= \sum_{p=1}^{N_s} \int_\Omega \mathcal{N}_i(\mathbf{x}) U_{sp}(\mathbf{x}) dv \qquad \text{if} \qquad (\mathcal{N}_i(\mathbf{x}) = 0 \quad \text{for} \quad \mathbf{x} \notin \mathcal{B}_s^t) \\ V_i &= \sum_{p=1}^{N_f} \int_\Omega \mathcal{N}_i(\mathbf{x}) U_{fp}(\mathbf{x}) dv \qquad \text{if} \qquad (\mathcal{N}_i(\mathbf{x}) = 0 \quad \text{for} \quad \mathbf{x} \notin \mathcal{B}_f^t) \end{aligned} \tag{4.57}$$

Therefore, we can exactly determine how much quadrature error has accumulated by approximating the above integrals according to Equation (4.17),

$$\begin{aligned} V_i &\approx v_{si} \equiv \sum_{p=1}^{N_s} v_{sp} \mathcal{N}_i(\mathbf{x}_{\mathbf{s}p}) \\ V_i &\approx v_{fi} \equiv \sum_{p=1}^{N_f} v_{fp} \mathcal{N}_i(\mathbf{x}_{\mathbf{f}p}) \end{aligned} \tag{4.58}$$

and measuring the relative *overshoot error*, e_{si} and e_{fi}, as follows,

$$\begin{aligned} e_{si} &= \max\left(0, \frac{v_{si} - V_i}{V_i}\right) \\ e_{fi} &= \max\left(0, \frac{v_{fi} - V_i}{V_i}\right) \end{aligned} \tag{4.59}$$

We have attempted several methods of reducing this error (which will be explored in future work); however the method used in this work is a strain-rate-dependent position correction given as follows,

$$\begin{aligned} \boldsymbol{\delta_{s}}_p^k &= -\alpha \Delta t (\Delta x)^2 \|\mathbf{L_{s0}}_p^{k+1}\| \sum_{i=1}^{[n]} e_{si} \nabla \mathcal{S}_{sip} \\ \boldsymbol{\delta_{f}}_p^k &= -\alpha \Delta t (\Delta x)^2 \|\mathbf{L_{f0}}_p^{k+1}\| \sum_{i=1}^{[n]} e_{fi} \nabla \mathcal{S}_{fip} \end{aligned} \tag{4.60}$$

with Δx the grid spacing of the Cartesian grid and α an arbitrary scale factor.

Chapter 5

Results

To validate our model, we use the numerical method descried in Section 4 to simulate underwater column collapses and quasi-2D shear flows for comparison with experimental data reported by Rondon et al. [2011] and Allen and Kudrolli [2017]. We also explore two applications of our method for potential use in impact/penetration problems (as explored in Ceccato et al. [2016]) or for loaded slope failures (see summary of numerical work in this area by Soga et al. [2015]).

5.1 Numerical Validation of Model and Method

In this section, we show that our model parameters can be fit to a particular class of fluid-sediment mixtures (in this case glass beads immersed in oil/water mixtures, see Pailha and Pouliquen [2009]) and that these fit parameters can be used to accurately simulate an underwater column collapse (from Rondon et al. [2011]) and quasi-2D erosion flows (from Allen and Kudrolli [2017]).

5.1.1 Model Fit to Glass Beads

Pailha and Pouliquen [2009] characterize the behavior of glass beads flowing down a chute while immersed in a viscous fluid (setup shown in Figure 5-1). The glass beads have density $\rho_s = 2500\frac{\text{kg}}{\text{m}^3}$ and diameter $d = 160\mu\text{m}$. Two mixtures of water/oil are reported and have viscosities $\eta_0 = 9.8 \times 10^{-3}$ Pa $\cdot$ s and $\eta_0 = 96 \times 10^{-3}$ Pa $\cdot$ s.

In order to fit our model to the characterization of this mixture, we have focused on a subset of the reported data shown in Figure 5-2. Figure 5-2b) shows the measured packing fraction of numerous flows/times plotted against the inertial number I_b (defined in Pailha and Pouliquen [2009]). We assume that the chute flow profile is parabolic (as is proven in Cassar et al. [2005]) such that $I_b \approx I_v$. We further assume that all of the reported flows are in the low Stokes limit (St $\to 0$) such that $I_m \approx \sqrt{2I_b}$. Fitting (2.104) to the lower extrema of the data, we find the following material parameters,

$$\phi_m = 0.584, \quad a = 1.23$$

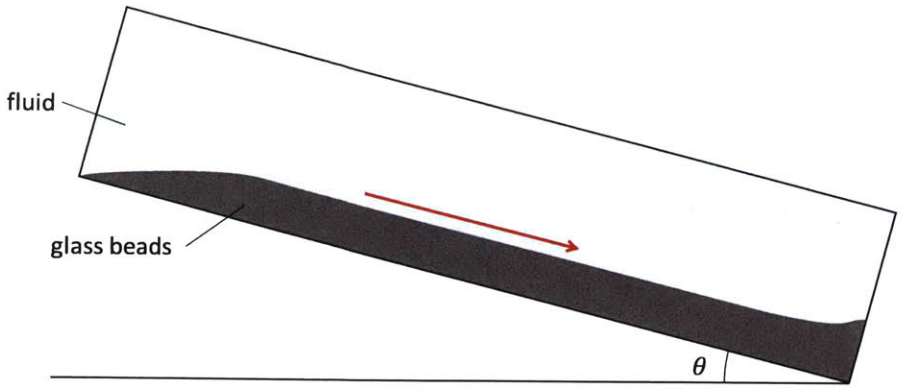

Figure 5-1: The rough experimental setup used by Pailha and Pouliquen [2009]. A bed of glass beads is immersed in a tank of viscous fluid. The incline of the base of the tank, θ, is changed to induce submerged slope avalanches.

Figure 5-2a) shows the measured internal friction angle $\tan(\theta)$ plotted against the experimental inertial number I_b. Assuming that all measurements were taken when the flows had reached steady state, $\tan(\theta) \approx \mu$ with μ given in (3.16). Fitting this equation to the data, we find the following material parameters,

$$\mu_1 = 0.35, \quad \mu_2 = 1.387, \quad b = 0.3085$$

Figure 5-2c) shows a set of flow onset measurements. At the transition from the "No flow" state to the "Flow" state, $\tan(\theta) \approx \mu_1 + \beta$. We assume that near the onset of flow $I_m = 0$. Therefore, the slope of the transition line between flowing and non-flowing behavior will be given by the sum $K_3 + K_4$. Fitting a slope to the data, we find, $K_3 + K_4 = 4.715$. Since the difference between K_3 and K_4 is difficult to determine experimentally and the rate of compaction in these flows is small (the K_5 term), we let,

$$K_3 = 0, \quad K_4 = 4.715, \quad K_5 = 0$$

With the parameters above determined for glass beads, we can now simulate other experiments which use similar mixtures. The remaining parameters (ρ_s, ρ_{0f}, η_0, and d) are determined by the specific materials used in the relevant experiments.

5.1.2 Granular Column Collapse of Glass Beads

Rondon et al. [2011] explore the behavior of collapsing granular columns submerged in a fluid with viscosity $\eta_0 = 12$ or 23 cP and density $\rho_{0f} \approx 1000\frac{\text{kg}}{\text{m}^3}$. A bed of glass beads with diameter $d = 225\mu$m and density $\rho_s = 2500\frac{\text{kg}}{\text{m}^3}$ was held at some initial packing fraction behind a retaining wall (see Figure 5-3). Once the wall was removed, the dynamics of the column were measured and reported.

In this work, we are interested in the behavior of two of the columns reported in that

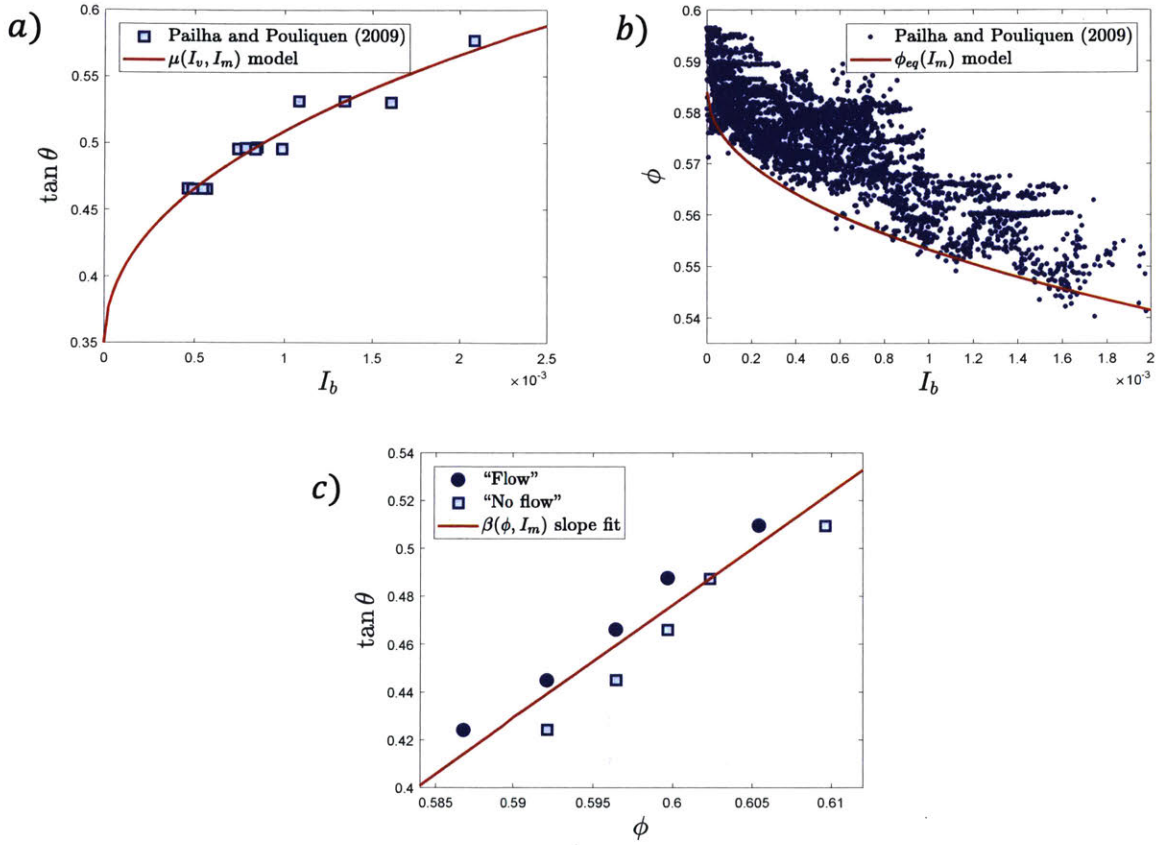

Figure 5-2: The three plots in this Figure show our model fit to the data presented in Figure 5 of Pailha and Pouliquen [2009]. a) Plot of internal friction coefficient against inertial number. b) Critical state packing fraction fit to extreme measurements of ϕ at various flow rates. c) β slope coefficient K_3 and K_4 fit to the critical angle between flowing and static slopes.

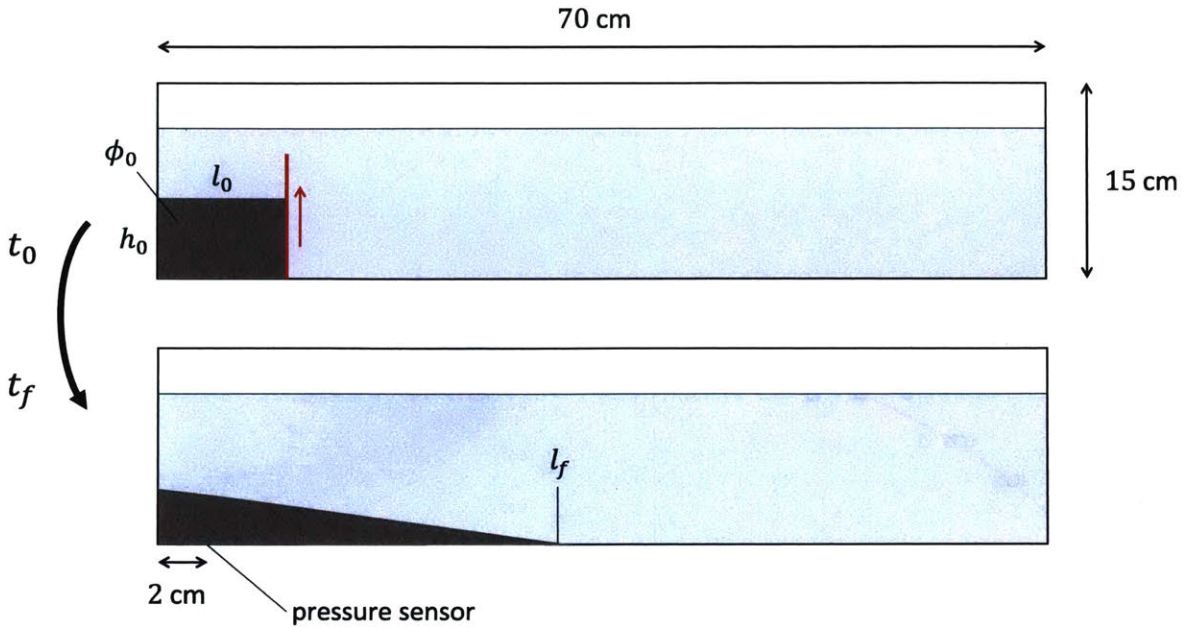

Figure 5-3: The experimental setup used by Rondon et al. [2011]. A column of small glass spheres with initial packing fraction ϕ_0 is held in place by a retaining wall and immersed in a long tank filled with a viscous fluid. At time t_0, the wall is removed and the column is allowed to collapse. A pressure sensor at the base of the column (2 cm from the edge of the tank) collects pore pressure data during the collapse. The run-out profiles of the column are captured with a camera.

work (see Table 5.1). The two columns are made of the same mass of glass beads formed into a *loose* and *dense* column (with initial packing fraction given by ϕ_0). It was observed that the initially *loose* column collapsed much faster with much longer run-out than the initially *dense* column.

To simulate these two column collapses, we consider a reduced computational domain by assuming that the flow is approximately plane-strain (quasi-2D) and that the fluid tank can be shortened to 30 cm in length without significantly affecting the dynamics of the column collapse. We then run our model with the initial conditions given in Table 5.1, computational parameters given in Table 5.2, and remaining material parameters given in Section 5.1.1. The fluid-wall interaction is governed by a simple frictionless boundary condition while the grain-wall interaction is governed by the frictional boundary rule described in Section 4.4.2.

In both the experiments and simulations, the only differences between the *dense* and *loose* columns are the initial packing fraction, the initial column height, and the initial hydrostatic stress state. The resulting differences in the simulated flow dynamics are due to the different solutions picked out by the governing equations given these initial conditions. A series of snapshots taken from these two simulations (as run on the 300×100 grid) are shown in Figure 5-4.

In addition to visualizing the solid phase dilation and compaction as in Figure 5-4, we

Table 5.1: Experimental Setup for Rondon et al. [2011]

Parameter	Dense Column	Loose Column
Tank Length	70 cm	70 cm
Tank Height	15 cm	15 cm
Tank Width	15 cm	15 cm
ϕ_0	0.60	0.55
l_0	6.0 cm	6.0 cm
h_0	4.2 cm	4.8 cm
ρ_s	2500 $\frac{\text{kg}}{\text{m}^3}$	2500 $\frac{\text{kg}}{\text{m}^3}$
d	255 μm	255 μm
ρ_{0f}	1000 $\frac{\text{kg}}{\text{m}^3}$	1000 $\frac{\text{kg}}{\text{m}^3}$
η_0	12 or 23 cP	12 or 23 cP

can also examine the differences in shearing rate and fluid pore pressure as shown in Figure 5-5. As the initially *dense* column collapses, the solid phase experiences *shear dilation* and 'opens', increasing the porosity of the mixture. This results in pore tension in the fluid phase as fluid is drawn into the increased pore space (see Figure 5-5a). This increased pore tension increases the effective granular pressure given by $\tilde{p}$ in (2.106) and therefore strengthens of the solid phase. One the other hand, as the initially *loose* collapses the solid phase experiences *plastic compaction*, reducing the porosity of the mixture. This has the opposite effect, causing a positive pore pressure (see Figure 5-5b) which reduces the strength of the solid phase. It is this coupling of solid phase flow to fluid phase pressure to solid phase strength that results in these two completely different collapse behaviors.

By accurately modeling these complex interactions, we are able to capture the vastly different collapse profiles (see Figure 5-6), predict the measured excess pore pressure (see Figure 5-7a), and match the time-accurate front motion (see Figure 5-7b) reported in Rondon et al. [2011].

The collapse profiles shown in Figure 5-6 are the $n = 0.45$ contours of the nodal porosity field $n(\mathbf{x})$ and show reasonable similarity to the experimental profiles provided courtesy of Pascale Aussilous.

To compare the simulated excess pore pressure to the excess pore pressure reported by Rondon et al. [2011], we first 'cast' the pressure field $p_f(\mathbf{x})$ defined by the coefficients $\{p_{fp}\}$ to the nodes of the background grid. Due to the collocation of the stress update with the material point centroids and the motion of the material point centroids through the computational domain, spurious pressure fields are known to develop (see Andersen and Andersen [2010]). The pore pressure in Figure 5-7b) shows the weighted average nodal representation of pressure (as defined in Dunatunga and Kamrin [2015]) near (but not at) the lower domain boundary and 2 cm from the left wall. This value is compared to a hydrostatic reference value to find the excess pore pressure. In the *dense* 300×100 simulation, the fluid phase material points exhibited excessive clumping (see Section 4.4.5), so a second nodal sample was taken at the same height, 2 cm from the right wall and used as the reference

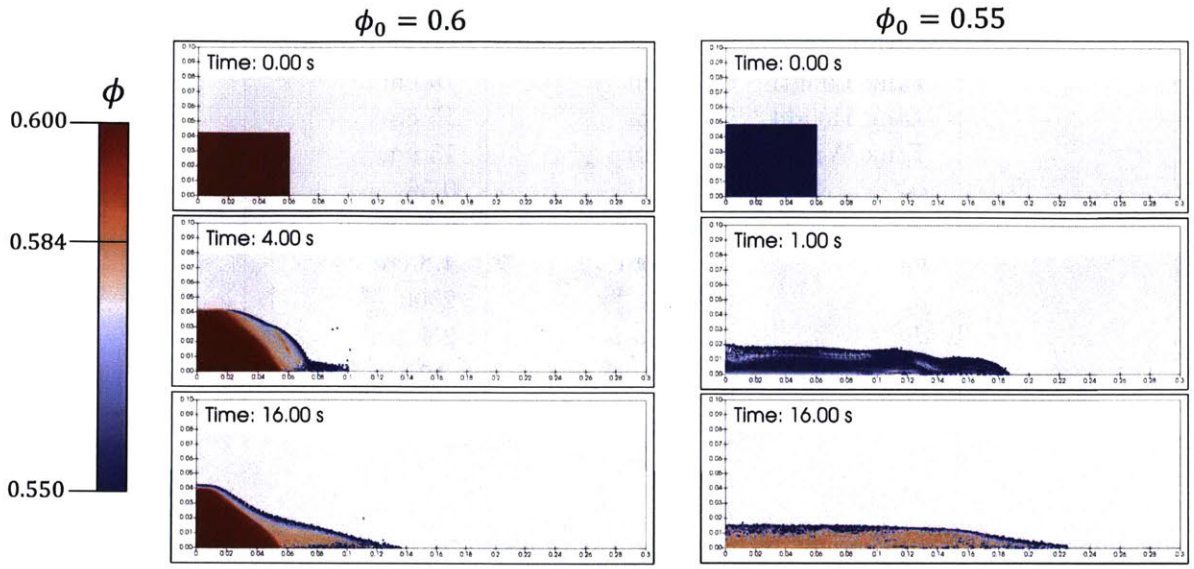

Figure 5-4: Comparison between simulated collapses for the *loose* initial packing (right) and the *dense* initial packing (left) using the 300×100 element grid described in Table 5.2. Solid phase material points are colored by packing fraction according to the scale at the left. Fluid phase material points are colored light gray.

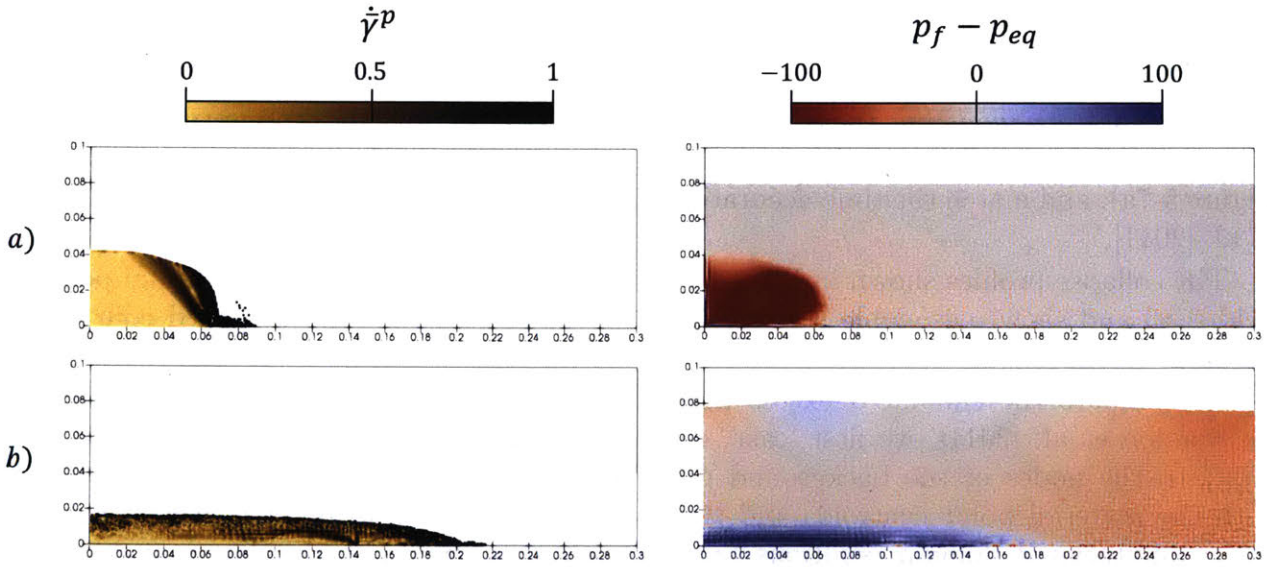

Figure 5-5: Snapshot of simulated solid phase equivalent plastic shear rate (left) and fluid phase excess pore pressure (right) at $t = 4$s for a) the initially *dense* column and b) the initially *loose* column. The plastic shearing rate is visualized at the material point centroids of the solid phase. The excess pore pressure as compared to a hydrostatic baseline p_{eq} (after 'projecting' to the grid and back to the points) is visualized at the fluid phase centroids.

Table 5.2: Simulation Parameters for Column Collapses

Parameter	300×100 Simulations	120×40 Simulations
Tank Length	30 cm	30 cm
Tank Height	10 cm	10 cm
Fluid Height	8 cm	8 cm
Elements	300 × 100	120 × 40
Points per Cell	4	4
Δt	$5 \cdot 10^{-5}$ s	$2 \cdot 10^{-5}$ s
Δx	1.0 mm	2.5 mm
t_0	0s	0s
t_f	20 s	60 s
G	$3.8 \cdot 10^4$ Pa	$3.8 \cdot 10^5$ Pa
K	$8.3 \cdot 10^4$ Pa	$8.3 \cdot 10^5$ Pa
η_0	$1.2 \cdot 10^{-2}$ Pa·s	$1.2 \cdot 10^{-2}$ Pa·s
κ	$1.0 \cdot 10^5$ Pa	$1.0 \cdot 10^6$ Pa

value. Close agreement is seen between the simulated pore pressure and the experimental measurements.

Front positions shown in Figure 5-7b) are determined by taking the maximum x-position of the collapse profiles shown in Figure 5-6.

All together, the results shown in Figures 5-6 and 5-7 indicate that our model is capable of accurately predicting the dynamics of granular column collapses and able to capture the sensitivity of the problem to small changes in initial conditions.

5.1.3 Quasi-2D Flow of Glass Beads

In addition to sudden collapses of granular columns, we are also interested in using our model to simulate steady erosion processes. To gage the accuracy of our method for such problems, we simulate the experiments performed by Allen and Kudrolli [2017].

As shown in Figure 5-8, the experimental setup approximates a 2D erosion flow by driving a conical motor at a prescribed rotation rate, f, above an immersed granular bed of glass beads. The refractive index of the beads and fluid are matched so that a camera can image a single plane of mixture illuminated by a laser. The results measured in that work are taken from series of images captured of that plane and reported as a function of vertical depth below the driving surface, z.

The mixture of fluid and grains used in Allen and Kudrolli [2017] is similar to that used in Pailha and Pouliquen [2009], suggesting that we can use the same material parameters determined in Section 5.1.1. The remaining material parameters are given by the specific materials used in the experiment: $\rho_{0f} = 1002\frac{\text{kg}}{\text{m}^3}$, $\eta_0 = 0.021$ Pa·s, $\rho_s = 2500\frac{\text{kg}}{\text{m}^3}$, and $d = 1.05$ mm.

We simulate four of the reported flows in that work, $f/f_c = \{0.37, 1.04, 1.26, 1.33\}$, where

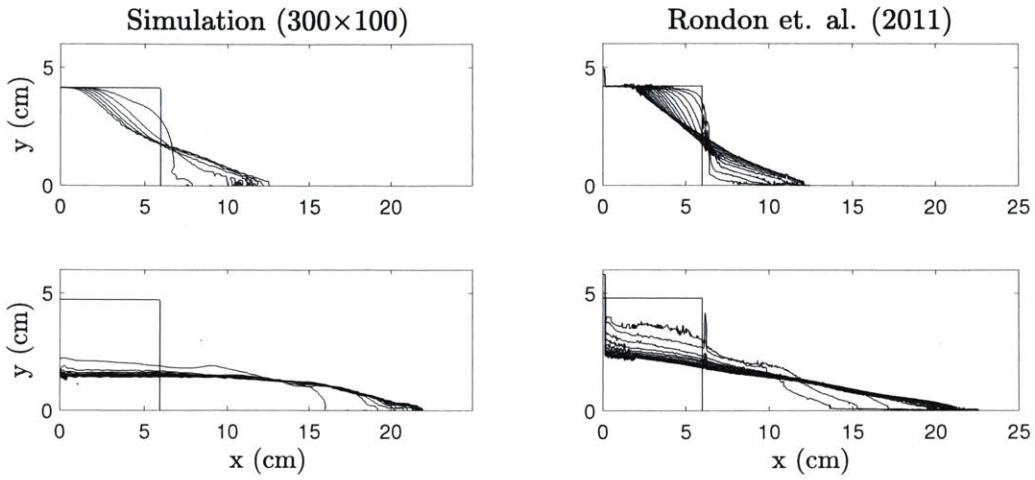

Figure 5-6: Contours of the collapsing columns from the *dense* simulation (top, left) taken at 3s intervals and the *loose* simulation (bottom, left) taken at 0.66s intervals. The corresponding contours for the *dense* experiment (top, right) and *loose* experiment (bottom, right) from Rondon et al. [2011] are also shown. The simulated profiles are generated by plotting the contour of the nodal porosity field (given by the coefficients $\{n_i\}$) at $n = 0.45$. The experimental contours are provided courtesy of Pascale Aussillous

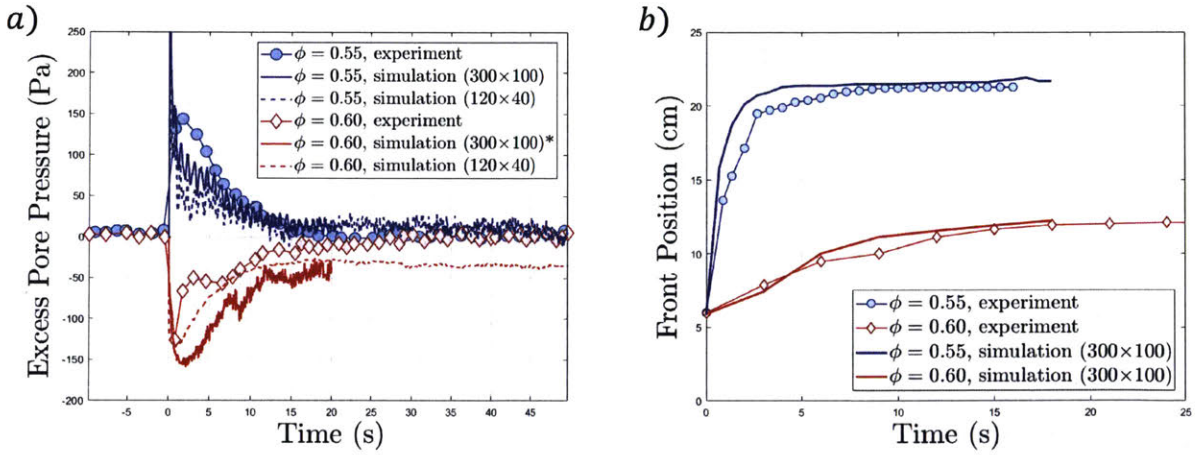

Figure 5-7: a) Comparison of the simulated excess pore pressure for the *loose* initial packing (top, blue) and the *dense* initial packing (bottom, red). The base pore pressure for all simulations is approximately 800 Pa. b) Comparison between simulated front positions for the *loose* initial packing (top, blue) and the *dense* initial packing (bottom, red).

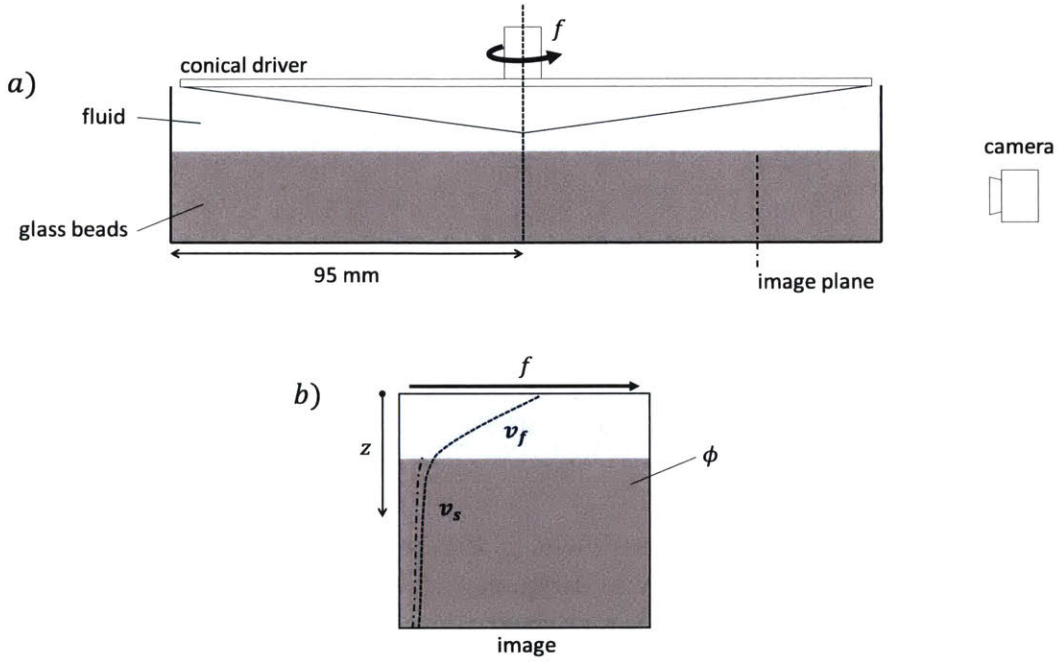

Figure 5-8: a) Experimental setup of Allen and Kudrolli [2017]. An approximately 9 mm bed of grains is immersed in a cylindrical tank filled with fluid. A conical driver is submerged to the granular surface and driven by a motor at a specified rotation rate f. b) The resulting flow is imaged at a plane near the edge of the tank. Measurements are taken of phase velocities and packing fractions as a function of distance z from the driving surface.

f is the assigned driving frequency and f_c is the reported critical driving frequency around which grains become suspended in the fluid flow. We set up an x-periodic domain measuring 15.5 mm by 15.5 mm and drive the upper surface at a velocity determined by the ratios the driving frequency f. We let the lower wall be governed by a no-slip boundary condition. The resulting fluid flow is allowed to reach steady-state and the flow properties are averaged over a 12 s time window. A summary of the simulation setup is given in Table 5.3.

Table 5.3: Simulation Parameters for Erosion Flows

Parameter	$f/f_c = 0.37$	$f/f_c = 1.04$	$f/f_c = 1.26$	$f/f_c = 1.33$
Bed Height	10.5 mm	11.0 mm	11.0 mm	11.4 mm
Driving Velocity	$0.2325\frac{\text{m}}{\text{s}}$	$0.6536\frac{\text{m}}{\text{s}}$	$0.7919\frac{\text{m}}{\text{s}}$	$0.8359\frac{\text{m}}{\text{s}}$
Elements	20×20	20×20	20×20	20×20
Points per Cell	9	9	9	9
Δt	$2 \cdot 10^{-5}$ s	$2 \cdot 10^{-5}$ s	$2 \cdot 10^{-5}$ s	$2 \cdot 10^{-5}$ s
Δx	775 μm	775 μm	775 μm	775 μm
t_0	0s	0s	0s	0s
t_f	30 s	30 s	30s	30s
G	$3.8 \cdot 10^4$ Pa	$3.8 \cdot 10^4$ Pa	$3.8 \cdot 10^4$ Pa	$3.8 \cdot 10^4$ Pa
K	$8.3 \cdot 10^4$ Pa	$8.3 \cdot 10^4$ Pa	$8.3 \cdot 10^4$ Pa	$8.3 \cdot 10^4$ Pa
η_0	$2.1 \cdot 10^{-2}$ Pa·s	$2.1 \cdot 10^{-2}$ Pa·s	$2.1 \cdot 10^{-2}$ Pa·s	$2.1 \cdot 10^{-2}$ Pa·s
κ	$1.0 \cdot 10^5$ Pa	$1.0 \cdot 10^5$ Pa	$1.0 \cdot 10^5$ Pa	$1.0 \cdot 10^5$ Pa

A series of simulation snapshots is shown in Figure 5-9. As was observed in Allen and Kudrolli [2017], below the critical driving frequency f_c there is essentially no flow of grains; however, once the driving frequency f is increased above f_c, solid phase material is 'picked up' by the shearing of the fluid phase and enters into suspension. The steady-state flow predicted by our simulations shows strong similarity to the experimentally measured packing fraction (see Figure 5-10) and phase velocities (see Figure 5-11).

The simulated packing fractions and velocities are plotted by averaging the material point coefficients $\{\mathbf{x}_{\mathbf{s}p}\}$, $\{\mathbf{x}_{\mathbf{f}p}\}$, $\{\mathbf{v}_{\mathbf{s}p}\}$, $\{\mathbf{v}_{\mathbf{f}p}\}$, and $\{\phi_p\}$ over a 12s window. The resulting phase velocity and packing fraction averages are then sorted by the average material point centroid position and filtered using the MATLAB `smooth()` function. It is important to note that as the solid phase dilates, the solid phase material points will separate. After the material points separate by more than 1 element (around $\phi \approx 0.2$), the material point value ϕ_p will no longer be representative of the true mixture packing fraction.

5.2 Qualitative Results

In this section we consider two potential applications of our model and method. The first shows the behavior of a fluid-grain mixture as an intruding body is pressed into its surface. The second shows the effect of water level on the failure of a loaded slope.

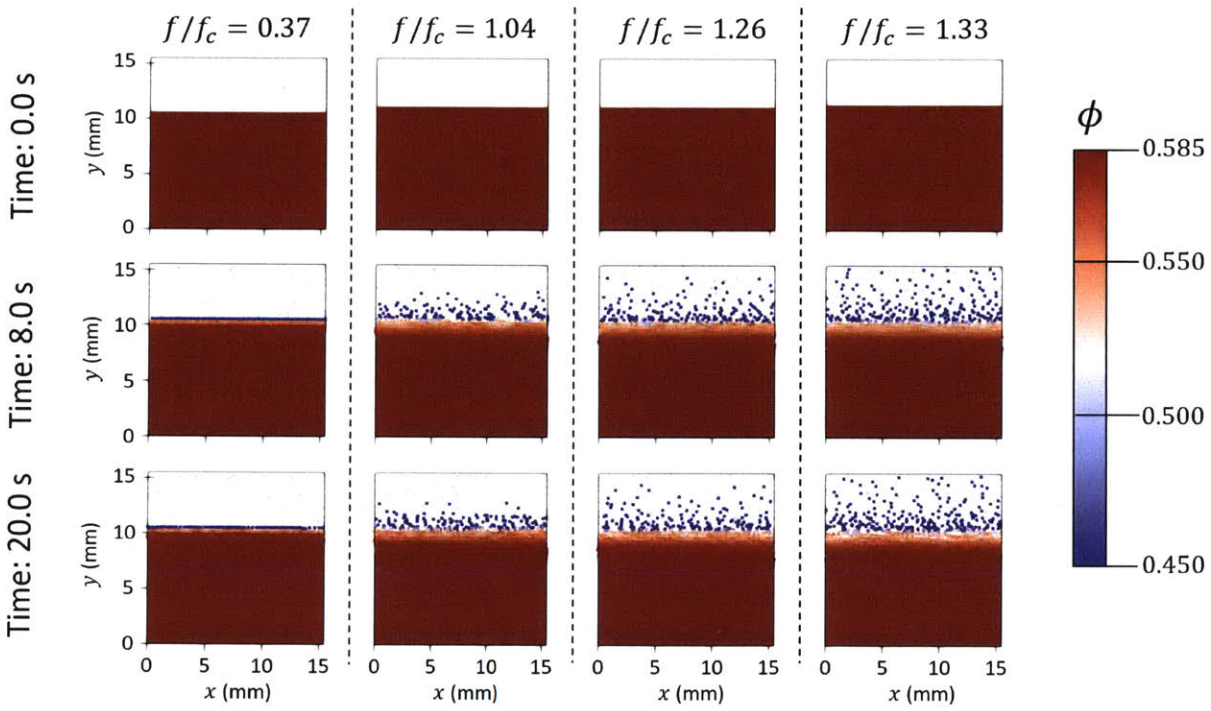

Figure 5-9: Comparison between the simulated erosion flows described in Table 5.3. Solid phase material points are colored by packing fraction according to the scale at the right. Fluid phase material points are colored light gray. In all cases, the shearing of the fluid phase induces motion in the solid phase. As the driving frequency f increases above the critical f_c (as reported in Allen and Kudrolli [2017]) solid phase material is 'picked up' and becomes suspended in the fluid.

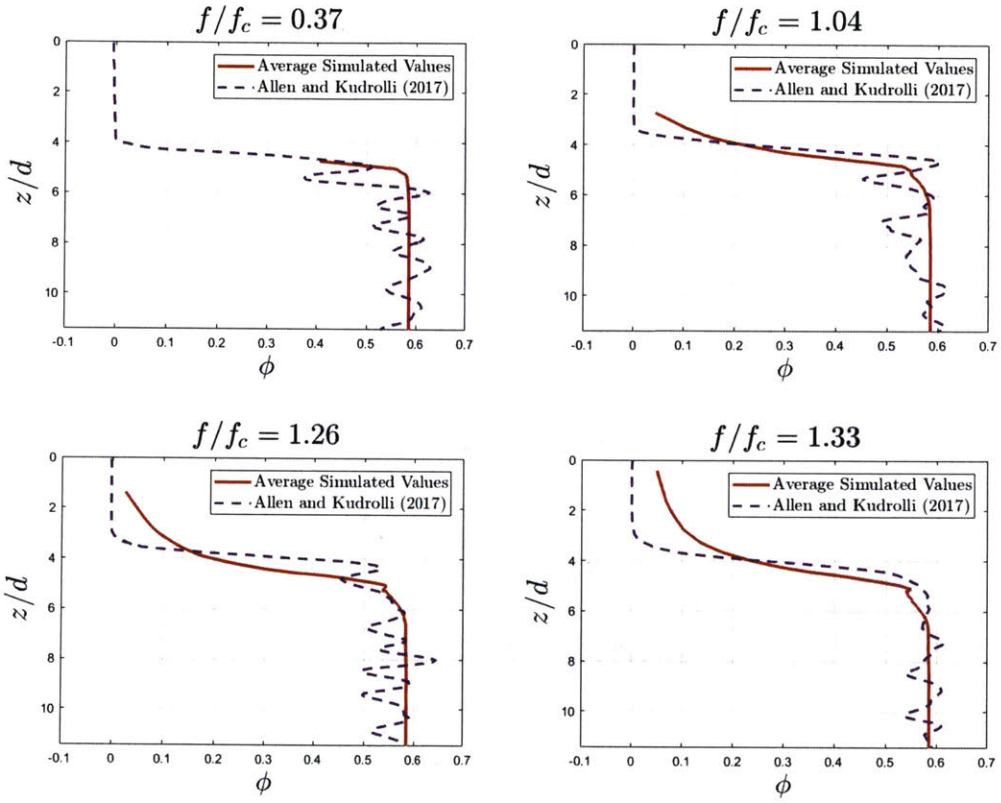

Figure 5-10: Plots comparing the time-averaged steady state packing fractions as a function of normalized depth reported in Allen and Kudrolli [2017] to those found by running the simulations described in Table 5.3. Very close matching is observed when the solid phase material is *dense*; however the simulated data has a heavy tail in the *dilute* regime. This is likely due to the large empty spaces between the solid phase material points when they become suspended in the fluid flow.

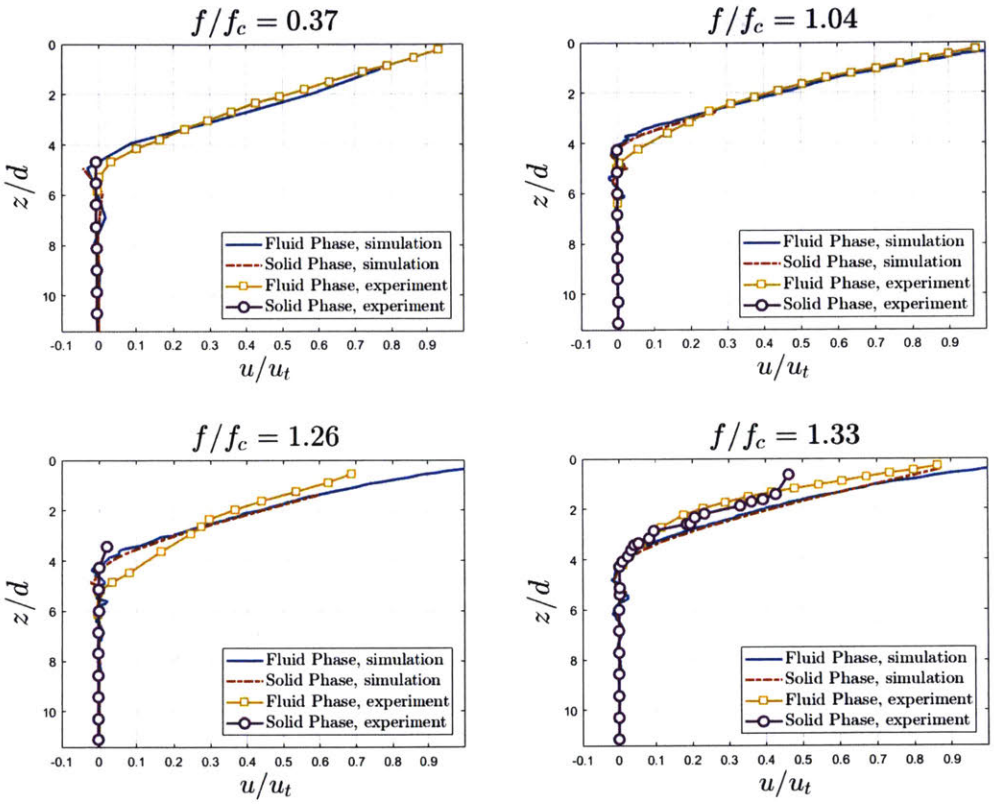

Figure 5-11: Plots comparing the time-averaged steady state phase velocities u (normalized by the velocity of the driving surface u_t) as a function of normalized depth reported in Allen and Kudrolli [2017] to those found by running the simulations described in Table 5.3. The simulated values show strong similarity to the experimental values; however, there are oscillations visible in the simulated profiles. These oscillations are due to well known errors in the material point velocity fields.

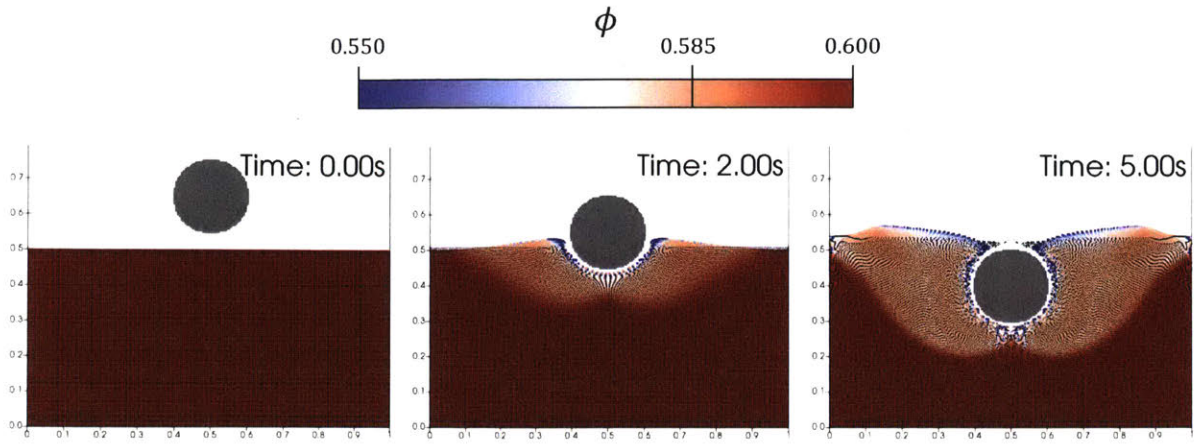

Figure 5-12: Series of snapshots taken from simulation described in Section 5.2.1. Solid phase material points are colored according to packing fraction. Fluid material points are represented by small black dots. Intruder material points are colored light gray. As the intruder enters the mixture, the shearing of the solid phase results in noticeable dilation.

5.2.1 2D Circular Intruder

The use of the material point method for intrusion into a saturated soil is explored at length in Ceccato et al. [2016]. In that work, the mixture model developed in Bandara and Soga [2015] is adjusted to use the Modified Cam Clay model to model the solid phase behavior.

Here we show that our model may be extended to explore similar problems by simulating the intrusion of a disk into a submerged bed of acrylic beads. As an exploratory problem, we use the material parameters given in Table 3.1 and let $d = 1.0$ cm, $\rho_s = 2500\frac{\text{kg}}{\text{m}^3}$, and $\rho_f = 1000\frac{\text{kg}}{\text{m}^3}$. A 1m×1m domain is simulated on a 100×100 element grid with 4 material points per cell. The domain is initially half-filled by a mixture of fluid and grains with packing fraction $\phi_0 = 0.60$. The resulting behavior shown in Figure 5-12. As the intruder enters the mixture, we observe shear dilation of the granular material and independent motion of the two phases of material as fluid fills in the opening pore space.

5.2.2 2D Slope Collapse

Another application of interest for our model is the complex interactions between structures and saturated soils. To demonstrate the application of this model to the problem of a loaded slope, we consider two simple cases. In the first case, a dry slope with length 14m and height 5m is loaded with a cement block at the top (see Figure 5-13). The slope is composed of 2mm diameter grains with density $\rho_s = 2500\frac{\text{kg}}{\text{m}^3}$. In the second case, an identical slope with identical loading and material composition is partially submerged in water (approximating a shoreline).

The simulations are performed in a 40m×10m domain discretized into 160×40 elements. The material points for the three bodies are seeded with 9 material points per grid cell.

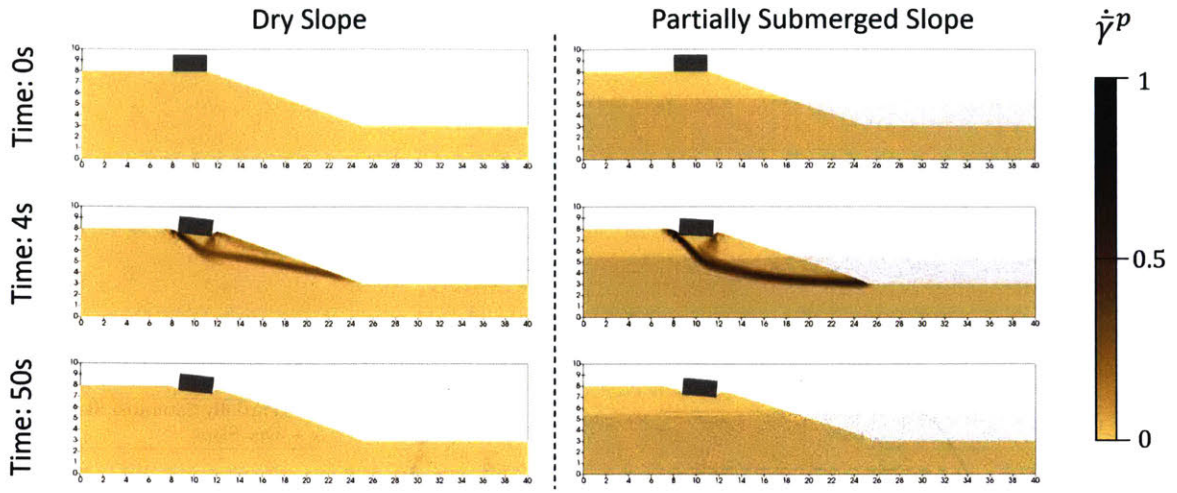

Figure 5-13: Series of snapshots taken from simulations described in Section 5.2.2. Solid phase material points are colored according to the *equivalent plastic shearing rate*, $\dot{\gamma}^p$. Fluid material points are represented by light gray dots. Block material points are colored light gray.

The initial packing of the granular slope is $\phi_0 = 0.585$. The resulting collapses are shown in Figure 5-13. We let the material properties be identical to those given in Section 5.1.1. As shown in Figure 5-14, the resulting motion of the block (approximating a structure) on top of the slope has a strong dependence on the water level in the slope. Over the course of 5 simulated seconds, the block on the partially submerged slope moves 20% more in the x-direction, 36% more in the y-direction, and rotates 34% less.

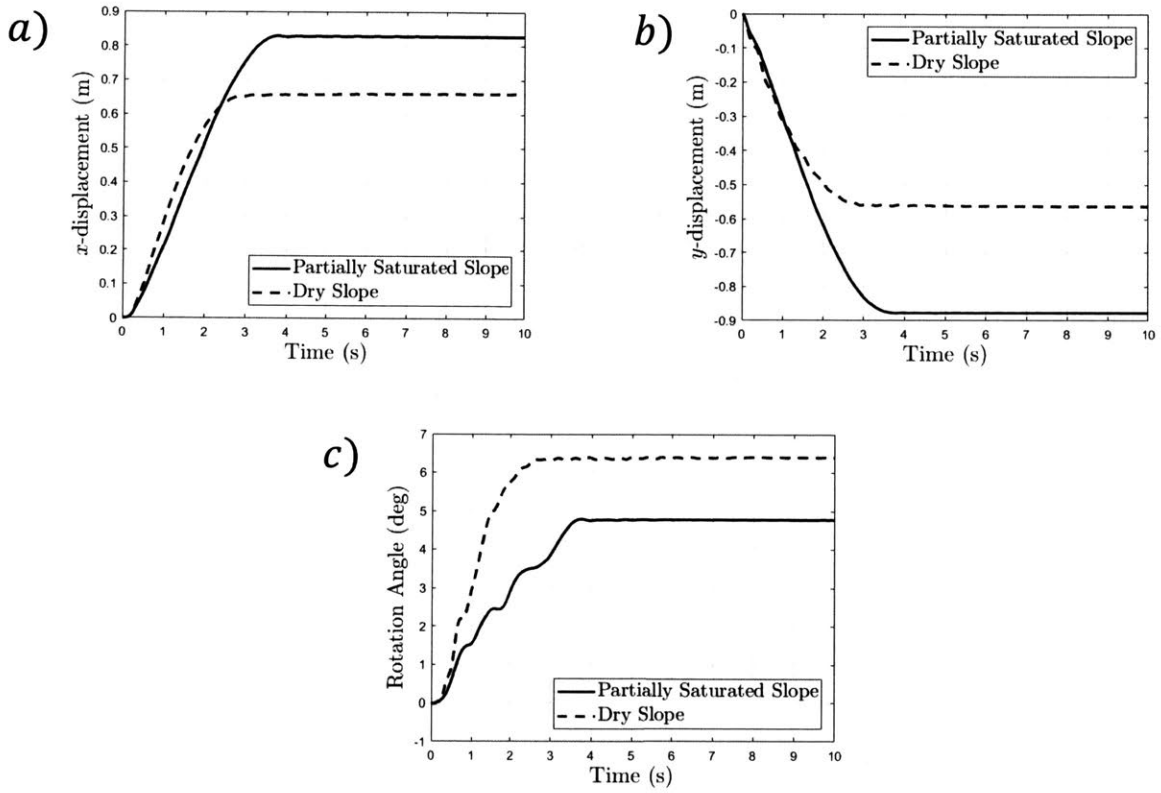

Figure 5-14: Plots of block motion for simulations described in Section 5.2.2. a) The x-displacement of the block's center of mass. b) The y-displacement of the block's center of mass. c) The rotation of the block about its center of mass.

Chapter 6

Conclusion

We have developed a full set of constitutive relations for fluid-sediment mixtures which is capable of accurately and robustly modeling both dense and dilute flows of material. Our model is derived from the integral form of the basic balance laws for two-phase mixtures and formulated to capture the dry and viscous inertial rheologies of granular materials, the critical state behavior of grains under shear, the viscous thickening of fluid due to suspended sediments, and the Darcy-like inter-phase drag. This model is implemented in a numerical framework capable of coupling the equations of motion governing the two independent continuum bodies defining the mixture.

We characterize mixtures of glass beads immersed in a viscous fluid by fitting our model to the experimental data reported in Pailha and Pouliquen [2009]. We then take these material parameters and show that our model and numerical implementation is able to accurately predict the behavior of both collapsing granular columns (see Rondon et al. [2011]) and shearing of fluid above granular beds (see Allen and Kudrolli [2017]) *without re-fitting material properties.* In addition, we also look at the application of this model and method to the problems of intrusion and slope stability.

The model we have presented in this work may be extensible to more general fluid-sediment mixtures such as those involving air (especially for examining the kick-up of dust for vertical take-off and landing vehicles). Other extensions of this model may look at adding cohesion (redefining the f_1 and f_2 yield conditions), introducing a fabric tensor to the rules governing dilation, or adding non-local effects.

In addition to the novel mixture constitutive rules, we have briefly examined a method to reduce the growth of numerical error in dynamic fluid flows. We believe that more focused work in this area is warranted and our approach here hints at a potential path toward improving known short-comings of the material point method.

Bibliography

Keita Abe, Kenichi Soga, and Samila Bandara. Material point method for coupled hydromechanical problems. *Journal of Geotechnical and Geoenvironmental Engineering*, 140(3): 04013033, 2013.

Benjamin Allen and Arshad Kudrolli. Depth resolved granular transport driven by shearing fluid flow. *Physical Review Fluids*, 2(2):024304, 2017.

L. Amarsid, J. Y. Delenne, P. Mutabaruka, Y. Monerie, F. Perales, and F. Radjai. Viscoinertial regime of immersed granular flows. *Physical Review E*, 96, 2017.

L. Anand and C. Su. A theory for amorphous viscoplastic materials undergoing finite deformations, with applications to metallic glasses. *Journal of the Mechanics and Physics of Solids*, 53(6):1362–1396, 2005.

Soren Andersen and Lars Andersen. Analysis of spatial interpolation in the material-point method. *Computers & structures*, 88(7-8):506–518, 2010.

Samila Bandara and Kenichi Soga. Coupling of soil deformation and pore fluid flow using material point method. *Computer and Geotechnics*, 63:199–214, 2015.

SG Bardenhagen and EM Kober. The generalized interpolation material point method. *Computer Modeling in Engineering and Sciences*, 5(6):477–496, 2004.

R. Beetstra, M. A. van der Hoef, and J. A. M. Kuipers. Drag force of intermediate reynolds number flow past mono- and bidisperse arrays of spheres. *AIChE Journal*, 53(2):489–501, February 2007.

FC Blake. The resistance of packing to fluid flow. *Transactions of the American Institute of Chemical Engineers*, 14(415-421):3, 1922.

F. Boyer, E. Gauzelli, and O. Pouliquen. Unifying suspension and granular rheology. *Physical Review Letters*, 107(18), 2011.

Jeremiah U Brackbill, Douglas B Kothe, and Hans M Ruppel. Flip: a low-dissipation, particle-in-cell method for fluid flow. *Computer Physics Communications*, 48(1):25–38, 1988.

JU Brackbill and HM Ruppel. Flip: A method for adaptively zoned, particle-in-cell calculations of fluid flows in two dimensions. *Journal of Computational Physics*, 65(2):314–343, 1986.

P. C. Carman. Fluid flow through granular beds. *Transactions - Institution of Chemical Engineers*, 15:150–166, 1937.

C Cassar, M Nicolas, and O Pouliquen. Submarine granular flows down inclined planes. *Physics of fluids*, 17(10):103301, 2005.

Francesca Ceccato and Paolo Simonini. Granular flow impact forces on protection structures: Mpm numerical simulations with different constitutive models. *Procedia Engineering*, 158: 164–169, 2016.

Francesca Ceccato, Lars Beuth, Pieter A Vermeer, and Paolo Simonini. Two-phase material point method applied to the study of cone penetration. *Computers and Geotechnics*, 80: 440–452, 2016.

Chingyi Chang and Robert L Powell. Dynamic simulation of bimodal suspensions of hydrodynamically interacting spherical particles. *Journal of Fluid Mechanics*, 253:1–25, 1993.

Chingyi Chang and Robert L Powell. Effect of particle size distributions on the rheology of concentrated bimodal suspensions. *Journal of Rheology*, 38(1):85–98, 1994.

JS Chong, EB Christiansen, and AD Baer. Rheology of concentrated suspensions. *Journal of applied polymer science*, 15(8):2007–2021, 1971.

Roland Clift, John R. Grace, and Martin E Weber. *Bubbles, drops, and particles.* Courier Corporation, 2005.

Benjamin K Cook, David R Noble, and John R Williams. A direct simulation method for particle-fluid systems. *Engineering Computations*, 21(2/3/4):151–168, 2004.

Frederic Da Cruz, Sacha Emam, Michael Prochnow, Jean-Noel Roux, and Francois Chevoir. Rheophysics of dense granular materials: Discrete simulation of plane shear flows. *Physical Review E*, 72(2), 2005.

D. S. Drumheller. On theories for reacting immiscible mixtures. *International Journal of Engineering Science*, 38:347–382, 2000.

Sachith Dunatunga and Ken Kamrin. Continuum modelling and simulation of granular flows through their many phases. *Journal of Fluid Mechanics*, 779:483–513, 2015.

Jules Étienne Juvénal Dupuit. *Études théoriques et pratiques sur le mouvement des eaux dans les canaux découverts et à travers les terrains perméables: avec des considérations relatives au régime des grandes eaux, au débouché à leur donner, et à la marche des alluvions dans les rivières à fond mobile.* Dunod, 1863.

H Eilers. The colloidal structure of asphalt. *The Journal of Physical Chemistry*, 53(8): 1195–1211, 1949.

Albert Einstein. Calculation of the viscosity-coefficient of a liquid in which a large number of small spheres are suspended in irregular distribution. *Ann. Phys. Leipzig*, 19:286–306, 1906.

Elliot James Fern and Kenichi Soga. The role of constitutive models in mpm simulations of granular column collapses. *Acta Geotechnica*, 11(3):659–678, 2016.

F Ferrini, D Ercolani, B De Cindio, L Nicodemo, L Nicolais, and S Ranaudo. Shear viscosity of settling suspensions. *Rheologica Acta*, 18(2):289–296, 1979.

Morton E. Gurtin, Eliot Fried, and Lallit Anand. *The Mechanics and Thermodynamics of Continua*. Cambridge University Press, Cambridge, UK, 2010.

Peng Huang, X Zhang, S Ma, and X Huang. Contact algorithms for the material point method in impact and penetration simulation. *International journal for numerical methods in engineering*, 85(4):498–517, 2011.

Roy Jackson. *The Dynamics of Fluidized Particles*. Cambridge University Press, Cambridge, UK, 2000.

Pierre Jop, Yoel Forterre, and Olivier Pouliquen. A constitutive law for dense granular flows. *Nature*, 441(7094), 2006.

Vaclav Klika. A guide through available mixture theories for applications. *Critical Reviews in Solid State and Materials Sciences*, 39(2):154–174, 2014.

CG Koh, M Gao, and C Luo. A new particle method for simulation of incompressible free surface flow problems. *International journal for numerical methods in engineering*, 89(12): 1582–1604, 2012.

Irvin M Krieger and Thomas J Dougherty. A mechanism for non-newtonian flow in suspensions of rigid spheres. *Transactions of the Society of Rheology*, 3(1):137–152, 1959.

JM Maljaars. A hybrid particle-mesh method for simulating free surface flows. 2016.

Mickael Pailha and Olivier Pouliquen. A two-phase flow description of the initiation of underwater granular avalanches. *Journal of Fluid Mechanics*, 633:115–135, 2009.

AJ Poslinski, ME Ryan, RK Gupta, SG Seshadri, and FJ Frechette. Rheological behavior of filled polymeric systems ii. the effect of a bimodal size distribution of particulates. *Journal of Rheology*, 32(8):751–771, 1988.

Loic Rondon, Olivier Pouliquen, and Pascale Aussillous. Granular collapse in a fluid: role of the initial volume fraction. *Physics of Fluids*, 23(7):073301, 2011.

Stephane Roux and Farhang Radjai. Texture-dependent rigid-plastic behavior. In H.J. Herrmann, JP. Hovi, and S. Luding, editors, *Physics of dry granular media*, pages 229–236. Springer, 1998.

Stephane Roux and Farhang Radjai. Statistical approach to the mechanical behavior of granular media. *Mechanics for a New Mellennium*, pages 181–196, 2001.

John Walter Rudnicki and JR Rice. Conditions for the localization of deformation in pressure-sensitive dilatant materials. *Journal of the Mechanics and Physics of Solids*, 23(6):371–394, 1975.

Andrew P Shapiro and Ronald F Probstein. Random packings of spheres and fluidity limits of monodisperse and bidisperse suspensions. *Physical review letters*, 68(9):1422, 1992.

Kenichi Soga, E Alonso, A Yerro, K Kumar, and S Bandara. Trends in large-deformation analysis of landslide mass movements with particular emphasis on the material point method. *Geotechnique*, 66(3):248–273, 2015.

Michael Steffen, Robert M Kirby, and Martin Berzins. Analysis and reduction of quadrature errors in the material point method (mpm). *International journal for numerical methods in engineering*, 76(6):922–948, 2008.

Jonathan J Stickel and Robert L Powell. Fluid mechanics and rheology of dense suspensions. *Annu. Rev. Fluid Mech.*, 37:129–149, 2005.

RF Storms, BV Ramarao, and RH Weiland. Low shear rate viscosity of bimodally dispersed suspensions. *Powder technology*, 63(3):247–259, 1990.

Deborah Sulsky, Zhen Chen, and Howard L Schreyer. A particle method for history-dependent materials. *Computer methods in applied mechanics and engineering*, 118(1-2): 179–196, 1994.

Karl Terzaghi. *Theoretical Soil Mechanics*. John Wiley and Sons Inc., New York, New York, 1943.

Clifford Truesdell and Walter Noll. The non-linear field theories of mechanics. In *The non-linear field theories of mechanics*. Springer, 1965.

Raffi M Turian and Tran-Fu Yuan. Flow of slurries in pipelines. *AIChE Journal*, 23(3): 232–243, 1977.

M. A. van der Hoef, R. Beetstra, and J. A. M. Kuipers. Lattice-boltzmann simulations of low-reynolds-number flow past mono- and bidisperse arrays of spheres: results for the permeability and drag force. *Journal of Fluid Mechanics*, 528:233–254, 2005.

Krzysztof Wilmanski. *Continuum Thermodynamics - Part 1: Foundations*. World Scientific, 2008.